UNIVERSITY OF CALIFORNIA,
IRVINE

Design and Implementation of Robust Full-Duplex Wireless Network

DISSERTATION

submitted in partial satisfaction of the requirements
for the degree of

DOCTOR OF PHILOSOPHY

in Electrical and Computer Engineering

by

Sergey Shaboyan

Dissertation Committee:
Professor Ahmed Eltawil, Chair
Professor Ender Ayanoglu
Professor Zhiying Wang

2020

DEDICATION

To my parents.

TABLE OF CONTENTS

LIST OF FIGURES

LIST OF TABLES

LIST OF ALGORITHMS

ACKNOWLEDGMENTS

I would like to express my deepest gratitude to my advisor, Professor Ahmed M. Eltawil, who provided me with the guidance and support in all aspects of my research at UC Irvine.

I would like to thank my Qualifying Exam Committee members Professor Kurdahi, Professor Wang, Professor Ayanoglu, Professor Veidenbaum and Professor Taha.

I would like to thank Frank Carr for mentoring and sharing his industry experience which was critical for building and troubleshooting our experimental full-duplex wireless system.

I would like to acknowledge the support and the cooperative work with the Wireless System and Circuits Lab (WSCL) members. The discussions and technical support provided by Dr. Alireza S. Behbahani and Dr. Elsayed Ahmed were very crucial in the successful completion of this project.

I would like to acknowledge the support of the WSCL members Ahmed Ibrahim, Mohammed Fouda, Davit Hovhannisyan.

VITA

Sergey Shaboyan

EDUCATION

Doctor of Philosophy in Electrical Engineering **2020**
University of California Irvine *Irvine, California*

Master of Science in Electrical Engineering **2010**
University of California Los Angeles *Los Angeles, California*

Bachelor of Science in Electrical Engineering **2009**
University of California Los Angeles *Los Angeles, California*

RESEARCH EXPERIENCE

PhD Student Researcher **2014–2020**
University of California, Irvine *Irvine, California*

M.S Student Researcher **2009–2010**
University of California, Los Angeles *Los Angeles, California*

WORK EXPERIENCE

Internship **2019–2020**
Intellisense Systems Inc. *Torrance, California*

Internship **2017–2018**
Lextrum Inc. *Irvine, California*

REFEREED JOURNAL PUBLICATIONS

Design and Implementation of an End-to-End Amplify and Forward Full-Duplex Relay Network — ***Submitted*** **March 2020**
IEEE Access

Application of ICA on Self-Interference Cancellation of In-band Full-Duplex Systems — **February 2020**
IEEE Wireless Communications Letters

Practical Considerations for Full-Duplex Enabled 5G Integrated Access and Backhaul — **Dec 2019**
Springer Journal of Signal Processing Systems

Active Cancellation of Self-Interference for Full-Duplex Amplify and Forward Wi-Fi Relay — **Dec 2018**
IEEE Wireless Communications Letters

REFEREED CONFERENCE PUBLICATIONS

Self-Interference Channel Characterization for Reconfigurable Antenna Based Systems — **Dec 2019**
Asilomar Conference on Signals, Systems, and Computers

Robust Frame Boundary Synchronization for In-Band Full-Duplex OFDM System — **Dec 2018**
Asilomar Conference on Signals, Systems, and Computers

Frequency and Timing Synchronization for In-Band Full-Duplex OFDM System — **Jan 2018**
IEEE Global Communications Conference

SOFTWARE

FDR TestBench — `C++`
Application for Amplify and Forward Full-Duplex Relay Control.

SRadio — `C++`
Application Layer for Software Defined Radio.

FDSim — `Matlab`
Full-Duplex Communication Simulator

HARDWARE

Amplify and Forward Full-Duplex Relay Prototype
A platform for Amplify and Forward Full-Duplex Relay research.

Full-Duplex Base Station Prototype
A platform for testing mobile to Full-Duplex base station link.

ABSTRACT OF THE DISSERTATION

Design and Implementation of Robust Full-Duplex Wireless Network

By

Sergey Shaboyan

Doctor of Philosophy in Electrical and Computer Engineering

University of California, Irvine, 2020

Professor Ahmed Eltawil, Chair

Recently Full-Duplex (FD) communication has gained significant interest due to demonstrable increase in throughput and spectral efficiency. Conventional Half-duplex (HD) communication systems use either time-duplexing or frequency-duplexing to avoid self-interference. In contrast, full-duplex systems transmit and receive simultaneously on the same frequency band, thus optimally utilizing available resources. The main challenge in FD systems is managing the self-interference (SI) signal at each node, which is typically orders of magnitude larger than the intended signal of interest (SOI). To achieve sufficient SI suppression, FD systems rely on cancellation across multiple domains such as spatial, analog, and digital. However, number of practical, FD specific challenges arise impacting quality of service, when at least one node in a network operates in full-duplex mode.

In this thesis, we consider practical issues of wireless networks containing a full-duplex node. The ultimate goal of this work is to design and implement real-time, end-to-end networks consisting of at least one FD node that is capable of improving network performance under limited available bandwidth constraint. First, we identify synchronization issues in a network consisting of a full-duplex base station communicating with half-duplex nodes. Novel synchronization techniques specific for full-duplex networks are proposed that allow compensation of synchronization errors in time and frequency. The proposed techniques are

implemented and tested experimentally on a real-time full-duplex wireless network. Second, we characterize the dynamic environment impact on the received self-interference in the FD system, which is equipped with a reconfigurable antenna as a passive SI suppression mechanism. The self-interference channel delay profile is measured using the FD system operating on 5MHz, 10MHz, and 20MHz bandwidths. The measured channel profiles collected under suppressing and non-suppressing antenna patterns are compared, and channel changes in static, as well as dynamic environments, are highlighted. We then statistically model the SI channel by performing probability distribution fitting to SI channel data. Third, the thesis proposes a Wi-Fi compliant self-interference active cancellation technique for amplify and forward, as well as decode and forward full-duplex relays. Finally, we design and implement an end-to-end wireless network extended with the aid of a custom-designed amplify and forward full-duplex relay. We then analyze the relay coverage limitation under the stability and transmit power constraints. The network performance is analyzed as a function of relay location for constant gain and constant transmit power modes, consequently suggesting optimal relay location that will maximize signal to noise plus interference ratio (SINR) at the destination node. We evaluate the overall network performance by simulation, as well as experimentally in outdoor/indoor environments.

Chapter 1

Introduction

1.1 Background

With the advent of 5G technology, there has been an increasing demand for wireless spectral resources due to a continuously growing number of wireless devices along with their bandwidth-hungry applications. In order to satisfy this demand, new approaches that maximize spectral efficiency are needed. In traditional wireless networks, nodes communicate in half-duplex mode, which means that they transmit and receive on two different frequency bands, time slots, or space codes. Therefore, half-duplex communication serves as an isolation mechanism between transmit and receive chains of the same node, such that the transmitting node does not receive its own transmitted signal. In a new approach, called full-duplex mode, transmission and reception takes place on the same frequency and in the same time slot, creating the potential of doubling the wireless spectrum utilization efficiency. However, simultaneous transmission and reception on the same frequency causes the transceiver to receive its own signal, often referred to as self-interference (SI). In order to be able to successfully receive the signal transmitted by the remote node, it is essential to

suppress the self-interference down to the noise floor. Suppression of SI is a major challenge in full-duplex communication since SI power is orders of magnitude larger than the power of the signal-of-interest (SOI). Large SI power requires a multistage cancellation chain, in order to suppress the SI down to the noise floor.

1.2 Self-Interference Suppression

A considerable amount of work has been done in developing various techniques for suppressing the self-interferer including passive as well as active SI cancellation. Passive SI suppression is performed in the propagation domain before transmitted SI reaches the receiver chain of the same node. This stage reduces some portion of SI, and in the meantime, helps to avoid saturation of the receiver front-end, which is crucial for the operation of subsequent stages down the chain. Passive SI suppression mechanisms such as separation between transmit and receive antennas, can be combined with antenna beamforming, beam steering, dual-polarization mechanisms, to create more than 65dB total passive SI suppression [27]. In the case, when a single antenna is used for simultaneous transmit and receive, circulators and/or dual-polarized antennas can be used to separate the transmit and receive signals [3].

Active SI cancellation is performed in the receiver chain. It is based on re-constructing the received SI from the known transmitted signal and subtracting it from the composite received signal. This operation can be carried out in both analog and digital domains, which is often referred to as analog SI cancellation and digital SI cancellation, respectively. Analog cancellation has been implemented using adaptive taps that allow destructive combining with received SI either at radio frequency (RF), intermediate frequency (IF), or at base-band (BB), before analog-to-digital (ADC) converter [22, 7, 8]. Digital SI cancellation is based on the same principle of active cancellation, but it is performed after the ADC. Since it is the last stage of suppression, an accurate SI channel estimation is required to construct and

cancel the remaining part of the SI. A common technique is the linear SI channel estimation, which in many cases, provides up to 30dB SI cancellation capability. However, the channel estimation accuracy of this technique is limited by several factors, such as phase noise of the local oscillator (LO) [2], nonlinearities caused by the power amplifier (PA) [1] and channel dynamics. Elimination of phase noise can be accomplished by linking the transmit and receive phase-locked loops (PLL). To capture nonlinearities, nonlinear SI channel estimation techniques have been developed that allow estimation of non-linearity coefficients iteratively [2], as well as with the aid of neural networks [28, 18].

1.3 Motivation

Since SI suppression is the main challenge enabling full-duplex communication, a lot of the work in full-duplex is dedicated to SI suppression techniques considering a single node transmitting and receiving in full-duplex mode. When a wireless network is constructed, a number of practical issues arise, requiring a specific approach in the case when at least one of the nodes communicates in FD mode. For example, a network consisting of half-duplex nodes and one full-duplex base station is facing challenges such as synchronization errors, degradation in SI suppression due to channel dynamics and relative position of the nodes. In the case when a full-duplex relay is added to an existing wireless network for coverage extensions purposes, a challenge of compliance with standardized protocol arises, forcing the FD relay to follow predefined guidelines. In a network with multiple full-duplex nodes, such as a tandem full-duplex relay network, the challenge of inter-relay interference arises, where every relay besides SI is receiving interference from other FD nodes [12].

With these challenges in mind, the design and implementation of a robust full-duplex network and demonstrating its performance in realistic channels is the main motivation behind the work in this thesis.

1.4 Thesis Contributions

In this thesis, practical issues of wireless networks containing a full-duplex node are considered. Several critical issues impacting network performance are investigated analytically as well as experimentally, and resolutions are proposed addressing them. The key contributions of the thesis can be summarized as follow:

1. *"Synchronization errors estimation and compensation in full-duplex communication".*
   There is a significant amount of research dedicated to synchronization error compensation techniques for nodes transmitting in HD mode. However, in FD mode, the received signal consists of a superposition of two streams transmitted by two different sources, where each signal stream experiences a different amount of time, frequency misalignment and various channel impairments. In this thesis, novel timing and frequency offset compensation techniques for full-duplex communication are proposed that allow successful suppression of SI in the digital domain and SOI recovery. In addition, the effectiveness of the proposed techniques are confirmed by simulation and experiments.

2. *"Robust frame boundary synchronization in a full-duplex OFDM system".*
   Two scenarios where the received frame is corrupt with SI in a way that drives the detection mechanism into false frame edge detection are identified. An improved frame boundary detection technique is proposed and shown to be immune against large SI levels and shifts in time, providing robust and accurate frame edge detection.

3. *"Self-interference channel characterization for the systems with re-configurable antenna".*
   SI variations have a significant impact on full-duplex communication. As presented in contribution 2, SI variations can create synchronization errors degrading system performance substantially. In the FD systems, where the re-configurable antenna is used as a passive SI suppression mechanism, SI variations can lead to non-optimal antenna

pattern selection resulting in poor SI suppression and, in some cases, a saturation of the receiver front end. In order to realistically model the SI, the SI channel is studied in various environments and time and frequency comparisons for narrow-band as well as wide-band wireless transmissions are presented. In addition, the SI channel is modeled statistically by fitting probability distributions and comparing them using the goodness of fit test.

4. *"Active SI Cancellation for a full-duplex relay in Wi-Fi network".*

   After demonstrating a peer to peer network, operating synchronously in full-duplex mode, a question arises whether full-duplex relaying is possible in already standardized Wi-Fi network. In contributions 1-3, to support digital cancellation and synchronization, a custom frame structure has been used, which is different from what is mandated in the Wi-Fi protocol. In order to enable the full-duplex relaying in the Wi-Fi network, novel techniques of channel estimation and synchronization are proposed that allow amplify and forward as well as decode and forward relays to operate using a standard Wi-Fi frame structure. System performance is evaluated in static and dynamic channels.

5. *"Design and Implementation of an end-to-end AF-FDR network".*

   As a next step, the design and implementation challenges of a network extended with the aid of amplify and forward full-duplex relays are considered. The coverage limitations of the full-duplex relay are analyzed under limited self-interference cancellation capability, and available transmit power constraints. The SINR analysis of tandem connected full-duplex relay network is carried out and back to back patch antennas are designed to eliminate inter-relay interference. In addition, the network performance is analyzed depending on the relay location, for the cases when the relay operates in constant gain and constant transmit power modes. Finally, the end-to-end wireless network extended with custom-designed AF-FDR is constructed, and performance is

evaluated experimentally in outdoor and indoor environments.

1.5 Thesis Organization

The rest of the thesis is organized as follows. In chapter 2, the frequency and timing synchronization of the in-band full-duplex OFDM system consisting of a base station and a remote node is presented. A robust frame boundary synchronization method for full-duplex communication is proposed in chapter 3. The self-interference channel is characterized in chapter 4, for a full-duplex system equipped with a reconfigurable antenna. In chapter 5, a Wi-Fi network extended by amplify and forward full-duplex relay is considered, and the Wi-Fi compliant active cancellation technique of self-interference is presented. The design and implementation challenges of an end-to-end amplify and forward full-duplex network are presented in chapter 6. Finally, the thesis is concluded in chapter 7.

Notation

We use $(*)$ to denote convolution, $(.)^*$ to denote conjugate, $E[.]$ to denote expectation, and $arg[.]$ to denote argument of a complex number. Time domain variables are represented as lowercase letters, while frequency domain variables use uppercase. Furthermore, bold lowercase letters indicate vectors.

Chapter 2

Frequency and Timing Synchronization for In-Band Full-Duplex OFDM System

2.1 Introduction

In-Band Full-Duplex (IBFD) communication is rapidly becoming accepted as a means of improving spectral efficiency in order to efficiently utilize limited frequency spectrum. On the other hand, Orthogonal Frequency Division Multiplexing (OFDM) is a well established modulation of choice, providing wideband, high rate, wireless communication service. Combining IBFD with OFDM has the potential to double the system throughput, when compared to their Half Duplex (HD) counterparts [41]. However, OFDM system performance can be substantially degraded due to frequency synchronization errors between transmitter and receiver [48]. The problem becomes compounded in IBFD-OFDM systems, due to the presence of strong self-interference (SI) in the received signal, which must be coherently canceled in

order to provide a satisfactory level of signal to interference plus noise ratio (SINR). Synchronization errors occur when the frequency of the local oscillator in the transmitter and receiver are mismatched, causing carrier frequency offset (CFO) and sampling time offset (STO).

OFDM synchronization issues for HD communication systems is a well researched and understood problem [35]. Synchronization mechanisms which employ a Direct Sequence Spread Spectrum signal on a single carrier frequency were proposed in [40]. Timing offset in full-duplex relays was studied in [54], where the timing offset is a result of propagation delay. However, compensation techniques developed for HD do not account for the presence of a large self-interferer (SI) within the band of interest, and therefore become inapplicable, in their current forms, to operate in FD systems, which rely on SI cancellation across multiple domains (spatial, analog and digital cancellation) to operate.

In this chapter, we identify and analyze impairments due to synchronization errors in IBFD-OFDM systems. We then develop techniques that address synchronization error compensation in FD communication. Specifically, the chapter presents the following contributions:

- A simple modification to the training frame structure of WiFi is used to allow for non-overlapping training of the SI and signal of interest (SOI) signals for synchronization proposes.
- A novel receiver architecture is presented for simultaneous SI cancellation and STO/CFO impairment recovery.
- Performance of the system impacted by synchronization error is evaluated using Matlab simulation, and experimentally tested on real time IBFD-OFDM software-defined radio (SDR) platform.

The remainder of the chapter is organized as follows. In Section 2.2, IBFD system combined

with OFDM is described and transceiver asynchronous operation is presented. In Section 2.3, techniques are proposed addressing STO and CFO. Theoretical SINR bound computation is presented in Section 2.4. Performance results of theoretical, simulated and experimental systems are presented and compared in 2.5. The chapter is concluded in Section 2.7.

2.2 Full Duplex System

Figure 2.1 illustrates a wireless system operating in full-duplex mode. The system consists of base station receiving from a remote node, at the same time transmitting to another node in the same frequency band. Signals transmitted by the remote node to the base station are referred to as SOI. The transmitted signal by the base station causes SI, therefore the received signal by the base station in the time domain can be modeled as

$$r(t) = s^{rx}(t) + y^{rx}(t) + w(t) \tag{2.1}$$

where $s^{rx}(t)$ and $y^{rx}(t)$ are SOI and SI components of the received signal. $w(t)$ is Additive White Gaussian Noise (AWGN).

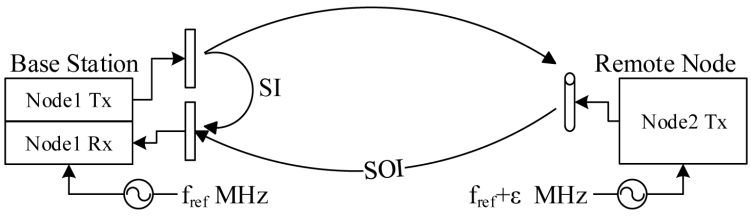

Figure 2.1: Block diagram of full duplex system.

From Eq. (2.1) it is clear that SI must be suppressed in order to achieve satisfactory SINR for the received signal. Numerous techniques are available for SI suppression including passive (eg. antenna separation, directional antennas etc.) and active (analog and digital cancellation). In analog cancellation, subtraction of the self generated SI signal is typically

performed before the low noise amplifier, using multi-tap RF filters that mimic the SI wireless channel. If a single antenna is used, RF circulators can be used to provide isolation. In the digital domain, remaining self interference is removed by estimating the SI channel. Other sources of noise such as phase noise and non-linearity are typically addressed by using a single Phase Locked Loop (PLL) to drive both transmit (Tx) and receive (Rx) chains, improving the linearity of both Tx and Rx chains, and using non-linearity estimation loops [41],[1].

2.3 Proposed Full Duplex System

Figure 2.2 presents a simplified equivalent system model of a FD system reflecting STO and CFO impairments. All nodes use OFDM that employs N_{FFT} subcarriers with inter-carrier spacing Δf. For sampling frequency f_s, subcarrier spacing is computed as

$$\Delta f = \frac{f_s}{N_{FFT}} = \frac{1}{N_{FFT}T_s} = \frac{1}{T_{sym}} \tag{2.2}$$

where T_s is sampling period and T_{sym} is one OFDM symbol duration.

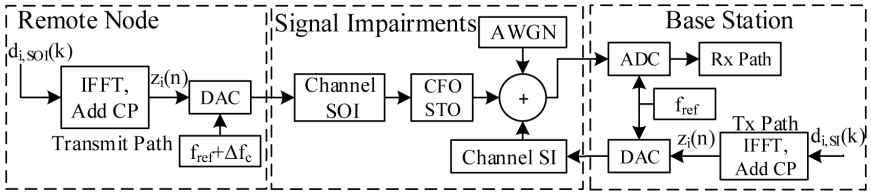

Figure 2.2: OFDM transmit path model with signal impairments.

2.3.1 OFDM Transmitter and Proposed Frame Structure

At the transmitter, for the i^{th} dataset, vector $\boldsymbol{d_i}$ consisting of N_d data symbols and M pilots is constructed and modulated on the $N_{FFT} = N_d + M$ subcarriers using Inverse Fast Fourier Transform (IFFT), forming one OFDM symbol. The output of IFFT is collected into vector

$\boldsymbol{z_i}$=$[z_i(0), z_i(1), ..., z_i(N_{FFT}-1)]^T$, where

$$z_i(n) = \begin{cases} \frac{1}{N_{FFT}} \sum_{k=0}^{N_{FFT}-1} d_i(k) e^{\frac{j2\pi kn}{N_{FFT}}} & 0 \leq n < N_{FFT} \\ 0 & otherwise \end{cases} \tag{2.3}$$

To avoid inter-symbol interference (ISI), a cyclic prefix (CP) of length of N_{CP} is pre-appended to each $\boldsymbol{z_i}$ block. Therefore the total number of time domain samples of each OFDM symbol duration is $N_T = N_{FFT} + N_{CP}$. Samples of each OFDM symbol are passed to the Digital to Analog Converter (DAC), up-converted to the carrier frequency f_c, and transmitted over the channel.

To support IBFD synchronization, the training fields for both the base station Tx and the remote node Tx are modified, such that they are non-overlapping as shown in figure 2.3. Training is divided into short and long preambles using the same structure as standard WiFi [23]. In the short preamble, short, repetitive, uncorrelated training sequences are used by each node to identify the frame start. In contrast, long training sequences are identical. A guard time (Trans) is inserted by the transmitter between fields and populated by zero vectors. The length of the guard period is a function of the maximum allowable drift in time and frequency. The data symbols of both Tx frames are fully overlapping.

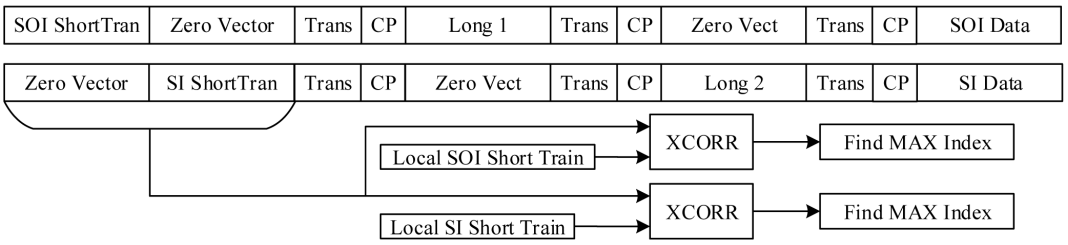

Figure 2.3: OFDM frame structure and short training cross-correlator structure.

2.3.2 Channel Model

Figure 2.2 illustrates the channel model used for simulation purposes to represent both SOI and SI propagation. SOI channel, h_{soi}, is modeled to reflect path loss and Rayleigh fading effects. SOI is impacted by carrier frequency offset (CFO) and sampling time offset (STO) due to the local oscillator (LO) mismatch Δf_c. CFO can be modeled as a constant positive or negative frequency shift. STO is modeled as fractional delay filter, which applies time-varying lead or lag.

The SI channel, h_{si}, is modeled to reflect path loss and Rayleigh fading effects. In addition, it assumes the use of passive self interference suppression (up to 70 dB passive SI suppression at 2.4 GHz, at 10 cm separation between Tx and Rx base station antennas) due to the use of reconfigurable directional antenna at the Receive port as described in [1]. The SI signal does not experience either CFO or STO because both the transmitter and receiver are co-located at the base station and share the same clock frequency. Finally, AWGN is added to the composite signal containing a superposition of the two signals.

2.3.3 IBFD-OFDM Receiver

At the receiver, the signal is down-converted to baseband and sampled using an Analog to Digital Converter (ADC) (figure 2.2). Due to the fact that the remote node uses a separate, asynchronous clock from that of the transmitter, a mismatch in the remote node transmitter's local oscillator (LO_{TX}) and receiver's local oscillator (LO_{RX}) frequency and phase is inevitable and will also be slowly time variant. Thus, their generated frequencies will be off by Δf_c resulting in CFO. The DAC at the remote node transmitter and the ADC at the receiver are also driven by LO_{TX} and LO_{RX} respectively, thus, after digitization, the received signal samples will experience STO. Therefore, the received i^{th} block of data $\boldsymbol{u_i}$ can

be expressed as follows:

$$u_i(n) = e^{\frac{j2\pi\Delta f_c}{f_s}} s_i^{tx}(n-\theta) * h^{soi}(n) + y_i^{tx}(n-\tau) * h^{si}(n) + w(n)$$

$$u_i(n) = e^{\frac{j2\pi\varepsilon n}{N_{FFT}}} s_i^{tx}(n-\theta) * h^{soi}(n) + y_i^{tx}(n-\tau) * h^{si}(n) + w(n) \tag{2.4}$$

where $s^{tx}(t)$ and $y^{tx}(t)$ are SOI and SI components of the transmitted signal. ε is the relative carrier frequency error, defined as $\varepsilon = \Delta f_c/\Delta f$, θ represents time shift of SOI due to STO, and τ represents time shift of SI due to channel delay. Time offset θ is a gradually increasing quantity which can have integer, as well as, fraction parts $\theta = \theta_{in} + \theta_{fr}$. Offset τ is relatively constant and represents an integer quantity.

As compared to half-duplex, in full-duplex communication, the received signal represents the superposition of two signals transmitted by two different transmitters as shown in Eq. (2.4). Directly applying a correction to the composite signal, will always lead to having one signal component corrected, while corrupting the other. i.e. if the SOI component is compensated for in the composite signal, the SI component will be corrupted, since operations performed on the received signal will affect both signal components. For proper demodulation, the receiver must recover the transmitted signal $s_i^{tx}(n)$ from $u_i(n)$.

Figure 2.4 illustrates the block diagram of an OFDM receiver supporting IBFD synchronization. The shaded blocks in the figure indicate processing steps that are novel to this architecture as opposed to a standard OFDM receiver. Frame edge detection is performed based on the modified frame structure presented in section 2.3.1. The digital cancellation block is modified to account for the estimated timing and frequency offsets, while performing SI cancellation as will be discussed later in the chapter. A key difference in this architecture is that STO is performed *after* digital cancellation rather than at the beginning of the receive chain. The reason this approach is needed in FD systems is to avoid SI corruption when

performing SOI CFO/STO correction. In the following section we present an overview of the building blocks, while highlighting the sequence of operations necessary for recovering the transmitted signal $s_i^{tx}(n)$. Detailed descriptions of each block are presented in subsequent sections.

Receiver Signal Processing Flow

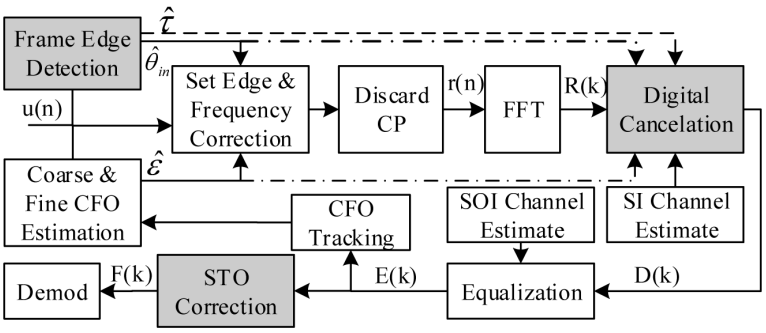

Figure 2.4: OFDM receiver diagram with IBFD synchronization.

First, the receiver estimates initial SI time offset τ, the integer part of the SOI sampling offset θ_{in} and frequency offset ε. The estimated time offset is removed from the received signal $u_i(n)$ for proper Fast Fourier Transform (FFT) window placement over SOI, followed by SOI complex phase rotation compensation as shown below

$$r_i(n) = u_i(n + \hat{\theta}_{in}) \cdot e^{-\frac{j2\pi\hat{\varepsilon}n}{N_{FFT}}} \tag{2.5}$$

where $\hat{\theta}_{in}$ is the estimated integer part of sampling offset θ and $\hat{\varepsilon}$ is estimated frequency offset. Once SOI is free of CFO and FFT window is aligned with its i^{th} block, the CP is discarded and the FFT is computed. The output of the FFT is vector $\boldsymbol{R}$ with length N_{FFT} and can be expressed as

$$R(k) = S^{tx}_{\theta_{fr}}(k)H_{soi}(k) + Y^{tx}_{\tau-\hat{\theta}_{in}}(k + \hat{\varepsilon})H_{si}(k) + W(k) \tag{2.6}$$

where $S^{tx}(k)$ and $Y^{tx}(k)$ are frequency domain representations of $s^{tx}(n)$ and $y^{tx}(n)$ respectively, subscript $\tau - \hat{\theta}_{in}$ indicates shift in time domain in positive direction. $H_{soi}(k)$ and $H_{si}(k)$ are frequency domain representations of $h_{soi}(k)$ and $h_{si}(k)$ respectively.

To perform digital cancellation, the receiver must construct the interferer as accurately as possible to match the interferer term given in Eq. (2.6). For this reason, the digital canceler utilizes the knowledge of the estimated initial SI time offset $\hat{\tau}$, estimated integer sampling offset $\hat{\theta}_{in}$, estimated frequency offset $\hat{\varepsilon}$, and Lest Square (LS) estimate of SI channel $\hat{H}_{si}(k)$. Therefore, vector at the output of digital canceler is denoted $\boldsymbol{D}$, and can be expressed as

$$D(k) = S^{tx}_{\theta_{fr}}(k)H_{soi}(k) + Y^{tx}_{\tau-\theta_{in}}(k+\hat{\varepsilon})H_{si}(k) - Y^{tx}_{\tau-\theta_{in}}(k+\hat{\varepsilon})\hat{H}_{si}(k) + W(k)$$

$$D(k) = S^{tx}_{\theta_{fr}}(k)H_{soi}(k) + W_{si}(k) + W(k) \tag{2.7}$$

where $W_{si}(k)$ is the residual uncompensated self-interference, and is due to SI channel estimation error.

To remove the channel effect H_{soi} impacting $S^{tx}(k)$, the receiver performs equalization by estimating the channel $\hat{H}_{soi}(k)$ of SOI using LS estimation and compensating for it. The vector at the output of equalizer is denoted $\boldsymbol{E}$ can be expressed as

$$E(k) = S^{tx}_{\theta_{fr}}(k)\frac{H_{soi}(k)}{\hat{H}_{soi}(k)} + W_{si}(k) + W(k)$$

$$E(k) = S^{tx}_{\theta_{fr}}(k) + W_{soi}(k) + W_{si}(k) + W(k) \tag{2.8}$$

where $W_{soi}(k)$ is the residual uncompensated channel effect on the $S^{tx}(k)$ signal, that appears as an additional noise term, and is due to SOI channel estimation error.

At this point the signal of interest is still impacted with fractional sampling time offset θ_{fr},

which has a gradually increasing nature due to the time drift. In general, channel equalization compensates for fractional timing offset, however for long OFDM frames, symbols located farther away from the training, gain additional fractional offset and undergo degradation in SINR.

To compensate for the fractional timing offset, receiver estimates additional channel change $\hat{H}_{ep}(k)$ on a per symbol basis, and compensates for it. Output of the timing offset correction block can be expressed as

$$F(k) = S^{tx}(k) + W_{ep}(k) + W_{soi}(k) + W_{si}(k) + W(k) \tag{2.9}$$

where $W_{ep}(k)$ is an additional noise term per-symbol channel estimation error. At this point, $F(k)$ consists of only $SOI^{tx}(k)$ plus noise terms. As a last step, $F(k)$ is forwarded to the demodulator for data extraction.

2.4 Compensation Algorithms

In this section, we discuss the details of the compensation techniques used to recover the signal of interest, while allowing for the successful operation of the digital canceler.

2.4.1 Sampling Time Offset Correction

Sampling time offset adds/removes fractional samples to the received signal creating drift in time and causing inter-carrier interference (ICI). Accumulating fractional samples over time results in integer sample shifts creating symbol timing offset, which causes ISI, due to the incorrect placement of the FFT window [33]. In the following, we first consider the effect of STO on the FD system, where $\Delta f_c = 0$ in (2.4). Under this condition (2.4) can be rewritten

as

$$u_i(n) = s_i^{tx}(n-\theta) * h_{soi}(n) + y_i^{tx}(n-\tau) * h_{si}(n) + w(n)\ . \tag{2.10}$$

In order to perform digital cancellation of SI and extract data from SOI, it is essential to locate the edges of both signal components and compensate for their offsets.

Symbol Timing Offset

To estimate $\hat{\theta}_{in}$ receiver cross-correlates the local copy of SOI training sequence with the received signal $u_i(n)$, and searches for peak position as described below

$$\hat{\theta}_{in} = \arg\max_n \Big[\sum_{m=1}^{W_d} u_i(m) \cdot p_{soi}^*(m+n) \Big] \tag{2.11}$$

where $p_{soi}(n)$ is the local copy of SOI short training, and W_d is correlation window width. To estimate $\hat{\tau}$, receiver cross-correlates the local copy of SI training sequence with received signal $u_i(n)$, and searches for peak position as described below

$$\hat{\tau} = \arg\max_n \Big[\sum_{m=1}^{W_d} u_i(m) \cdot p_{si}^*(m+n) \Big] \tag{2.12}$$

where $p_{si}(n)$ is the local copy of SI short trainings. The correlation window width W_d dictates that the synchronization error must be within a tolerable range. For that reason the receiver must exploit a pilot signal transmitted by the transmitter and readjust transmission start time.

Relative offset between signal components $s_i^{rx}(n)$ and $y_i^{rx}(n)$ is defined as $\Delta t = \hat{\theta}_{in} - \hat{\tau}$. Depending on the amount of Δt, we distinguish 3 cases:

Case 1: If $\Delta t = 0$ there is no relative offset between $s_i^{rx}(n)$ and $y_i^{rx}(n)$, the two data blocks are aligned and the problem reduces to HD synchronization.

Case 2: If $\Delta t > 0$, $y_i^{rx}(n)$ is shifted to the left with respect to $s_i^{rx}(n)$ as shown in figure 2.5a. The receiver aligns FFT window with SOI edge by removing time shift θ_{in} from the received signal $u_i(n)$ in (2.10). As a result, the SOI component in received $r_i(n)$ block does not have integer time offset, however SI component does. SI component that falls between $s_i^{rx}(n)$ boundaries is denoted as $y_{s_i}^{rx}(n)$. In this case, the $s_i^{rx}(n)$ is overlapped with y_i^{rx} as well as y_{i+1}^{rx}. To construct a SI copy matching to $y_{s_i}^{rx}(n)$, the digital canceler has to concatenate a portion from the current SI symbol and a portion from the next SI symbol, expressed as

$$y_{s_i}^{rx}(n) = \begin{cases} y_i^{rx}(n + \Delta t) & 0 \leq n < N_{FFT} - \Delta t \\ y_{i+1}^{rx}(n + \Delta t - N_{CP}) & N_{FFT} - \Delta t \leq n < N_{FFT} \end{cases} \tag{2.13}$$

Case 3: $\Delta t < 0$, $y^{rx}(n)$ is shifted to the right with respect to $s^{rx}(n)$. There are two scenarios $|\Delta t| \leq N_{CP}$ and $|\Delta t| > N_{CP}$.

Consider a small relative shift $|\Delta t| \leq N_{CP}$ as depicted in figure 2.5b. It is clear that the extracted data block $r_i(n)$ contains y_i^{rx} that is cyclically shifted by $|\Delta t|$ to the right. For this reason, the digital canceler has to construct a cyclically shifted (by $|\Delta t|$) copy of SI (2.14), to perform proper cancellation.

$$y_{s_i}^{rx}(n) = \begin{cases} y_i^{rx}(n + N_{FFT} - |\Delta t|) & 0 \leq n < |\Delta t| \\ y_i^{rx}(n - |\Delta t|) & |\Delta t| \leq n < N_{FFT} \end{cases} \tag{2.14}$$

In many applications CP is shortened to increase data throughput of the system. In order to increase tolerable range of symbol time offset, it is useful to consider the case when $|\Delta t| > N_{CP}$ figure 2.5c. Here again the receiver aligns the FFT window with s_i^{rx} edge. In this case extracted $r_i(n)$ block contains y_i^{rx}, its CP, as well as y_{i-1}^{rx}. To properly handle digital cancellation, receiver has to buffer and concatenate current and previous interferer symbols (2.15). Implementation of this technique extends error tolerance to additional N_{FFT}

samples, resulting in total correction ability of $N_{CP} + N_{FFT}$ samples relative offset.

$$y_{s_i}^{rx}(n) = \begin{cases} y_{i-1}^{rx}(n + N_{FFT} - |\Delta t| + N_{CP}) & 0 \leq n < |\Delta t| - N_{CP} \\ y_i^{rx}(n + N_{FFT} - |\Delta t|) & |\Delta t| - N_{CP} \leq n < |\Delta t| \\ y_i^{rx}(n - |\Delta t|) & |\Delta t| \leq n < N_{FFT} \end{cases} \tag{2.15}$$

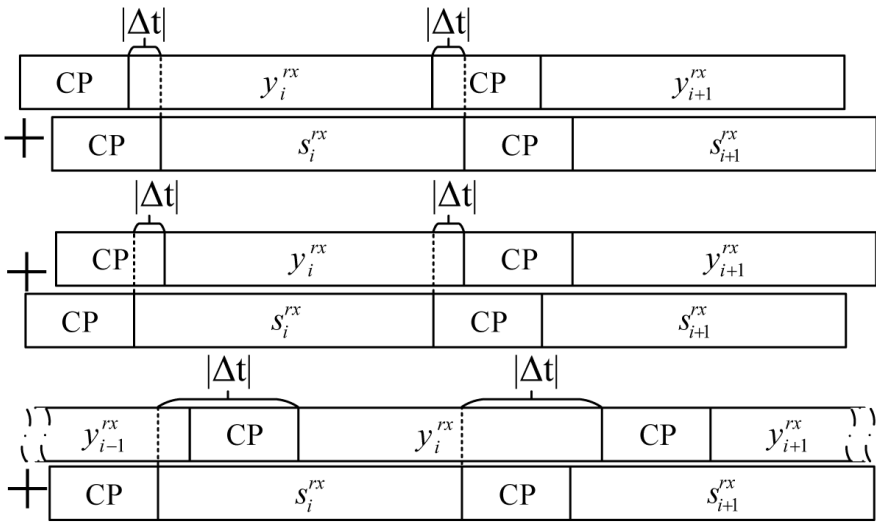

(a) $\Delta t > 0$

(b) $\Delta t < 0$, $|\Delta t| \leq N_{CP}$

(c) $\Delta t < 0$, $|\Delta t| > N_{CP}$

Figure 2.5: Received OFDM symbols with relative offset Δt.

Fractional Timing Offset

It is important to note that in all cases described above only integer part of the offset is estimated and compensated, but the fractional part remains. There are two effects due to fractional offset.

First, fractional time offset can create rounding error in correlation based boundary detection algorithm, which will misplace the FFT window by one sample. Rounding down error places FFT window early over SOI data by one sample, running into the cyclic-prefix. This causes a cyclic shift of SOI data, which is automatically compensated by equalization. Rounding up error places the FFT window late, running into the next symbol, destroying orthogonality

and causing ISI. To prevent system degradation due to rounding up errors, constant N_b sample back off is used, where $N_b < N_{CP}$. Which means that instead of taking the data of one symbol duration from s_i^{rx} edge, receiver takes it from the point shifted towards the CP by N_b samples. This insures FFT window placement to be strictly within one OFDM symbol.

Second, fractional offset causes phase shift in the received signal. This can be partially handled by the equalizer, that uses channel estimates from the OFDM training sequence. The remainder can be compensated by additional equalization using channel estimates acquired from embedded pilots in each symbol.

2.4.2 Carrier Frequency Offset

CFO in OFDM system introduces amplitude reduction, phase shift and ICI [48]. Consider the received signal in FD system impacted only by CFO. Setting $\theta = 0$, $\tau = 0$ in (2.4) we get

$$u_i(n) = e^{\frac{j2\pi\varepsilon n}{N_{FFT}}} s_i^{tx}(n) * h_{soi}(n) + y_i^{tx}(n) * h_{si}(n) + w(n) \tag{2.16}$$

Relative frequency offset can be written as a sum of integer and fractional relative frequency offsets. $\varepsilon = \varepsilon_{in} + \varepsilon_{fr}$ where ε_{in} is the frequency offset integer multiple to subcarrier spacing, and ε_{fr} is the frequency offset fractional multiple to subcarrier spacing.

After identifying the incoming frame edge as described in the previous section, the receiver proceeds to perform coarse frequency offset estimation, fine frequency offset estimation, frequency offset compensation and tracking.

During coarse frequency offset estimation, the receiver estimates the relative integer frequency offset ε_{in} by correlating the received training sequence with its shifted original copy

in the frequency domain [33], and finding the peak position as follows

$$\hat{\varepsilon}_{in} = \arg\max_{k} \Big[\sum_{m=0}^{N_T-1} V_{rx}(m) \cdot V_o^*(m+k) \Big] \tag{2.17}$$

where $V_{rx}(m)$ and $V_o(m)$ are the received and original long training sequences in the frequency domain.

Then it uses repetitive time domain patterns of preamble to estimate remaining offset, which is a fraction of subcarrier spacing. The receiver takes the phase difference of two repetitive training blocks and relates that to the frequency offset by

$$\hat{\varepsilon}_{fr} = \frac{N_{FFT}}{2\pi N_p} \arg \Big[\sum_{m=0}^{N_P-1} q_{soi}(m) \cdot q_{soi}^*(m+N_P) \Big] \tag{2.18}$$

where $q_{soi}(m)$ is a single received block in the repetitive SOI preamble, and N_p is its repeating period.

The receiver compensates the received data symbols with the estimated frequency offset value $\hat{\varepsilon}$, and readjusts the estimate by tracking the frequency offset on a symbol by symbol basis, using inserted pilots.

To compensate for CFO, the receiver uses the estimated CFO value $\hat{\varepsilon}$ and counter rotates the received signal $u_i(n)$, as shown in (2.19). This compensates frequency offset of SOI, but also rotates the SI component.

$$r_i(n) = u_i(n) \cdot e^{-\frac{j2\pi\hat{\varepsilon}n}{N_{FFT}}} = s^{tx}(n) * h_{soi}(n) + y^{tx}(n) * h_{si}(n) \cdot e^{-\frac{j2\pi\hat{\varepsilon}n}{N_{FFT}}} + w(n) \tag{2.19}$$

From expression (2.19) it is clear that the digital canceler must know the value of $\hat{\varepsilon}$ and rotate the constructed interferer accordingly.

2.5 SINR Computation

At the demodulation step, the signal consisting of SOI and noise components is expressed in (2.9), with four major noise sources, namely, AWGN, residual uncompensated self interference, SOI channel estimation errors, and per symbol timing correction errors.

For simplicity, in the following SINR analysis we focus on the four major noise contributing terms identified earlier, and do not account for other secondary sources such as IQ imbalance, non-linearities, phase noise, severe fading channel, Doppler, multipath etc. Thus, the computed theoretical SINR can serve as an upper bound for achievable SINR as follows:

$$SINR = \frac{P_{SOI}}{P_N + P_e^{SOI} + P_e^{SI} + P_{ep}^{SOI}} \tag{2.20}$$

where P_{SOI} is the power of SOI, P_N is the power of AWGN W(k) with variance σ_N^2. P_e^{SOI}, P_e^{SI} and P_{ep}^{SOI} are corresponding powers of $W_{SOI}(k)$, $W_{SI}(k)$ and $W_{ep}(k)$.

At the channel estimation step, the receiver estimates the channel by computing the ratio of received training sequence R(k) to the known training sequence X(k) in the frequency domain.

$$\hat{H}(k) = \frac{R(k)}{X(k)} = \frac{X(k)H(x) + W(k)}{X(k)} = H(k) + \frac{W(k)}{X(k)} \tag{2.21}$$

To compute the power of noise contributing terms P_e^{SOI}, P_e^{SI} and P_{ep}^{SOI}, we define channel estimation mean-square error (MSE) J as

$$J = \frac{1}{N_{FFT}} \sum_{k=1}^{N_{FFT}} \left[|H(k) - \hat{H}(k)|^2 \right] \tag{2.22}$$

Using (2.21) and the fact that AWGN $w(n)$ is independent of the transmitted sequence $X(k)$, and that the training sequence $X(k)$ is a unity power vector consisting of ± 1s, we can

compute (2.23) as

$$J = E\left[\left|\frac{W(k)}{X(k)}\right|^2\right] = E\left[\left|\frac{1}{X(k)}\right|^2\right] E[|W(k)|^2] = \sigma_N^2 \tag{2.23}$$

The result in (2.23) indicates that the estimation error over one OFDM symbol equals to the AWGN noise power. In the proposed estimation algorithm, we average the channel estimates $\hat{H}_{SOI}(k)$, $\hat{H}_{SI}(k)$ and $\hat{H}_{ep}(k)$ over ℓ OFDM symbols therefore

$$P_e^{SOI} = P_e^{SI} = P_{ep}^{SOI} = \frac{\sigma_N^2}{\ell} \tag{2.24}$$

Substituting (2.24) in (2.20), the SINR expression is simplified as

$$SINR = \frac{P_{SOI}}{P_N} \cdot \frac{\ell}{\ell + 3} \, . \tag{2.25}$$

2.6 Simulation and Experimental Results

All simulations and experiments are performed according to the parameters listed in Table 2.1. As a performance metric, SINR value is calculated at the demodulation step for various offset amounts measured in parts per million (ppm).

OFDM Parameters	**Value**	**Signal Parameters**	**Value**
Number of OFDM Subcarriers	64	Channel Type	D
Number of Data Subcarriers	44	Doppler Frequency	10 Hz
Number of Pilots	4	AWGN Power	-100dBm
Cyclic Prefix (CP)	$3.2\mu s$	Rx SOI Power	-70 dBm
Symbol Duration (CP+FFT)	$16\mu s$	Rx SI Power	-65 dBm
Long Training Duration	$32\mu s$	Passive Cancelation	-70 dBm
Short Training Duration	$16\mu s$	Carrier Frequency	2.5 GHz
Subcarrier Frequency Spacing	78125Hz	Sampling Rate	5 MHz
Number of Symbols/Frame	100	Tx Power	5dBm

Table 2.1: Simulation parameters

2.6.1 Simulation

The full duplex system modeled in Figure 2.2 is simulated. Packets belonging to SOI are impacted with frequency and timing offset. Packets belonging to SI have passive suppression of 70dB due to the use of directional antennas as described in [1].
Using (2.25) and parameters in Table 1, the theoretical SINR bound is computed to be equal to 26dB. SINRs of theoretical, perfectly synchronized, synchronization error compensated and synchronization error uncompensated systems are presented in Figure 2.6.

From the figure, it is clear to see that the SINRs of theoretical, perfectly synchronized, synchronization error compensated are very close to each other up to 70 ppm and vastly improved as compared to an uncompensated system. Figure 2.7 illustrates the difference in SINR between the ideally synchronized and compensated systems as compared to theory. The ideally synchronized assumes perfect knowledge of the timing and frequency offset parameters at the receiver while the compensated system estimates these variables. At zero offset, both systems show a fixed offset from theory which grows gradually for the compensated system. However, even at 70 ppm, only 0.7dB of degradation is recorded.

2.6.2 Experimental Setup

A complete full-duplex experimental system is constructed using the Universal Software Radio Peripheral (USRP) SDR platform. Each USRP contains a Radio Frequency (RF) transceiver and a Field Programmable Gate Array (FPGA). All USRPs are connected to a host PC through a Gigabit Ethernet connection. The baseband signal processing is performed over the host PC. The baseband signals are streamed to/from the USRPs at a rate of 25M sample/sec. The RF transceivers are then used for real time signal transmission and reception.

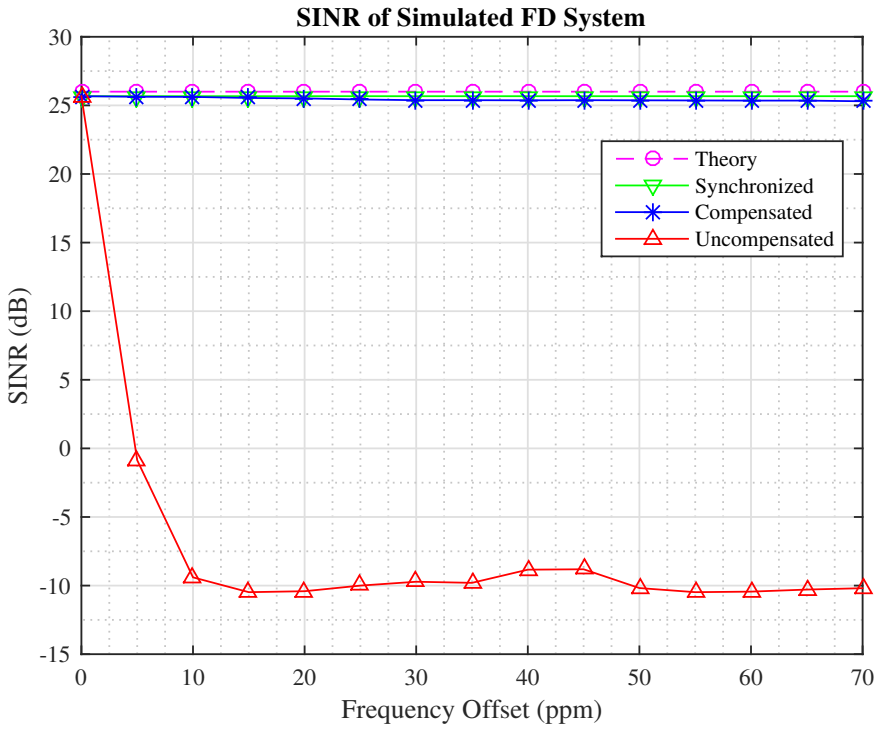

Figure 2.6: Performance of simulated FD system.

As shown in Figure 2.1, Node 1 is equipped with one transmit and one receive antenna. Node 2 uses only one antenna. A dipole omni-directional antenna is used as transmit antenna, while a reconfigurable directional antenna is used as a receive antenna. Both transmit and receive antennas have the same antenna polarization. The reconfigurable antenna has a total of 4096 different possible radiation patterns. A successful pattern, is a pattern that maximizes the SOI signal and minimizes the SI signal. The pattern selection is performed through a 12-line digital control cable driven from an FPGA on a Zedboard. The timing of all USRPs and the FPGA that drive the antenna radiation selection are aligned with one reference Pulse Per Second (PPS) signal. A full description of the experimental setup for the FD platform is available in [1].

The reference clock is generated locally at each node. A sinewave generator, Agilent N9310, is used to generate the reference clock at node 2. This enables control over the reference clock frequency, to test system performance at different frequency offset amounts. Due

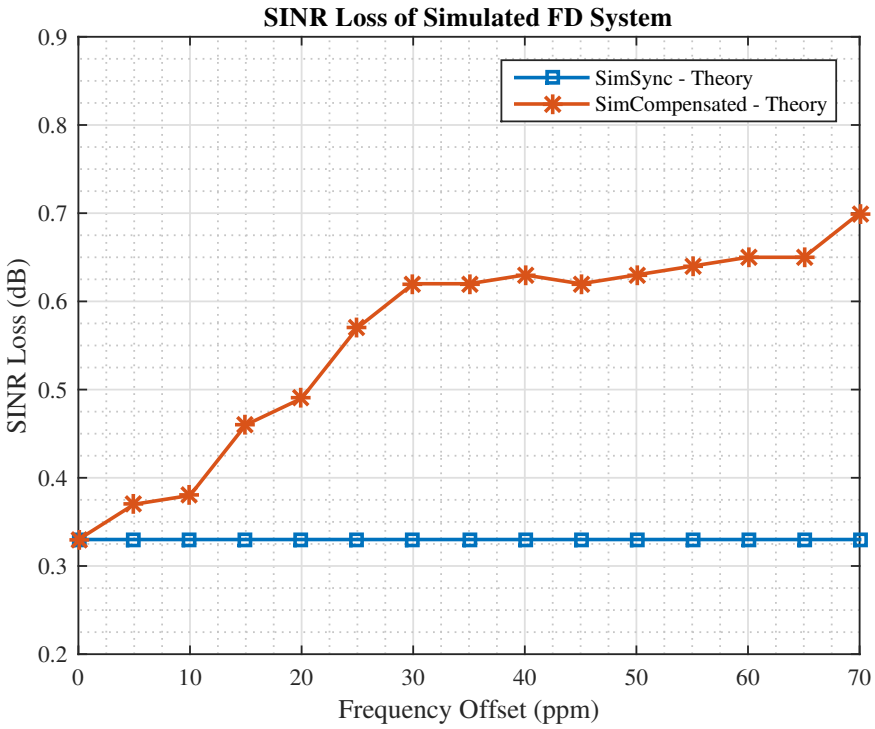

Figure 2.7: Performance degradation of simulated FD systems.

to measurement equipment reference clock offset tolerance limitation, the maximum offset possible is 25ppm.

2.6.3 Experimental Results

The full-duplex system described above was tested in a fully synchronized (by-wire synchronized), compensated and uncompensated modes, and performance was recorded. For each offset value, transmission of over 250 OFDM frames is performed. Each ppm value is set by tuning the reference frequency generator and verifying resultant frequency offset amount by the estimation algorithm running at the receiver. Experimental results are presented in Figure 2.8. To facilitate comparison, theoretical, simulated and experimental results, are overlapped in Figure 2.8.

Figure 2.9 illustrates the difference between the wired synchronized experimental system and

the compensated experimental system. At small offsets, no measurable difference is recorded up to 5 ppm, at which a degradation in the compensated system is measured and gradually increases, but remains within 0.5 dB up to 20 ppm. Between 20 ppm and 25 ppm, there is a sharp increase in SINR loss by 1dB, which is attributed to the measurement equipment reference clock offset operating at its limits.

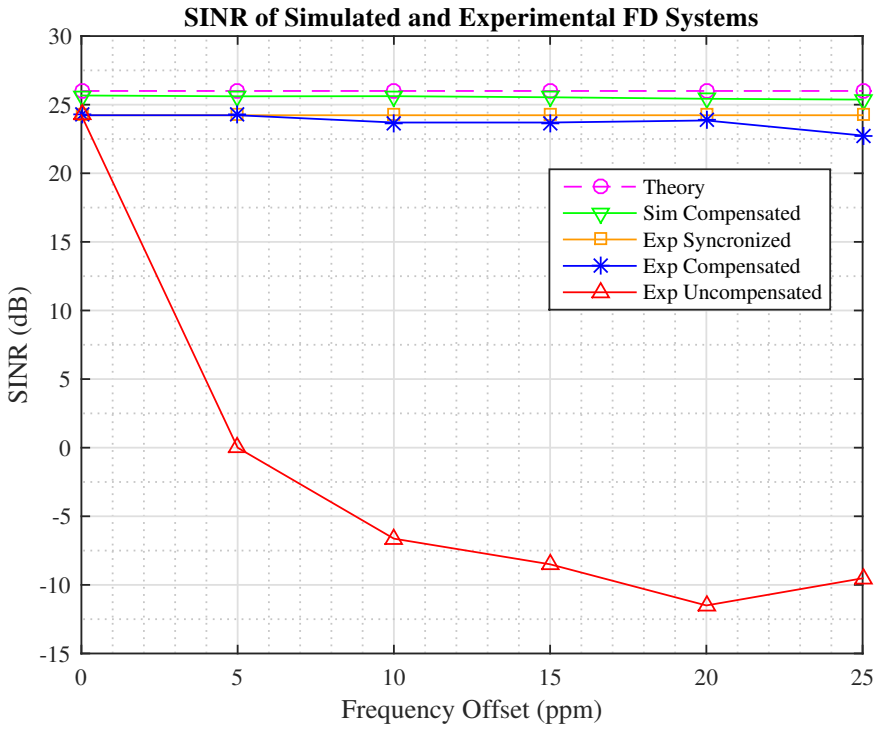

Figure 2.8: Performances of experimental and simulated FD systems.

2.7 Conclusion

This chapter presented a timing and frequency synchronization scheme for OFDM full-duplex systems. The major challenge in full-duplex system is the presence of self-interferer.A simple modification to the frame structure to support IBFD-OFDM frame edge detection and training is proposed. A novel wireless OFDM receiver architecture that compensates for timing and frequency offset while suppressing the self-interference is presented and its performance

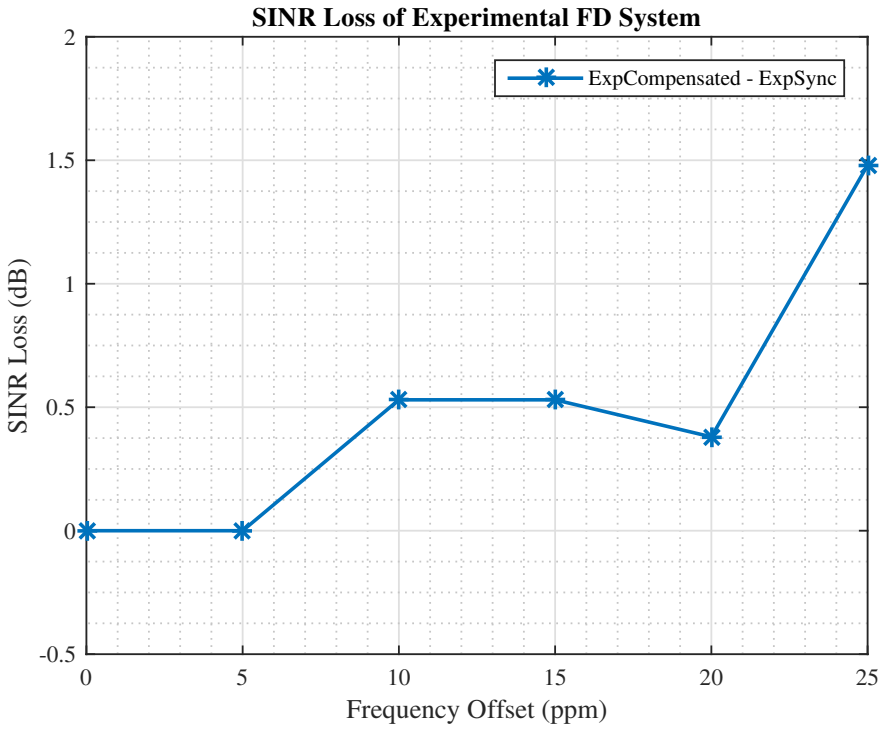

Figure 2.9: Performance degradation of experimental systems.

is analyzed. Simulation and experimental results generated on real time full-duplex platform are presented showing the effectiveness of the proposed technique in realistic indoor wireless environments.

Chapter 3

Robust Frame Boundary Synchronization for In-Band Full-Duplex OFDM System

3.1 Introduction

As presented in chapter 2, coupling FD with Orthogonal Frequency Division Multiplexing (OFDM) is a logical step towards achieving high spectral efficiency. However, the performance of OFDM-based FD systems can be substantially degraded due to frequency synchronization errors between transmitter and receiver [43].

Synchronization of wireless nodes employing OFDM has been studied by [30], and synchronization error compensation techniques were proposed assuming perfect channel state information. To estimate channel under severe timing and frequency offsets, the authors in [11] have proposed a customized frame structure of alternating pilots pre/post appended with guard intervals. A modified WiFi frame structure supporting synchronization using

insertion of guard intervals has been proposed in [43] as well, however insertion of guard intervals alone is insufficient for robust frame boundary detection. Under scenarios of severe time drift or substantially large SI, frame start detection fails to detect the correct edge causing incorrect placement of Fast Fourier Transform (FFT) window resulting in ISI and ICI as will be discussed in Section 3.4.

Since frame boundary detection is the first crucial step in the synchronization chain, in this chapter we will focus on identifying and analyzing the scenarios causing block boundary detection failure in FD mode. We then propose a technique enabling successful block boundary detection even under severe offsets. In particular, this chapter presents the following contributions:

- A novel block boundary detection technique relaxing requirement of guard interval separating short training sequences and boosting robustness of frame start detection algorithm is proposed.
- A novel receiver architecture is presented for simultaneous SI cancellation and STO/CFO impairment recovery.
- Performance of the system impacted by dynamic channel effects and synchronization errors is evaluated using Matlab simulation as well as experimentally on the real-time FD platform.

The remainder of the chapter is organized as follows. In Section 3.2 an IBFD system combined with OFDM is described. In Section 3.3 sources of timing and frequency misalignment effects are described and their impacts on SI cancellation are highlighted. In Section 3.5, robust block boundary detection technique (RBBD) of both SI and SOI is proposed. Functionality of RBBD is demonstrated experimentally in Section 3.6. Performance results of simulated system under different channel conditions is presented and compared in Section 3.7. The chapter is concluded in Section 3.8.

3.2 System Model

Figure 3.1 illustrates a wireless system operating in full-duplex mode. The system consists of base station (BS) receiving from a remote node, at the same time transmitting to another node on the same frequency band. Signals transmitted by the remote node to the base station are referred to as SOI. The transmitted signal by the base station causes SI, therefore the received signal by the base station in the time domain can be modeled as

$$r(t) = s^{rx}(t) + y^{rx}(t) + w(t) \tag{3.1}$$

where $s^{rx}(t)$, $y^{rx}(t)$ are SOI and SI components of the received signal, and $w(t)$ is Additive White Gaussian Noise (AWGN).

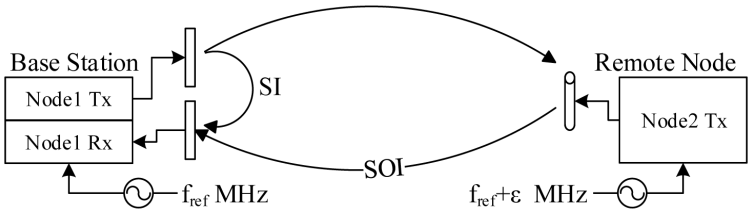

Figure 3.1: Diagram of full duplex relayed Wi-Fi Network.

From Eq. (3.1) it is clear that SI must be suppressed in order to achieve satisfactory SINR for the received signal.

Numerous techniques are available for SI suppression, including passive (eg. antenna separation, directional antennas etc.) and active (analog and digital cancellation). Both analog and digital cancellation techniques rely on subtraction of the local copy of SI in analog or digital domains respectively [44].

3.2.1 Transmitter

All nodes use packetized data transmission, where every data packet starts with a header consisting of training sequences. Training is divided into short and long preambles using similar structure as standard WiFi [23]. Both the base station Tx and the remote node Tx are using modified non-overlapping training fields to support IBFD synchronization as described in [43]. A guard time (Trans) is inserted by the transmitter between long training fields and populated by zero vectors to protect them from overlapping due to the time drift [11]. Short training fields are not separated by zero vectors, by virtue of proposed boundary detection technique that can tolerate partial overlap without performance degradation, which is discussed in details in Section 3.4. The data symbols of both Tx frames are fully overlapping.

All nodes use OFDM that employs N_{FFT} subcarriers with inter-carrier spacing Δf. For sampling frequency f_s, subcarrier spacing is computed as

$$\Delta f = \frac{f_s}{N_{FFT}} = \frac{1}{N_{FFT} T_s} = \frac{1}{T_{sym}} \tag{3.2}$$

where T_s is sampling period, f_s is sampling frequency and T_{sym} is one OFDM symbol duration.

At the transmitter, for the i^{th} dataset, vector $\boldsymbol{d_i}$ consisting of N_d data symbols and M pilots is constructed and modulated on the $N_{FFT} = N_d + M$ subcarriers using Inverse Fast Fourier Transform (IFFT), forming one OFDM symbol. The output of IFFT is collected into vector $\boldsymbol{z_i}$=$[z_i(0), z_i(1), ..., z_i(N_{FFT}-1)]^T$, where

$$z_i(n) = \begin{cases} \frac{1}{N_{FFT}} \sum_{k=0}^{N_{FFT}-1} d_i(k) e^{\frac{j2\pi kn}{N_{FFT}}} & 0 \leq n < N_{FFT} \\ 0 & \text{otherwise} \end{cases} \tag{3.3}$$

To avoid inter-symbol interference (ISI), a cyclic prefix (CP) of length of N_{CP} is pre-appended to each $\boldsymbol{z_i}$ block. Therefore the total number of time domain samples of each OFDM symbol duration is $N_T = N_{FFT} + N_{CP}$. Samples of each OFDM symbol are passed to the Digital to Analog Converter (DAC), up-converted to the carrier frequency f_c, and transmitted over the channel.

3.2.2 Receiver

Receiving node downconverts the signal to baseband and digitizes using Analog to Digital Converter (ADC). It then uses short training sequence to perform block boundary detection and coarse frequency offset estimation. It then uses long training field for channel estimation and fine timing/frequency offset estimation. The length of the guard period is a function of the maximum allowable drift in time and frequency. In the short preamble, short, repetitive, uncorrelated training sequences are used by each node to identify the frame start position associated with each signal component. In contrast, long training sequences are identical.

3.2.3 Channel Model

Figure 3.2 illustrates the channel model used for simulation purposes to represent both SOI and SI propagation. SOI channel, h^{soi}, is modeled to reflect path loss and Rayleigh fading effects. Since received packets are transmitted by nodes, randomly located in the cell, h^{soi} is modeled to reflect random discontinuity of SOI channel from packet to packet. SOI is impacted by carrier frequency offset and sampling time offset due to the local oscillator (LO) mismatch Δf_c. CFO can be modeled as a constant positive or negative frequency shift. STO is modeled as fractional delay filter, which applies time-varying lead or lag.

The SI channel, h_{si}, is modeled to reflect path loss and Rayleigh fading effects. Because of

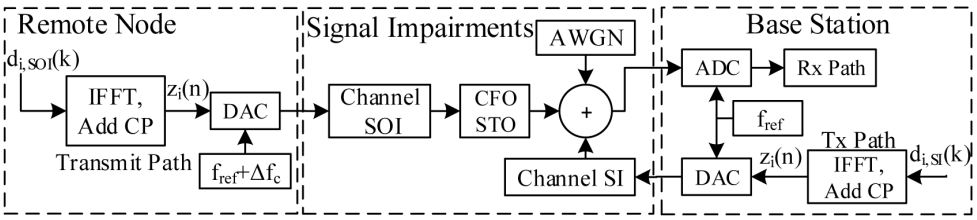

Figure 3.2: OFDM transmit path model with signal impairments.

fixed relative position of self-interference Tx and Rx antennas, h_{si} is modeled to maintain channel continuity from packet to packet. In addition, it assumes the use of passive self interference suppression due to the use of re-configurable directional antenna at the receive port as described in [43]. The SI signal does not experience either CFO or STO because both the transmitter and receiver are co-located at the base station and share the same clock frequency. Finally, AWGN is added to the composite signal containing a superposition of the two signals.

3.3 Channel and Synchronization Effects

Each wireless node generates its own clock signal locally. No matter how accurate two asynchronous clock generators are, the frequency of their oscillations will not be exactly similiar. Clock frequency mismatch causes local oscillator frequency mismatch Δf_c between transmitter's LO and receiver's LO. As a result received signal will experience CFO. The DAC at transmitter and the ADC at the receiver are also driven by asynchronously generated clock signals, thus, after digitization, the received signal samples will experience STO as well. Each signal component in $r(t)$ shown in (3.1) is subject to time and/or frequency offsets with different amounts, since received signal by BS consists of two signal components transmitted by two different transmitters. SOI component in received signal $r(t)$ is transmitted by remote node and thus, it will be impacted by CFO, STO as well as channel delay. SI component in received signal $r(t)$ is transmitted by BS, therefore it will only experience channel delay. To

capture time and frequency misalignments, the received i^{th} block of data $\boldsymbol{r_i}$ can be written as

$$r_i(n) = e^{\frac{j2\pi\varepsilon n}{N_{FFT}}} s_i^{tx}(n-\theta) * h_i^{soi}(n) + y_i^{tx}(n-\tau) * h_i^{si}(n) + w(n) \tag{3.4}$$

where $s^{tx}(t)$ and $y^{tx}(t)$ are SOI and SI components of the transmitted signal. $h^{soi}(n)$ and $h^{si}(n)$ represent path loss and fading of SOI and SI channels respectively. ε is the relative carrier frequency error, defined as $\varepsilon = \Delta f_c/\Delta f$, θ represents time shift of SOI due to STO plus channel delay, and τ represents time shift of SI due to channel delay. Time offset θ is a gradually increasing quantity, which can have integer, as well as, fraction parts $\theta = \theta_{in} + \theta_{fr}$. Offset τ is relatively constant and can be treated as an integer quantity.

3.4 Block Boundary Synchronization Issues

Sampling time offset adds/removes fractional samples to the received signal creating drift in time and causing inter-carrier interference (ICI). Accumulating fractional samples over time result in integer sample shifts creating symbol timing offset, which causes ISI, due to the incorrect placement of the FFT window [30]. In the following, we first consider the effect of STO on the FD system, where $\Delta f_c = 0$ in (3.4). Under this condition (3.4) can be rewritten as

$$r_i(n) = s_i^{tx}(n-\theta) * h_{soi}(n) + y_i^{tx}(n-\tau) * h_{si}(n) + w(n)\ . \tag{3.5}$$

In order to perform digital cancellation of SI and extract data from SOI, it is essential to locate the edges of both signal components and compensate for their offsets.

In general, to locate the edge of a frame, receiver correlates the received signal with locally

stored copy of short training signal and searches for the peak position.

$$\hat{\rho} = \arg\max_{n} \Big[\sum_{m=1}^{W_d} r_i(m) \cdot p^*(m+n) \Big] \tag{3.6}$$

where ρ is detected peak position, W_d is correlation window width and $p(n)$ is the local copy of short training. However, correlation and peak position detection approach alone can easily lead to incorrect results in FD mode, due to the fact that two adjacent short training fields in received signal are subject to different impairments. To analyze the failure of conventional edge detection approach in details, we will look into the following scenarios, that occur frequently in FD mode.

Scenario 1: Overlap of SI and SOI short trainings in received signal. Time drift can shift SOI component in time causing short training field to overlap with SI short training filed in received signal. The overlapping region represents the sum of SOI and SI, which occurs when $\tau - \theta < N_T$.

$$\hat{\rho} = \arg\max_{n} \Big[\sum_{m=1}^{W_d} [s_i^{rx}(n-\theta) + y_i^{rx}(n-\tau)] \cdot p^*(m+n) \Big] \tag{3.7}$$

Correlation with overlapped region has potential of resulting in large false peaks.

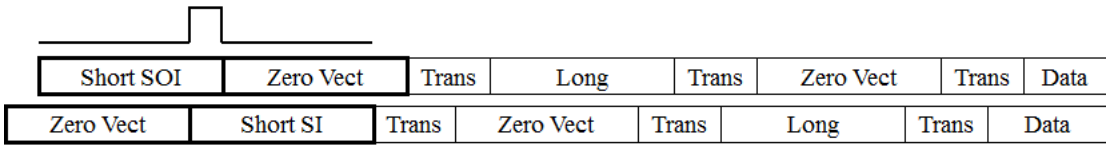

Figure 3.3: Overlap of short training fields in FD OFDM frame.

Scenario 2: Large power difference between SI and SOI components in received signal, in the absence of overlap $\tau - \theta > N_T$. Due to the fact that SI transmit antenna is located very close to Rx antenna, received SI short training power can be much larger than SOI short training power. In that case correlation of received SI with SOI local copy will still result in uncorrelated signal with high enough peaks, located next to SOI short training field. Those

false peaks can mislead peak detection algorithm into detecting wrong edge.

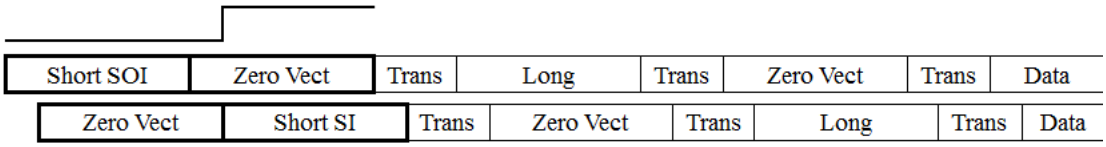

Figure 3.4: FD OFDM frame with large power of SI short training.

Note that inserting zero padded guard interval between short training fields helps with block boundary detection in Scenario 1, but it does not help in Scenario 2. Hence we propose the following technique that combats false correlation peaks in both cases.

3.5 Proposed Synchronization Techique

First, the receiver aims to locate the boundary of SI, which is obvious to locate, due to the fact that SI component experiences a fixed propagation delay without any time drift and has significant power after ADC. To estimate $\hat{\tau}$, receiver cross-correlates the local copy of SI training sequence with received signal $r(n)$, and searches for peak position as described below

$$\hat{\tau} = \arg\max_{n} \left[\sum_{m=1}^{W_d} r(m) \cdot p_{si}^{*}(m+n) \right] \tag{3.8}$$

where $p_{si}(n)$ is the local copy of SI short trainings. Once SI boundary location is found, receiver estimates SI channel $\hat{H}_{si}(k)$, and uses it to perform digital cancellation on SI short training effectively removing it

$$g(n) = r(n) - p_{si}(n-\hat{\tau}) * \hat{h}_{si}(n). \tag{3.9}$$

where $g(n)$ represents a copy of received signal $r(n)$ with SI short training signal removed. Now receiver can safely cross-correlate the local copy of SOI training sequence with the received signal $g(n)$, and search for peak position in order to estimate $\hat{\theta}_{in}$ as described below

Algorithm 1 Robust Block Boundary Detection (RBBD)

1: Detect SI boundary by estimating $\hat{\tau}$
2: Extract SI Long Training use $\hat{\tau}$
3: Estimate SI Channel $\hat{h}_{si}(n)$ use SI Long Training
4: Construct Rx SI short training $\hat{y}_i(n) = p_{si}(n - \hat{\tau}) * \hat{h}_{si}(n)$
5: Subtract $\hat{y}_i(n)$ from received signal$\rightarrow$ $g(n) = r_i(n) - \hat{y}_i(n)$
6: Detect SOI boundary using $g(n)$ by estimating $\hat{\theta}$

$$\hat{\theta}_{in} = \arg\max_{n} \Big[\sum_{m=1}^{W_d} g(m) \cdot p^*_{soi}(m+n) \Big] \tag{3.10}$$

where $p_{soi}(n)$ is the local copy of SOI short training. The correlation window width W_d dictates that the synchronization error must be within a tolerable range. For that reason the receiver must exploit a pilot signal transmitted by the transmitter and readjust transmission start time.

The benefit of the presented technique is twofold. Not only does it introduce robustness in block boundary detection, but also contributes in frequency offset estimation. Since short training is also used for coarse frequency offset estimation, overlapping short training fields in received signal $r(n)$ (Scenario 1) will cause a large CFO estimation error. However, cancellation of SI short training for RBBD purposes results in signal $g(n)$, which has SI free short training field and can be used for coarse frequency offset estimation.

Figure 3.5 illustrates the block diagram of an OFDM receiver supporting IBFD synchronization. The shaded blocks in the figure indicate processing steps that are novel to this architecture as opposed to a standard OFDM receiver. A key difference in this architecture is that block boundary detection of SOI and coarse frequency offset estimation is performed after SI short training removal.

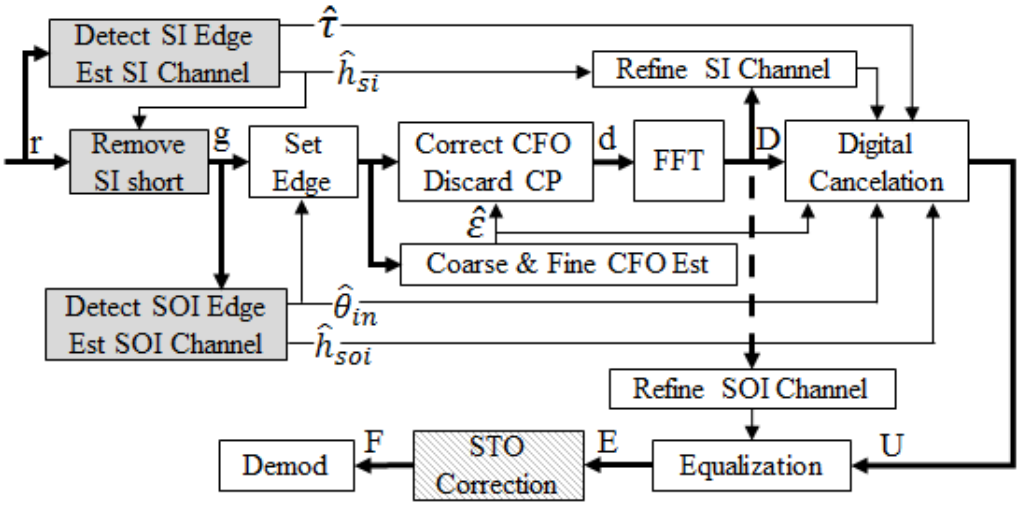

Figure 3.5: OFDM receiver diagram with IBFD synchronization.

3.6 Experimental Results

The proposed technique has been experimentally tested on an FD system with timing and frequency offsets. The experimental FD platform consists of software defined radios (SDR) operating in the topology shown in figure 3.1. All SDRs parameters are set according to signal parameters listed in Table 2.1.

OFDM Parameters	Value	Signal Parameters	Value
Number of OFDM Subcarriers	64	Sim. Channel Type	D
Number of Pilots	4	AWGN Power	-100 dBm
Cyclic Prefix (CP)	$3.2\mu s$	Rx SOI Power	-70 dBm
Symbol Duration (CP+FFT)	$16\mu s$	Carrier Frequency	2.5 GHz
Short Training Duration	$16\mu s$	Signal Bandwidth	5 MHz
Subcarrier Frequency Spacing	78125Hz	Tx Power	5 dBm

Table 3.1: Simulation and Experiment parameters.

Figure 3.6 represents a snapshot of a received frame preamble, where SOI and SI short training parts experience partial overlap corresponding to Scenario 1 in Section 3.4. Figure 3.7 represents a snapshot of a received frame preamble, where SOI and SI short training parts do not overlap, but magnitude of SI is larger then SOI, which corresponds to Scenario

2. Frame boundary detection alone failed to detect corrected frame start position in both cases.

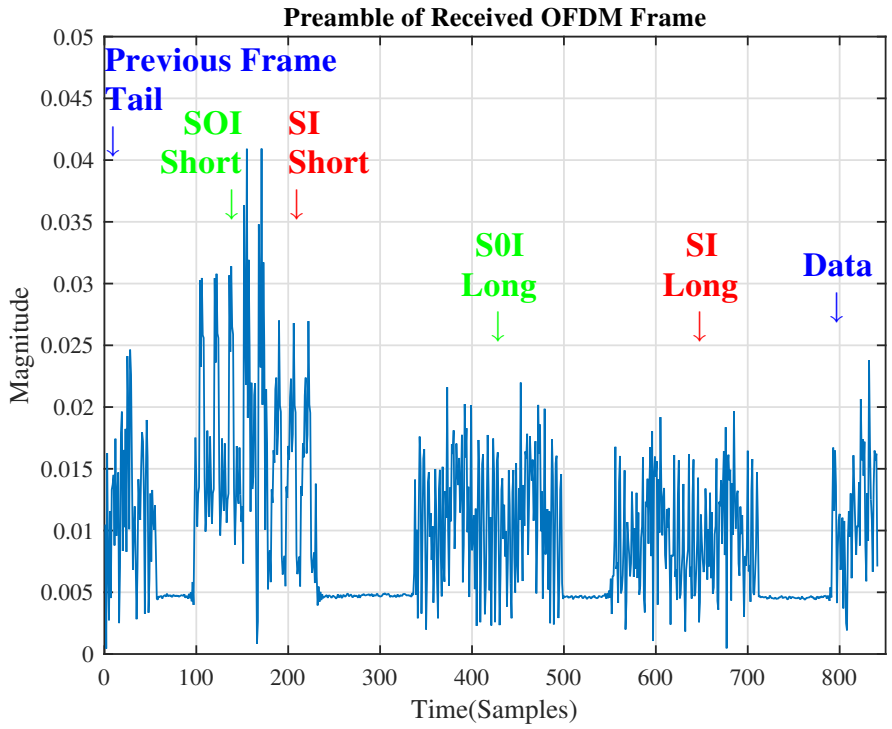

Figure 3.6: Received OFDM frame with partially overlapped SI and SOI short preambles.

The proposed RBBD algorithm manages to suppress SI short preamble down to the noise floor and increases the probability of correct SOI edge detection as well as coarse CFO estimation as shown in Figure 3.8. Note that suppression of SI short preamble depends on the accuracy of SI channel estimate, and does not depend on the the type of occurred scenarios.

3.7 Simulation Results

To further highlight the benefit of RBBD, the FD system in figure 3.1 was simulated for large values of CFO and various SI suppression values. All simulations are performed according

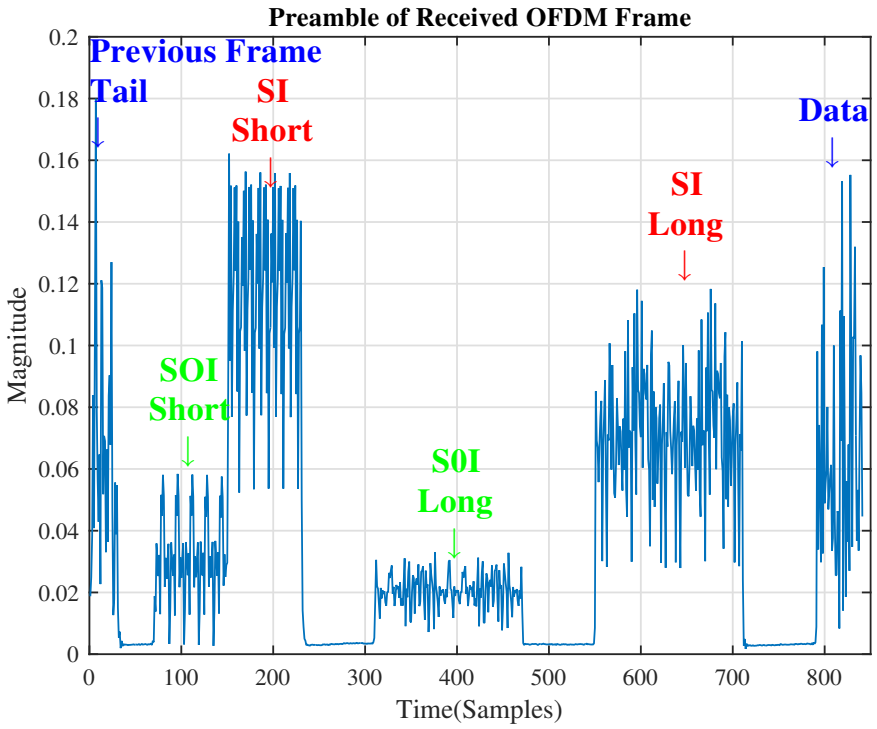

Figure 3.7: Received OFDM frame with SI larger than SOI (Scenario 2).

to the parameters listed in Table 2.1. Overall performance of FD system with and without RBBD is plotted in figures 3.9 and 3.10.

Figure 3.9 illustrates successful frame reception rate as a function of CFO while SI power is kept constant at -75dBm. The large value of cancellation is necessary to show how non-RBBD approaches fail. The figure compares the performance of the system under Scenario 1, since the length of the overlapping interval is proportional to the rate of time drift. From the figure 3.9 it becomes clear that successful frame reception rate of a system without RBBD drops as CFO increases. However when RBBD is applied, the system provides frame success rate of 100% up to CFO of 65ppm. The figure also shows the average system SINR of the received signal at SOI demodulation step.

Figure 3.10 illustrates successful frame reception rate as a function of SI suppression level before ADC, while CFO is kept constant at 1ppm. This corresponds to Scenario 2. From

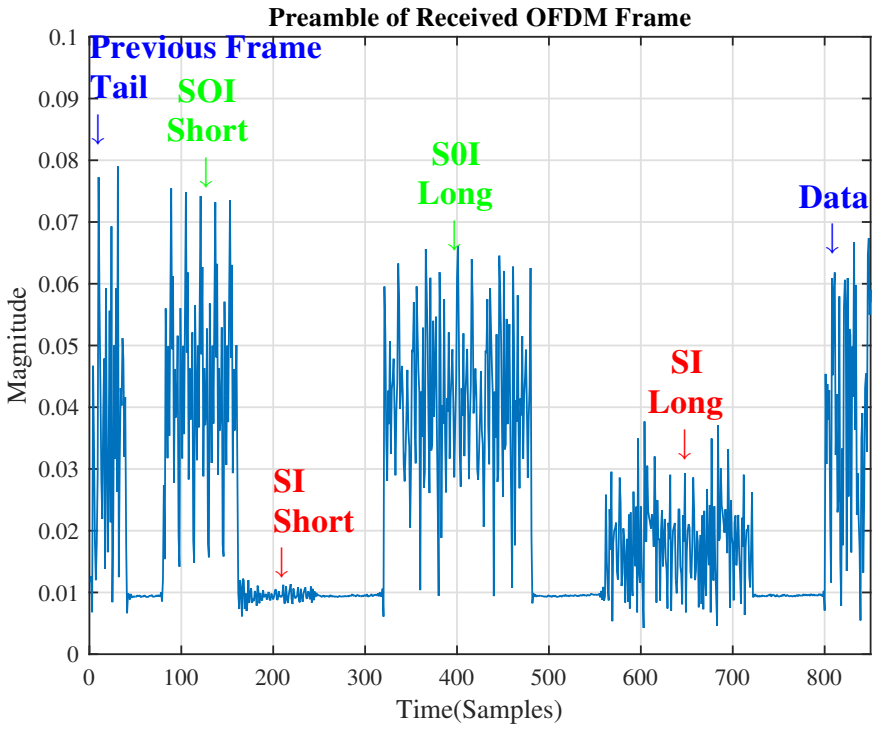

Figure 3.8: Rx OFDM Frame after removal of SI short preamble.

figure 3.10 one can see that the system without RBBD is doing well up to SI suppression of 75dB. This corresponds to the SI power of -70dBm, which equals to SOI power. Increasing SI power more causes block boundary detection errors and a large drop in performance. In case of RBBD the system can withstand large SI levels up to -30dBm and still provide successful frame reception.

3.8 Conclusion

This chapter presents robust block boundary synchronization for in-band full-duplex OFDM system. Detection of frame boundary is one of the initial steps towards successful demodulation of OFDM data. Inaccurate block boundary estimation leads to the loss of the whole data block. Two common failure scenarios are discussed and a novel, robust approach is presented, which boosts synchronization performance and allows operation in severe channel

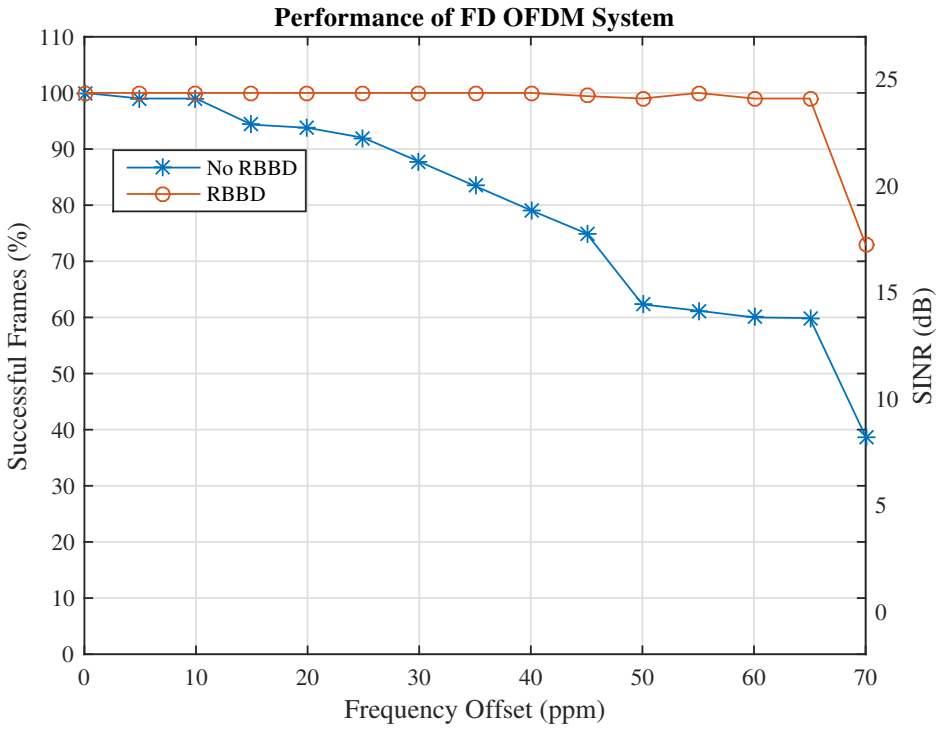

Figure 3.9: Performance of the FD system vs. CFO.

conditions. Simulation and experimental results are presented showing the effectiveness of the proposed technique.

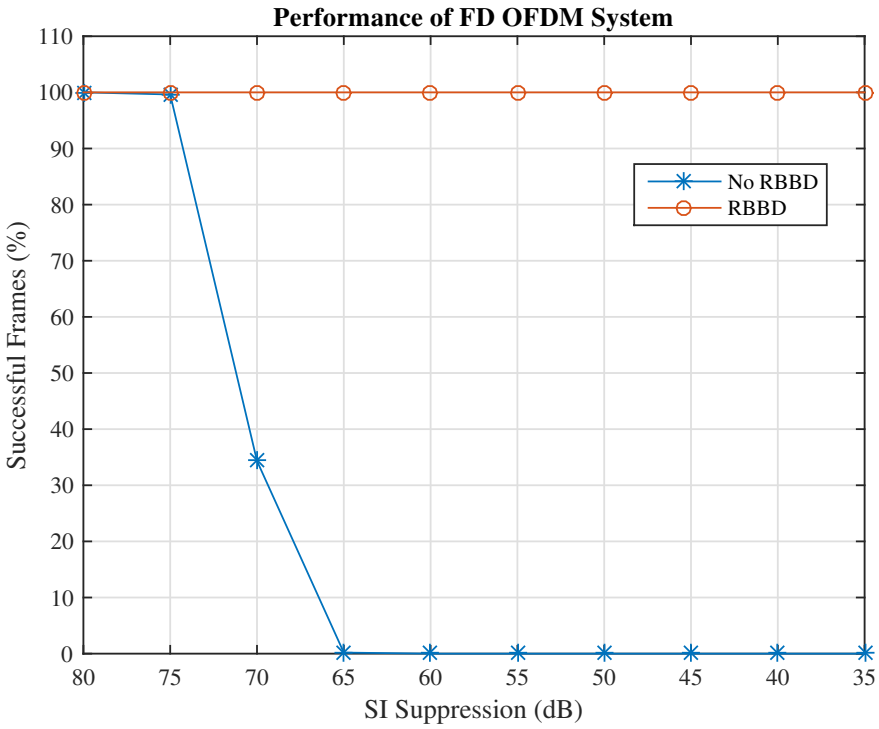

Figure 3.10: Performance of the FD system vs. SI suppression.

Chapter 4

Self-Interference Channel Characterization for Reconfigurable Antenna Based Systems

4.1 Introduction

Traditional radio channels are well understood and characterized with mature channel models when the transmitter and receiver are isolated and separated. However, only few works have investigated the SI channel and its effect on system performance. The authors in [53], consider SI channel propagation characteristics for a two dipole antenna in an indoor environment when operating at 2.6 GHz with 200 MHz bandwidth. The statistical model of path loss factor and Ricean K-factor for different antenna separation was proposed and discussed. Indoor mobile single-input single-output (SISO) SI channel propagation characteristics of a shared single omnidirectional dipole antenna with circulator were investigated in [52]. The measurements indicate that the corresponding SI channel power delay profile (PDP) has

three components: the leakage path, the reflection due to antenna port mismatch, and multipath fading due to surrounding environment. The space multipath component has been modeled by a power-law decay with a log-normal variation. The coherence bandwidth of the SISO SI channel for both the shared and the separate antenna architectures of the IBFD for 3-10 GHz ultra-wideband (UWB) have been studied in [42]. One of the key results is that the coherence bandwidth of the SI channel is found to be varying between 1 and 4 MHz. In [50], the wideband SI channel for outdoor-to-indoor relay was characterized with 300 MHz bandwidth centered at 2.6 GHz. Their measurements indicate that the SI relay channel can be modelled as a single decaying exponential function with specular components, and the small scale fading of each tap was modeled by Rician distribution. The authors in [17] present a measurement based study of the capabilities and limitations of three key mechanisms for passive self-interference suppression: directional isolation, absorptive shielding, and cross polarization. The study demonstrates that more than 70 dB of passive suppression can be achieved in certain environments. They found that environmental reflections limit cancellation performance where passive SI suppression can be achieved. In addition, higher passive SI suppression generally results in serious frequency selectivity of the SI channel.

In this chapter, we perform channel characterization of self-interference IBFD-OFDM systems that use beam steering, multi-reconfigurable antenna (MRA) as a passive SI suppression mechanism. Specifically, this chapter presents the following contributions:

- Measurements of SI channel are presented that are collected using IBFD-OFDM software-defined radio (SDR) platform under scenarios of high and low suppression levels provided by MRA, static/dynamic environments and system bandwidth of 5MHz, 10MHz 20MHz.
- Comparison between measured channel delay profiles along with frequency responses is presented highlighting the significant differences and their impact on complexity of SI suppression mechanisms.

- Statistical modeling of SI channel is performed by fitting probability distribution to the collected data and comparing the results by conducting goodness of fit test.

The remainder of the chapter is organized as follows. In Section 4.2, MRA based IBFD system is described and the received level of SI along with its impact on system performance depending on selected MRA pattern are presented. In Section 4.3, experimental setup for SI channel measurements is described. SI channel measurements under different scenarios are presented and compared in Section 4.4. Channel characterization based on statistical modeling is presented in Section 4.5. The chapter is concluded in Section 4.6.

4.2 Full Duplex System

A wireless system operating in full-duplex mode is illustrated in figure 4.1. The system consists of base station receiving from a remote node N2, at the same time transmitting to another node in the same frequency band. Signals transmitted by the remote node to the base station are referred to as signal of interest (SOI), and the transmitted signal by the base station causes SI. All the nodes employ Orthogonal Frequency Division Multiplexing (OFDM) with N_{FFT} subcarriers, therefore the i^{th} block of received signal by the base station in the frequency domain can be modeled as

$$R_i(k) = S_i^{tx}(k)H_i^{soi}(k) + Y_i^{tx}(k)H_i^{si}(k) + W_i(k) \tag{4.1}$$

where $S^{tx}(k)$ and $Y^{tx}(k)$ are SOI and SI components of the transmitted signal. $H_i^{soi}(k)$ and $H_i^{si}(k)$ are channels frequency responses of SOI and SI respectively. $W(k)$ is Additive White Gaussian Noise (AWGN).

From Eq. (4.1) it is clear that SI must be suppressed in order to achieve satisfactory Signal to Interference and Noise Ratio (SINR) for the received signal. Multiple techniques for sup-

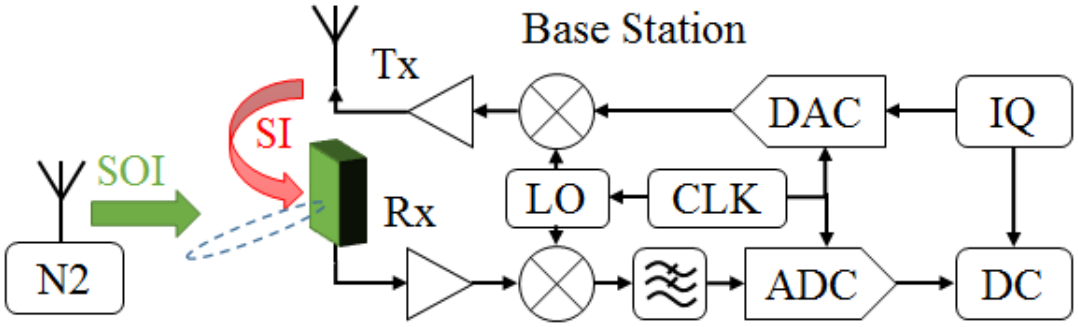

Figure 4.1: Block diagram of full duplex node.

pressing SI exist across multiple domains such as propagation, analog and digital. The base station is equipped with a multi-reconfigurable antenna (MRA), which provides significant passive suppression of self-interference in the propagation domain, meanwhile preventing saturation of Rx font-end. It is a single antenna element, equipped with rectangular patch segments, that can either be connected together with low loss switches or can be left floating. This causes the antenna geometry to change consequently changing its radiation pattern dynamically. Figure 4.2b shows a 3D shape of a selected radiation pattern, and Figure 4.2a illustrates 2D radiation patterns for different switch combinations, plotted on top of each other to highlight their differences. Aiming for maximum passive SI suppression, the search algorithm selects the radiation pattern that achieves the weakest $H^{si}(k)$.

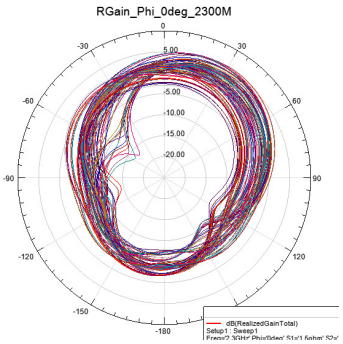

(a) 2D Radiation Pattern

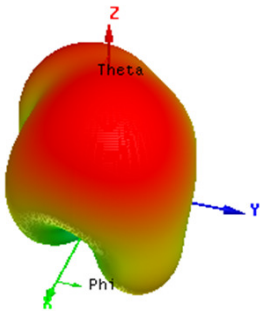

(b) 3D Radiation Pattern

Figure 4.2: MRA Radiation Pattern

To achieve active SI suppression, digital cancellation is used as a second stage after MRA. At this step the receiver uses the knowledge of a local copy of the transmitted signal to

perform subtraction from the received signal, which contains the superposition of SOI and SI. While subtracting a known signal (SI known transmit signal) seems straightforward, numerous analog components in the Tx chain distort the signal both linearly and non-linearly, complicating the cancellation process. Furthermore, noise mechanisms associated with the phase locked loop and receiver components further complicate the problem. Therefore naively subtracting the baseband signal from the received signal without accounting for all the distortions results in limited cancellation performance. Assuming perfect synchronization between the nodes the received signal after digital cancellation can be expressed as

$$D_i(k) = S_i^{tx}(k)H_i^{soi}(k) + Y_i^{tx}(k)(H_i^{si}(k) - \hat{H}_i^{si}(k)) + W_i(k) \tag{4.2}$$

where $\hat{H}^{si}(k)$ is the estimated SI channel at digital cancellation step. In this work, least square (LS) estimation method is used for estimating SI channel at the receiving node.

$$\hat{H}_i^{si}(k) = \frac{P_i^{si}(k)}{Y_i^{tx}(k)} = \frac{Y_i^{tx}(k)H_i^{si}(k) + W_i(k)}{Y_i^{tx}(k)}, \tag{4.3}$$

where $P_i^{si}(k)$ is the local copy of i^{th} block of SI preamble. From (4.2) it is obvious that the interference term diminishes as the difference between the actual and estimated SI channels decreases. Considering finite accuracy of SI channel estimation, the received signal after digital cancellation can be expressed as

$$D_i(k) = S_i^{tx}(k)H_i^{soi}(k) + W_i^{si}(k) + W_i(k) \tag{4.4}$$

where $W^{si}(k)$ is the residual uncompensated self-interference, and is due to SI channel estimation error [43].

4.3 Experimental System Setup

A complete full-duplex experimental system is constructed using the Universal Software Radio Peripheral (USRP) SDR platform. Each USRP contains a Radio Frequency (RF) transceiver and a Field Programmable Gate Array (FPGA). All USRPs are connected to a host PC through a Gigabit Ethernet connection. The baseband signal processing is performed over the host PC. The baseband signals are streamed to/from the USRPs at a rate of 25M sample/sec. The RF transceivers are then used for real time signal transmission and reception.

As shown in Figure 4.3, the base Station is equipped with one transmit and one receive antenna situated 10cm apart from each other. Node 2 uses only one antenna. A monopole omni-directional antenna is used as transmit antenna, while a reconfigurable directional antenna is used as a receive antenna. Both transmit and receive antennas have the same antenna polarization. The reconfigurable antenna has a total of 4096 different possible radiation patterns. A successful pattern, is a pattern that maximizes the SOI signal and minimizes the SI signal. The pattern selection is performed through a 12-line digital control cable driven from an FPGA on a Zedboard. The timing of all USRPs and the FPGA that drive the antenna radiation selection are aligned with one reference Pulse Per Second (PPS) signal. All the signals are transmitted according to parameters listed in Table 4.1.

OFDM Parameters	**Value**	**Signal Parameters**	**Value**
Number of OFDM Subcarriers	64	Carrier Frequency	2.5 GHz
Number of Data Subcarriers	44	Sampling Rate	5-20 MHz
Cyclic Prefix (CP)	$3.2\mu s$	Tx Power	10dBm
Symbol Duration (CP+FFT)	$16\mu s$	Rx SOI Power	-65 dBm
Long Training Duration	$32\mu s$	Rx SI Power SP	-60 dBm
Short Training Duration	$16\mu s$	Rx SI Power NSP	-25 dBm

Table 4.1: Experimental system parameters

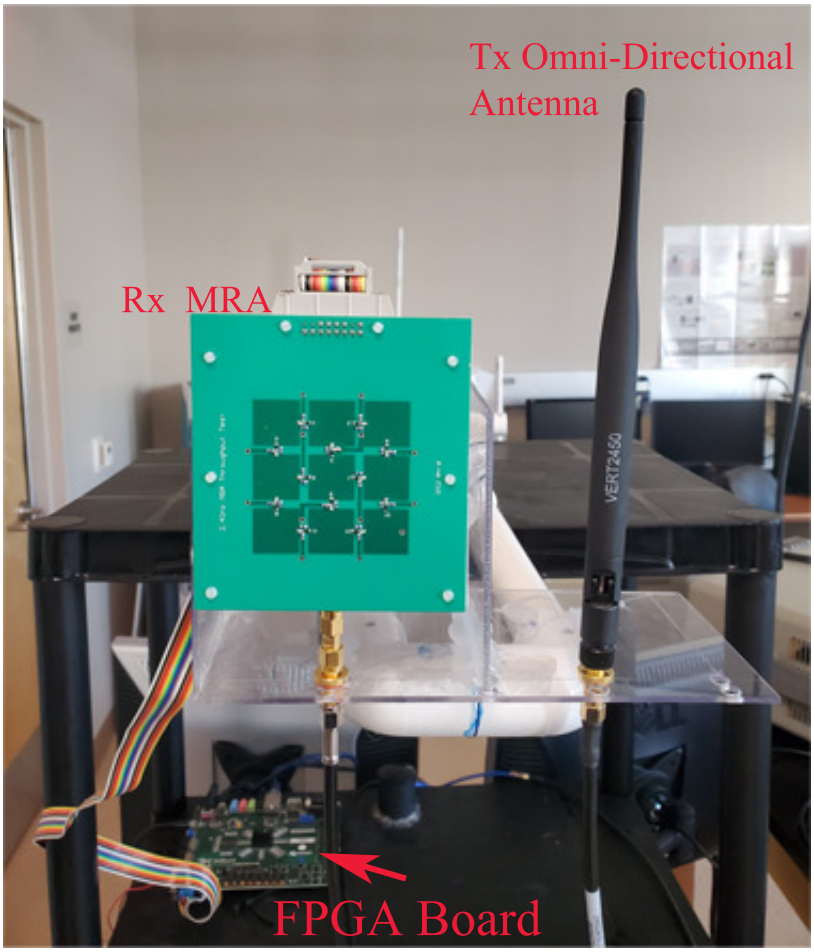

Figure 4.3: Tx and Rx antenna setup on FD base station

4.4 Channel Measurements and Comparison

To capture the SI channel characteristics depending on selected MRA pattern, the received signal i probed in the digital domain (after ADC) before the digital cancellation step shown in Figure 4.1. Since the MRA has 4096 different patterns, each selected pattern can be viewed as a unique channel. To simplify the study we examine the SI channel when a suppressing pattern (SP) is selected, providing SI suppression of at least 60dB, and a non-suppressing pattern (NSP) is selected, in which case SI suppression is only 20dB due to antenna separation. The channel measurements are performed by sending a test signal and measuring the channel response at the receiver. To capture the SI channel effects on narrow-band and wide-

band operations, the channel measurement are acquired using a system bandwidth of 5MHz, 10MHz and 20MHz. The test signal is generated using continues transmission of consecutive packets, where each packet is constructed according to a modified WiFi frame structure with non-overlapping training preamble enabling the receiver to estimate the channels of individual signal components of SI and SOI in FD mode [45].

4.4.1 NSP Channel Measurements

SI channel measurements were collected in the lab during static and dynamic environments. Channel dynamics were introduced by manually moving a reflector object with $1m^2$ flat surface area approximately $2m$ away from the base station. Figure 4.4 illustrates the power delay profile of SI channel under the scenario when a non-suppressing pattern is selected by MRA. From the figure, it is clear that due to the low suppression of SI there exist one strong channel path that dominates regardless of the transmitted signal bandwidth and existence of surrounding reflecting objects. The channel power delay profile was not affected by the introduced dynamics due to the presence of strong SI signal transmitted from a source 10cm away, which is orders of magnitude larger than the reflections from object located 2m away.

4.4.2 SP Channel Measurements

In the case when a suppressing pattern is selected by MRA, an additional SI suppression of 35dB is observed, which weakens the direct sight of SI channel, effectively making the SI reflections from indirect sight significant. Figure 4.5 illustrates the SI channel delay profile when SP is selected in static environment. Due to the minimal changes in environment, the power variations of the channel taps are minimal. As a result the channel taps with dominant powers do not experience much variation throughout the experiment. For narrowband system, the SI channel can be approximated as having one dominant tap, whereas for

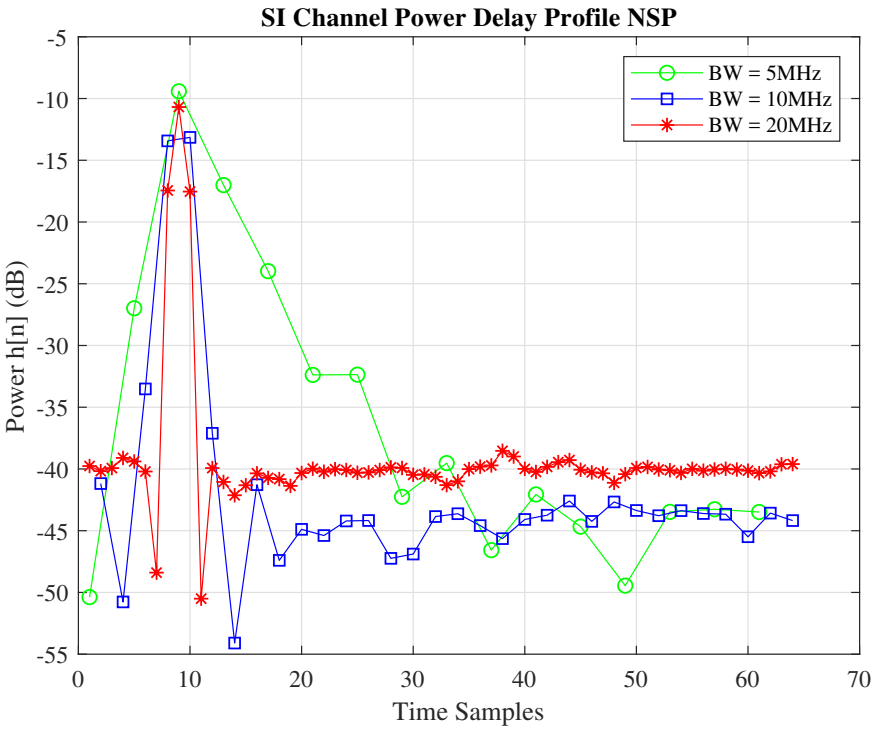

Figure 4.4: SI channel delay profile in *static and dynamic* environments.

larger bandwidth, such as 10MHz and 20MHz multi-path components come into the picture. The presence of significant multi-path creates additional channel taps and consequently frequency selectivity, which can be seen in the channel frequency response plotted in Figure 4.6.

Figure 4.7 illustrates the SI channel power delay profile in a dynamic environment. In this case, due to the moving reflecting object, even the dominant SI channel taps are experiencing large power level variations over time. As opposed to the NSP case, the introduced environment dynamics become more significant with larger SI suppression. Comparing channel delay profiles of static and dynamic environments (Figure 4.7 and Figure 4.5), it is obvious that dynamic SI channel has larger delay spread, introducing frequency selectivity even for narrow-band transmission. By comparing the estimated frequency response of static and dynamic channels (Figure 4.6 and Figure 4.8), it is obvious that frequency selectivity in dynamic channel is noticeably increased for all three bandwidths.

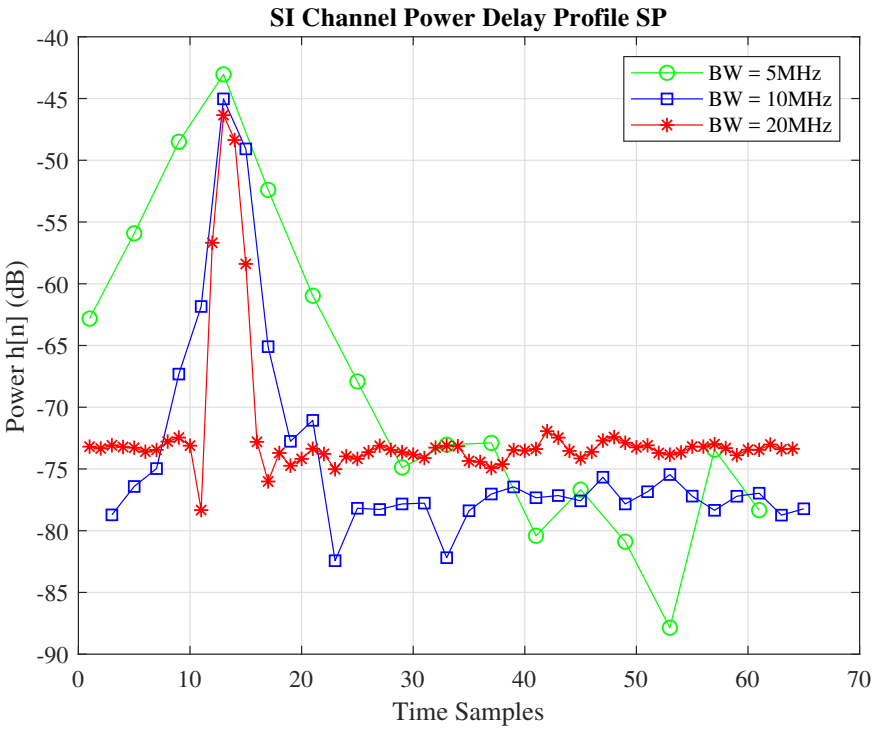

Figure 4.5: SI channel delay profile in *static* environment.

4.4.3 Discussion

The SI channel characteristics directly impact the SI suppression capability and the complexity of suppressing mechanisms. Initially SI suppression is small, and there is a single dominant SI path, while multi-path are insignificant (Figure 4.4). As the dominant path is being suppressed, some reflections become significant requiring additional suppression stages especially for wide-band transmission (Figure 4.5). In addition, if a dynamic environment is introduced, then suppression of SI becomes even more challenging with increased delay spread and varying power levels of channel delay taps as shown in Figure 4.7.

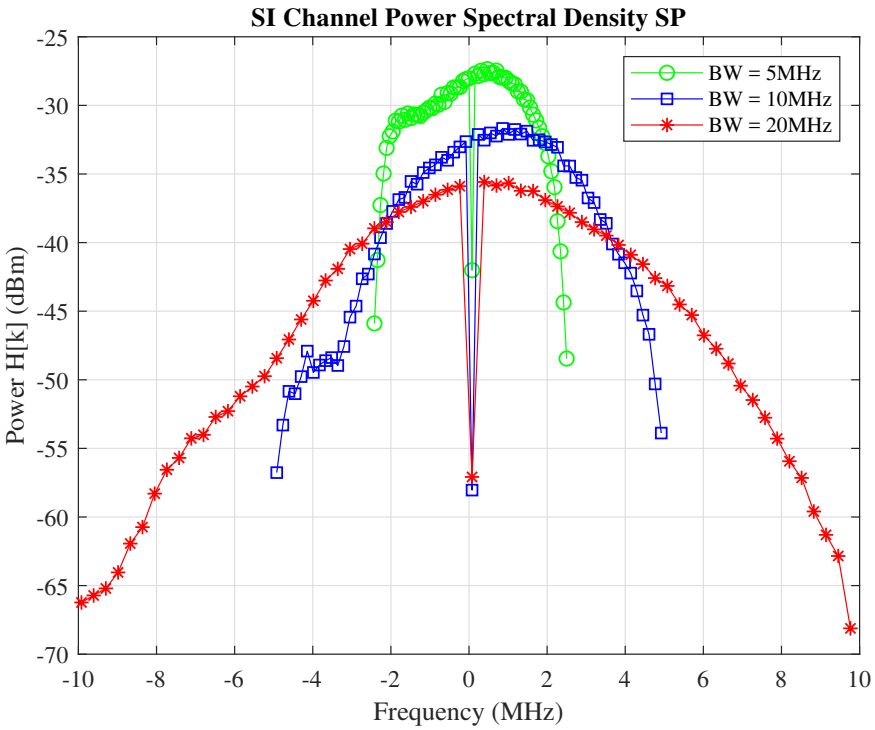

Figure 4.6: SI channel frequency profile in *static* environment.

4.5 SI Channel Characterization

The channel model illustrated in Figure 4.1 represents both SOI and SI channels. SOI channel can be modeled as Rayleigh fading channel, considering the absence of Line-Of-Sight (LOS) component due to the location of Node2 [24].

In order to properly choose a realistic model for SI channel, we conducted a brief statistical study of the SI channel for the scenarios when SP and NSP are selected by MRA. For each of the two patterns, over 5000 SI channel measurements are collected. We then performed fitting of Rayleigh and Rician probability density functions (PDF) into collected data, using maximum likelihood estimation (MLE) of parameters [5]. To conduct a fair comparison between the candidate models we have used two parameter Rayleigh distribution, where an additional parameter defines the location of the Probability Density Function (PDF) [14].

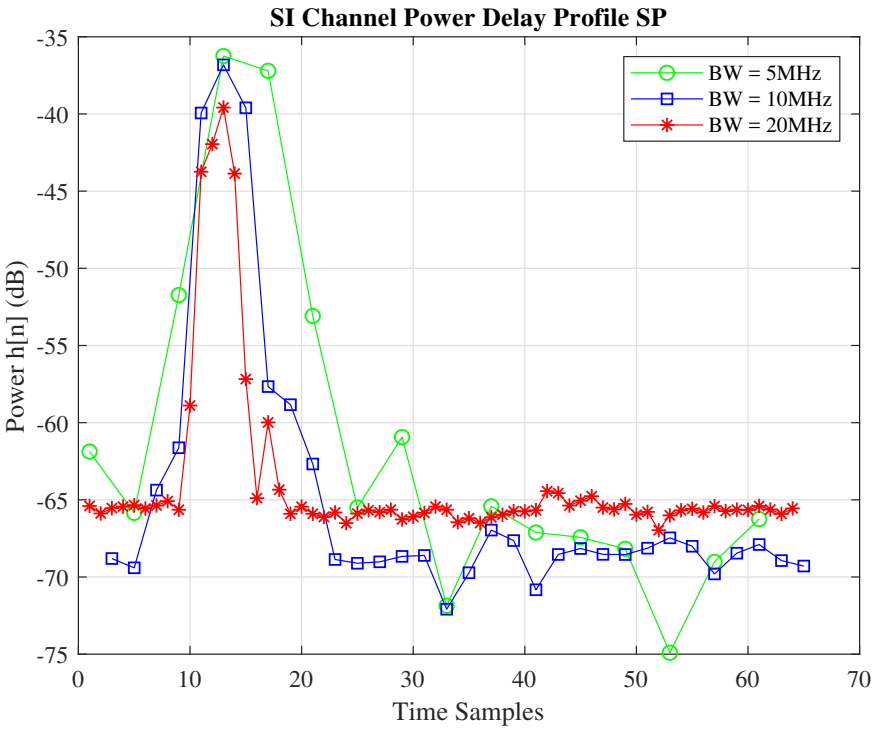

Figure 4.7: SI channel delay profile in *dynamic* environment.

Figure 4.9 illustrates channel distribution of SI when NSP is selected, overlapped with candidate PDFs. To quantify the goodness of model fit to statistical data, we calculated the Akaike information criterion (AIC), as well as the Bayesian information criterion (BIC) values and tabulated thye results in Table 4.2. The model with the lowest AIC and BIC is preferred. When NSP is selected, the presence of a strong LOS component centers the distribution away from the origin and keeps it symmetrical in shape. As a result Rician PDF is better fit demonstrating low AIC and BIC (Table 4.2). Rician K-factor is defined as the ratio of signal power in dominant component over the scattered power. For this particular channel, it is estimated to be 24.65dB, which is another indication of a strong LOS for SI. In the case of SP, there is a significant suppression of SI resulting in skewness and shift towards the origin (Figure 4.10), where Rayleigh distribution begins to be a better fit as shown in Table 4.2. Rician K-factor in this case is estimated to be -32dB indicating weak LOS and tendency toward Rayleigh distribution.

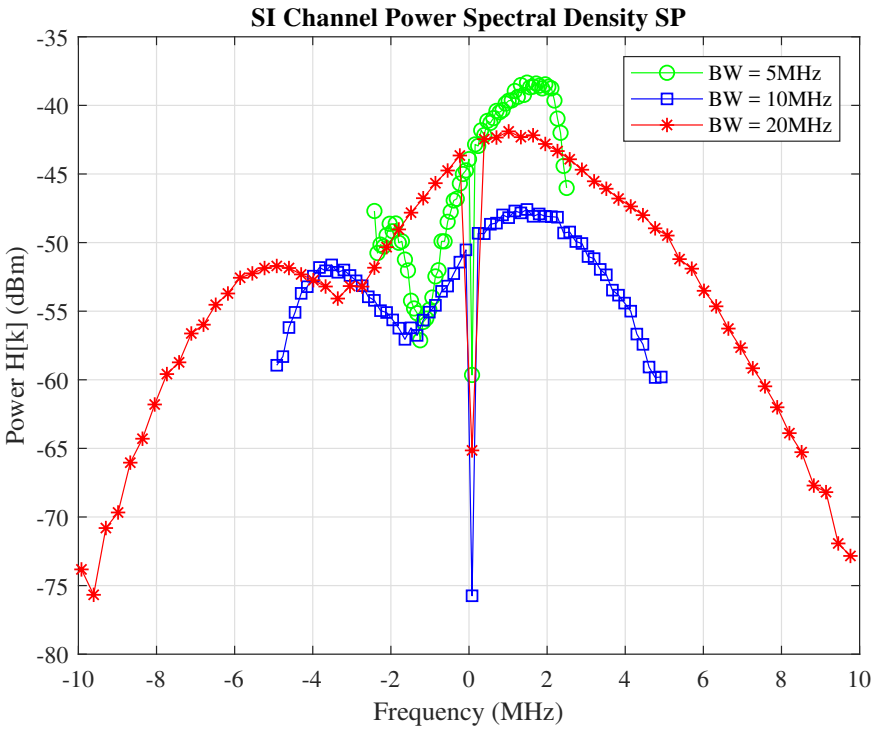

Figure 4.8: SI channel frequency profile in *dynamic* environment.

Distribution	AIC for NSP	BIC for NSP	AIC for SP	BIC for SP
Rayleigh	-43939	-43922	-36852	-36839
Rician	-61358	-61342	-35890	-35879

Table 4.2: AIC and BIC values indicating goodness of fit.

4.6 Conclusion

This chapter presented self-interference channel characterization for MRA based OFDM full-duplex systems. The goal of SI channel measurements is to demonstrate the channel behaviour depending on the achieved suppression levels, system bandwidths and environment dynamics. Comparison of collected SI channel measurements in above mentioned scenarios is performed and significant changes are highlighted. Finally SI channel is statistical modeled by fitting probability distributions to collected channel data and results are compared using goodness of fit test.

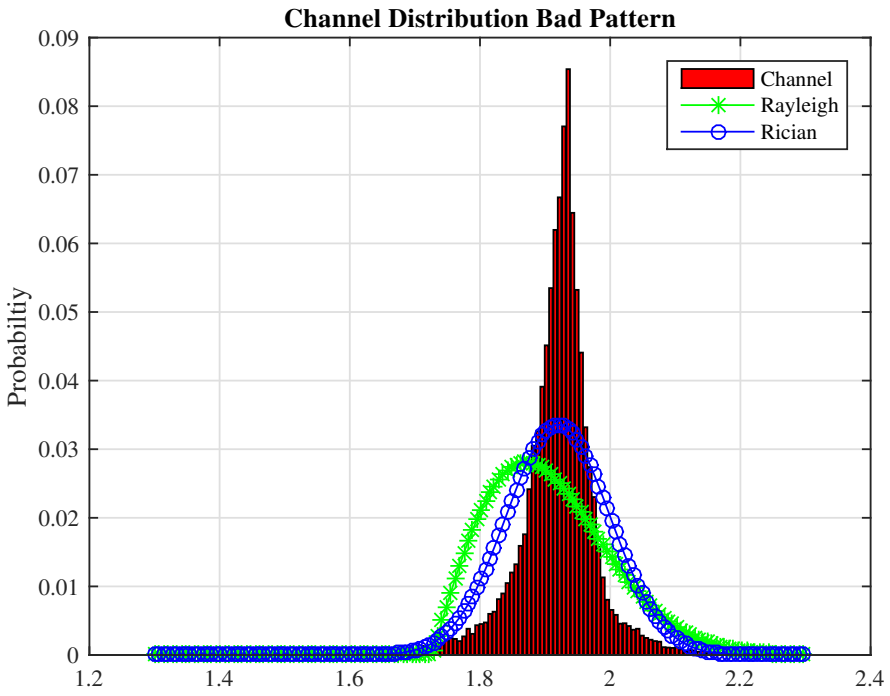

Figure 4.9: Channel PDF when NSP is selected.

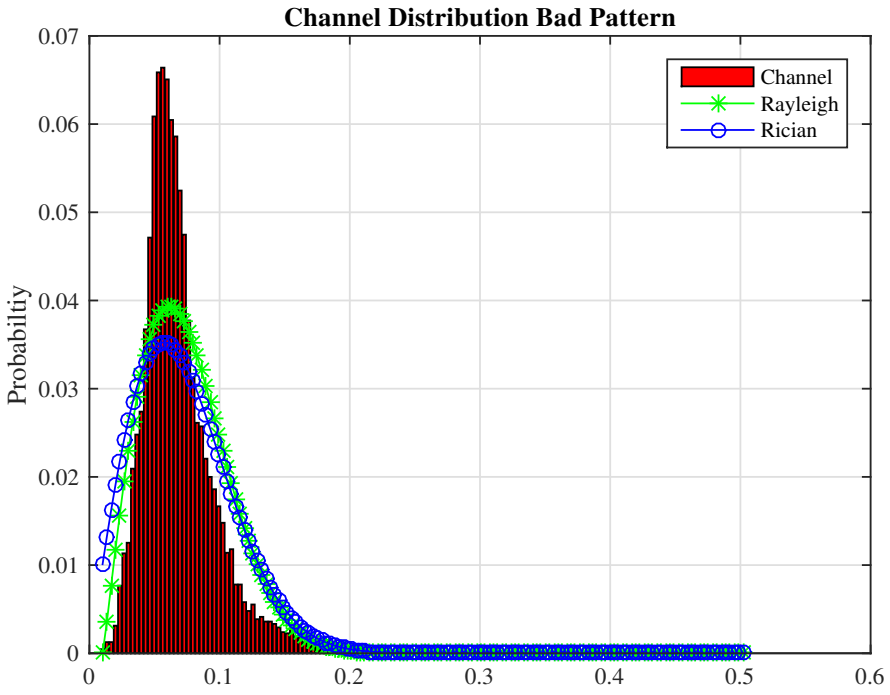

Figure 4.10: Channel PDF when SP is selected.

Chapter 5

Active Cancellation of Self-Interference for Full-Duplex Wi-Fi Relay

5.1 Introduction

Addition of relay station (RS) to an existing Wi-Fi network is a common solution when wireless coverage extension is required in the absence of a connection to the backbone network. Half-duplex (HD) Wi-Fi relays employ two different frequencies, time slots, or orthogonal spreading codes to prevent the transmitted signal from interfering with its own receiver. In contrast full-duplex relays (FDR) utilize wireless resources more efficiently by transmitting and receiving simultaneously on the same frequency band, creating the potential of doubling the system throughput, when compared to their Half Duplex (HD) counterparts [43]. Although FDR has higher transmission efficiency, it suffers from Self Interference (SI) since the transmitted signal by the FDR is received as an in-band blocker by its own receiver. The SI

signal results in system instability, and poor signal to interference plus noise ratio (SINR) of the signal that is intended to be relayed [55]. In order to use a FDR for higher efficiency, SI must be coherently canceled in order to provide stability and a satisfactory level of SINR of the received signal, before amplifying and forwarding it. To achieve sufficient SI suppression FDR relies on cancellation across multiple domains (spatial, analog and digital cancellation).

Numerous techniques are available for SI suppression including passive (eg. antenna separation, directional antennas etc.) and active (analog and digital) cancellation [51]. Active cancellation (AC) is based on the knowledge of the SI channel state information and its boundary in time. To estimate channels under severe timing and frequency offsets, a customized frame structure of alternating pilots has been proposed [11]. However, changing the current standards to accommodate FDRs is either unlikely or will delay the adoption of FDR systems. Thus, in order to benefit from FDR, it is necessary to find means to perform SI cancellation while remaining standard compliant.

In this chapter Amplify and Forward Relay (AFR) station is considered. We identify and analyze impairments due to wireless channel effect and synchronization errors on the received signal by AFR. Techniques are developed enabling AFR to perform channel estimation, synchronization error estimation and compensation, while maintaining compliance with Wi-Fi packet structure. Specifically, this chapter presents the following contributions:

- A novel estimation strategy of SI channel and time delay is presented that makes use of existing procedures in Wi-Fi protocol, and avoids any software/hardware modifications of the other network nodes.
- A collision detection technique is presented, allowing validation of acquired channel estimate based on none-acknowledgeable packets in random access networks.
- Performance of the system in the presence of dynamic channel effects and synchronization errors is evaluated.

The remainder of the chapter is organized as follows. In Section II a Wi-Fi network extended by FDR is described and challenges are outlined. In Section III time and frequency misalignments are described and their impacts on SI cancellation are highlighted. In Section IV, SI channel estimation and time alignment techniques are proposed. Performance results of the simulated system under different channel conditions is presented and compared in V. The chapter is concluded in Section VI.

5.2 System Model

Figure 5.1 illustrates a Wi-Fi network consisting of an access point (AP) and stations (ST). Some stations are located outside the coverage of AP and do not receive service, e.g ST2. For simplicity we will assume that the transmitted signal strength by AP is negligible outside of the AP's radio coverage area. To extend the coverage, a FDR station is placed at the boundary of the AP cell. All the stations including FDR and AP utilize Orthogonal Frequency Division Multiplexing (OFDM), that employs N_{FFT} subcarriers with inter-carrier spacing $\Delta f = f_s/N_{FFT} = 1/(N_{FFT}T_s) = 1/T_{sym}$, where T_s is sampling period, f_s is sampling frequency and T_{sym} is one OFDM symbol duration.

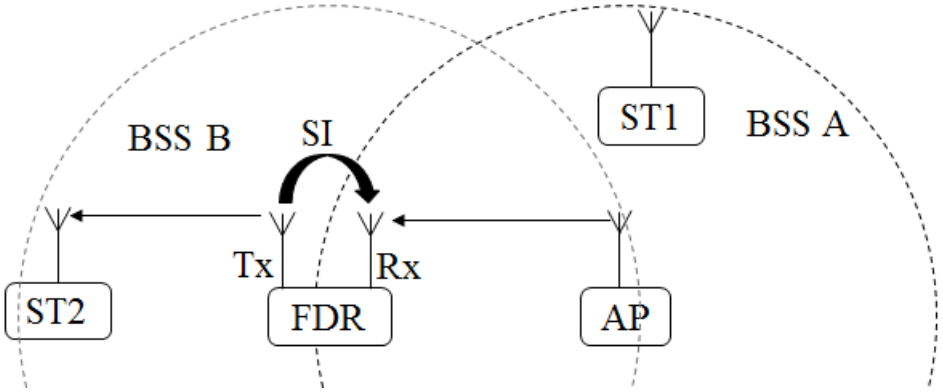

Figure 5.1: Diagram of full duplex relayed Wi-Fi Network.

5.2.1 Relay Station

The relay station is classified to be Amplify and Forward (AF) type, however it is assumed to have the ability to construct and transmit certain control/management packets defined in the Wi-Fi standard. The relay station receives and transmits Wi-Fi packets on the same frequency and in the same time slot. The signal that FDR is aiming to receive is the signal of interest (SOI). The transmitted signal by FDR is also received by its own receiver, causing SI, thus the received signal by the FDR station can be modeled as

$$r(t) = s^{rx}(t) + y^{rx}(t) + w(t) \tag{5.1}$$

where $s^{rx}(t)$ and $y^{rx}(t)$ are SOI and SI components of the received signal and $w(t)$ is Additive White Gaussian Noise (AWGN).

In general, SI power is orders of magnitude larger than SOI, due to the fact that the distance between Tx and Rx antennas of the FDR is significantly smaller compared to the distance between any transmitting node and the FDR. In order to successfully receive SOI and re-transmit it with high gain, while maintaining stability, a proper isolation between Tx and Rx chains of the FDR is required [32], to avoid positive feedback. This is difficult to achieve only with passive SI suppression. Active suppression relies on the accurate knowledge of the SI component in the received signal. Hence we will detail the channel and timing misalignment impact on AC at FDR, in Section III.

5.2.2 Channel Model

SOI channel, h^{soi}, is modeled to reflect path loss and Rayleigh fading effects. Since received packets are transmitted by nodes, randomly located in the cell, h^{soi} is modeled to reflect random discontinuity of SOI channel from packet to packet. SOI is impacted by carrier

frequency offset and sampling time offset due to the local oscillator (LO) mismatch Δf_c.

The SI channel, h_{si}, is modeled to reflect path loss and Rayleigh fading effects. There are three main consideration to make regarding SI channel as follows:

1. Due to the fixed relative position of SI Tx and Rx antennas, h_{si} is modeled to maintain channel continuity from packet to packet.

2. It is assumed that a passive SI suppression of 60 dB is achieved by using reconfigurable directional antennas as previously described by the authors in [43]. Using reconfigurable directional antennas, effectively cancels the line of sight SI component and results in a Rayleigh channel observed for the SI channel rather than a high K Ricean channel.

3. The SI signal does not experience either Clock Frequency Offset (CFO) or Sampling Time Offset (STO) because both the transmitter and receiver are co-located at the FDR and share the same clock frequency.

Finally, AWGN is added to the composite signal consisting of SOI and SI.

5.3 Channel and Misalignment Effects on FDR

Each wireless node generates its clock signal locally. Clock frequency mismatches result in a frequency mismatch Δf_c between the transmitter LO and the receiver LO. As a result, the received signal will experience CFO. The Digital to Analog Converter (DAC) at the transmitter and the Analog to Digital Converter (ADC) at the receiver are also driven by asynchronously generated clock signals, thus, after digitization, the received signal samples will experience STO as well. Each signal component in $r(t)$ as shown in (5.1) is subject

to time and/or frequency offsets with different amounts, since the received signal by FDR consists of two signal components transmitted by two different transmitters. SOI component in the received signal $r(t)$ is transmitted by the remote node thus, it will be impacted by CFO, and STO as well as channel delay. SI component in received signal $r(t)$ is transmitted by FDR, therefore it will only experience channel delay. To capture time and frequency misalignments, the received i^{th} block of data $\boldsymbol{u_i}$ by FDR can be written as

$$u_i(n) = e^{j\frac{2\pi\varepsilon n}{N_{FFT}}} s_i^{tx}(n-\theta) * h_i^{soi}(n) + y_i^{tx}(n-\tau) * h_i^{si}(n) + w(n), \tag{5.2}$$

where $s^{tx}(t)$ and $y^{tx}(t)$ are SOI and SI components of the transmitted signal. $h^{soi}(n)$ and $h^{si}(n)$ represent path loss and fading of SOI and SI channels respectively. ε is the relative carrier frequency error, defined as $\varepsilon = \Delta f_c/\Delta f$, θ represents time shift of SOI due to STO plus channel delay, and τ represents time shift of SI due to channel delay. Time offset θ is a gradually increasing quantity, which can have integer, as well as, fraction parts $\theta = \theta_{in} + \theta_{fr}$. Offset τ is relatively constant and can be treated as integer quantity.

5.3.1 Amplify And Forward Full-Duplex Relay

In AF mode, FDR is transparently relaying every packet without decoding its content. This strategy relaxes MAC requirements at the expense of allowing unnecessary re-transmissions. Recall that AC relies on subtraction of known transmitted SI from the signal being received. After Digital Cancellation (DC), i^{th} block of the received signal $\boldsymbol{d_i}$ can be expressed as

$$d_i(n) = u_i(n) - y_i^{tx}(n-\hat{\tau}) * \hat{h}_i^{si}(n) = e^{j\frac{2\pi\varepsilon n}{N_{FFT}}} s_i^{tx}(n-\theta) * h_i^{soi}(n) + w_i^{si}(n) + w(n), \tag{5.3}$$

where $\hat{\tau}$ is the estimated time offset of SI component and $\hat{h}^{si}(n)$ is SI channel estimate. $w^{si}(n)$ is the residual SI after DC. Analog cancellation takes the same approach but operations are carried out in analog domain before the receiver ADC. From (5.3) it is obvious that even

when FDR does not decode SOI, it still has to estimate SI channel and its delay, in order to minimize residual SI $w^{si}(n)$, before amplifying and re-transmitting $\boldsymbol{d_i}$.

5.3.2 Decode And Forward Full-Duplex Relay

In DF mode, FDR appears as a station to the AP and serves ST2 as AP. DFR decodes incoming packet and makes a decision whether the packet needs to be relayed. This strategy of relaying allows selective relaying of wireless packets, avoiding unnecessary re-transmissions and possible congestion of neighboring networks. On the other hand, DF-FDR has to be able to successfully decode at least Medium Access Control (MAC) field of the received Wi-Fi packet, requiring full compensation of synchronization errors as well as SI suppression below noise floor. Hence DFR has to perform SI suppression as shown in (4), followed by compensation of θ, ε and $\boldsymbol{h_i^{soi}}$.

5.4 Proposed SI Channel Estimation and Alignment

As described earlier AF-FDR requires time offset detection of SI component as well as SI channel estimate. During relaying, it receives two overlapping packets, where overlap corrupts both training and data fields, as shown in figure 5.2. Since all transmitted packets must comply with Wi-Fi standard, FDR cannot use a customized packet structure, which could avoid overlap of training fields during re-transmission.

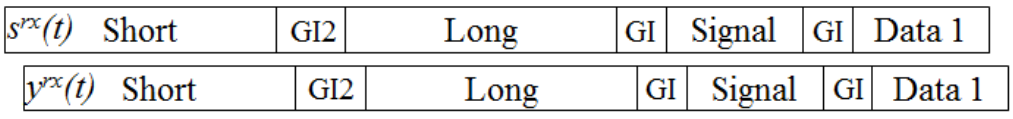

Figure 5.2: Received Signal by FDR in Wi-Fi Traffic.

5.4.1 Proposed AF-FDR solution:

In this work, we propose that the FDR transmits control/management frames periodically to train and update the SI channel estimate accordingly using transmit Clear-To-Send (CTS) frame to itself, which is an already defined technique in Wi-Fi. CTS-to-self is a method of reserving medium for upcoming data transmission, for a specified duration [23]. Since FDR only needs to perform training during CTS-to-self, and has no intention of reserving the channel, it will set Duration field to be 0.

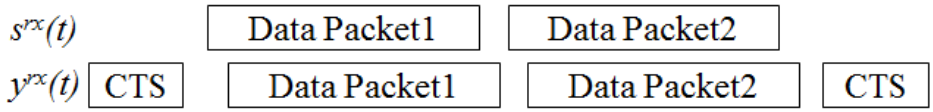

Figure 5.3: Transmission of CTS-to-self packets by AF-FDR.

In general, there are 3 different scenarios that can occur as FDR proceeds with transmitting CTS-to-self, aiming for accurate channel estimate.

Case 1: When FDR is powered up it goes through an initialization phase, where it collects information about the network as well as valid SI channel estimates $\hat{\boldsymbol{h}}^{\boldsymbol{si}}$. In this phase the validity of $\hat{\boldsymbol{h}}^{\boldsymbol{si}}$ is verified by rejecting the outliers from multiple channel estimates followed by statistical averaging.

Case 2: When FDR gains access to the medium, transmission of CTS frame has started and no other station is allowed to transmit. As a result received signal consists of SI only, and the received i^{th} block of pilot data can be expressed as

$$p_i(n) = y_i^{tx}(n-\tau) * h_i^{si}(n) + w(n). \tag{5.4}$$

Using $p_i(n)$ from (5.4) FDR estimated the time delay of SI by correlating the received signal

with locally stored training sequence, and searches for a peak position as described below.

$$\hat{\tau} = \arg\max_{n} \Big[\sum_{m=1}^{W_d} p_i(m) \cdot p_i^{si*}(m+n) \Big], \tag{5.5}$$

where $p_i^{si}(n)$ is the local copy of i^{th} block of SI preamble, and W_d is the correlation window width. Once position of SI is determined, the least square (LS) estimation of its channel can be carried out in frequency domain as

$$\hat{H}_i^{si}(k) = \frac{P_i(k)}{Y_{i,\hat{\tau}}^{tx}(k)} = \frac{Y_{i,\tau}^{tx}(k) H_i^{si}(k) + W(k)}{Y_{i,\hat{\tau}}^{tx}(k)}, \tag{5.6}$$

where $\hat{H}_i^{si}(k)$ is the i^{th} SI channel estimate. $P_i(k)$, $Y_i^{tx}(k)$, $W(k)$ are frequency domain representations of $p_i(n)$, $y_i^{tx}(n)$, $w(n)$ respectively. After acquiring the recent SI channel estimate, FDR uses it to cancel SI from the received signal $u_i(n)$. As a result the i^{th} block of received data packet after AC is given by (5.3). Since AF-FDR is not interested in decoding SOI, it will amplify and re-transmit $\boldsymbol{d_i}$ as the next step.

Case 3: Due to the random access mechanism of Wi-Fi network, it is possible that upon transmitting CTS-to-self by FDR, another station begins transmitting simultaneously. The two transmissions will collide, contaminating received CTS, and will result in corruption of the new SI channel estimate. Note that there is neither collision sense (CS) mechanism, nor CTS-to-self acknowledgement. Cyclic Redundancy Code (CRC) field of a Wi-Fi frame allows receiver to test validity of the packet, however that requires decoding the packet, which AF-FDR is unable to do. To check, whether the training signal has been contaminated or not, we propose the following technique.

First the FDR buffers the frame and detects the i^{th} block boundary of SI. Then it uses the previous channel estimate $\hat{h}_{i-1}^{si}(n)$ to perform subtraction of Tx copy of SI training from Rx

training signal $p_i(n)$ as

$$\delta_i = \frac{1}{N_{FFT}} \sum_{n=1}^{N_{FFT}} \left| p_i(n) - y_i^{tx}(n - \hat{\tau}) * \hat{h}_{i-1}^{si}(n) \right|^2, \tag{5.7}$$

where δ is the received residual power after subtraction. If after performing self-subtraction of CTS-to-self frame, there is still significant residual power left, then the CTS-to-self has collided and the new channel estimate is discarded. However, if after performing self-subtraction on $p_i(n)$, the remaining power of δ is below a predefined threshold, then CTS-to-self was successful, and channel estimate is updated with the new one.

$$\hat{h}^{si}(n) = \begin{cases} \hat{h}_i^{si}(n) & \delta_i < \eta \\ \hat{h}_{i-1}^{si}(n) & otherwise, \end{cases} \tag{5.8}$$

where η is a predefined power threshold level.

Given there was no collision, the remaining power δ, after self-subtraction of CTS, depends on the difference between the current SI channel $h_i^{si}(n)$, and the previous SI channel estimate $\hat{h}_{i-1}^{si}(n)$, which is a function of the coherence time of the channel. Section 5.5 presents numerical simulation results to quantify the performance of the proposed techniques.

5.4.2 Proposed DF-FDR Solution:

As discussed earlier this type of relay is non-transparent and decodes incoming packets before re-transmission in order to only relay the packets that are directed to its stations. Because DF relay appears as AP for the stations located in extended coverage area, it has to broadcast management packets to its clients periodically such as beacon frames [23]. In addition, it has to send Request to Send (RTS)/CTS or CTS-to-self to reserve the medium and avoid hidden node problem [23]. Those transmission are typically in HD mode creating

a great opportunity for DF-FDR to estimate SI channel and its delay without increasing the channel usage.

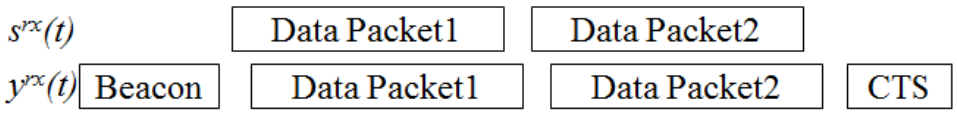

Figure 5.4: Transmission of Beacon and CTS-to-self packets by DF-FDR.

Estimation is performed taking similar approach for AF counterpart described by (5.5), (5.6).

Case 1, Slowly varying channel: DF-FDR uses its periodically transmitted beacons to acquire a valid SI channel estimate $\hat{\boldsymbol{h}}^{\boldsymbol{si}}$. As opposed to AF relay, DF relay has the ability to decode a packet, and therefore it can use CRC checksum in addition to AF-FDR test method to verify validity of SI channel estimate.

Case 2, Fast varying channel: Since typical beacon transmission period is approximately 100ms, besides transmitting beacon, DF-FDR will need to transmit CTS-to-self in between two beacons to be able to track the fast varying channel.

Once recent SI channel estimate is acquired, DF-FDR uses it to cancel SI in received signal $\boldsymbol{r_i}$. As a result i^{th} block received signal after active cancellation is given by (5.3). Since DF-FDR is expected to continue with decoding SOI, it has to estimate and remove timing and frequency errors from $\boldsymbol{g_i}$.

$$\hat{\theta} = \arg\max_{n} \Big[\sum_{m=1}^{W_d} p_i(m) \cdot p_i^{soi*}(m+n) \Big], \tag{5.9}$$

where $p_i^{soi}(n)$ is the local copy of i^{th} block of SOI preamble, $\hat{\theta}$ is the estimated time offset of SOI component.

5.5 Simulation Results

The AF-FDR system is simulated according to the parameters listed in Table 5.1. The aim is to relay Wi-Fi data packets without amplifying SI. FDR has passive SI cancellation capability of 60dB [43]. FDR transmits CTS-to-self packets periodically to acquire SI channel and delay estimates, which are used to perform AC on every consecutive data packet until next SI training cycle.

To quantify the impact of SI channel estimation frequency on SI cancellation, the FDR system is simulated for different CTS-to-self transmission periods and the cancellation gain is plotted in Figure 5.5, for static as well as dynamic channels. For CTS transmission periods that are less then 5ms, cancellation gains are almost identical for static and dynamic channels.

OFDM Parameters	**Value**	**Signal Parameters**	**Value**
OFDM Subcarriers	64	Channel Type	D
Data Packet Duration	1.6ms	AWGN Power	-100 dBm
Cyclic Prefix (CP)	$3.2\mu s$	Rx SOI Power	-70 dBm
Symbol Duration (CP+FFT)	$16\mu s$	Rx SI Power	-65 dBm
CTS+DIFS Duration	$130\mu s$	Tx Power	+15dBm
Inter-carrier spacing	78125 Hz	Carrier Frequency	2.5 GHz

Table 5.1: Simulation parameters

As the training frequency of SI channel is reduced, packets that have experienced a fading channel exhibit a degradation in cancellation gain commensurate with the Doppler of the channel. This effect can be reduced by increasing the frequency of CTS training, at the expense of increased channel utilization shown in Figure 5.6, which illustrates the percentage of time that channel is occupied by the CTS plus its associated distributed interframe space (DIFS), as a function of the training period.

Figure 5.6 suggests, that in lightly loaded networks, where packet collision rate is negligible,

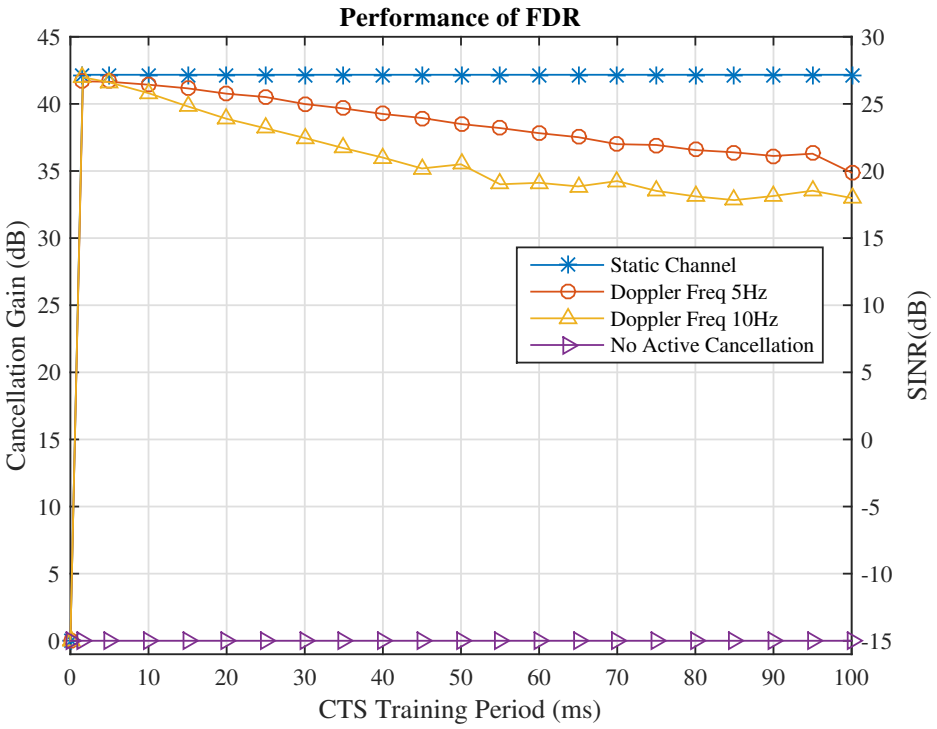

Figure 5.5: Active Cancellation Gain vs. CTS-to-self period.

SI channel estimation can be done as often as every 1ms, with approximately 6% channel utilization. However increasing the CTS-to-self transmission period slightly e.g up to 5ms, lowers channel utilization down to 1.5% with less than 1dB cancellation gain loss at 10 Hz Doppler.

To determine whether or not the received CTS-to-self packet is contaminated, FDR performs collision detection test on received CTS-to-self frame described by (5.7), (5.8). Figure 5.7 illustrates power of received CTS-to-self packet and residual power δ, in a fading channel with a Doppler frequency of 10Hz. The graph shows that as the previous estimate ages, as long as no collision occurs, residual power increases over time, showing a increase of 10dB over a duration of 100ms. Figure 5.7 further suggests that a good value for the predefined threshold η is -85 dB for this system (eqs. (5.8).

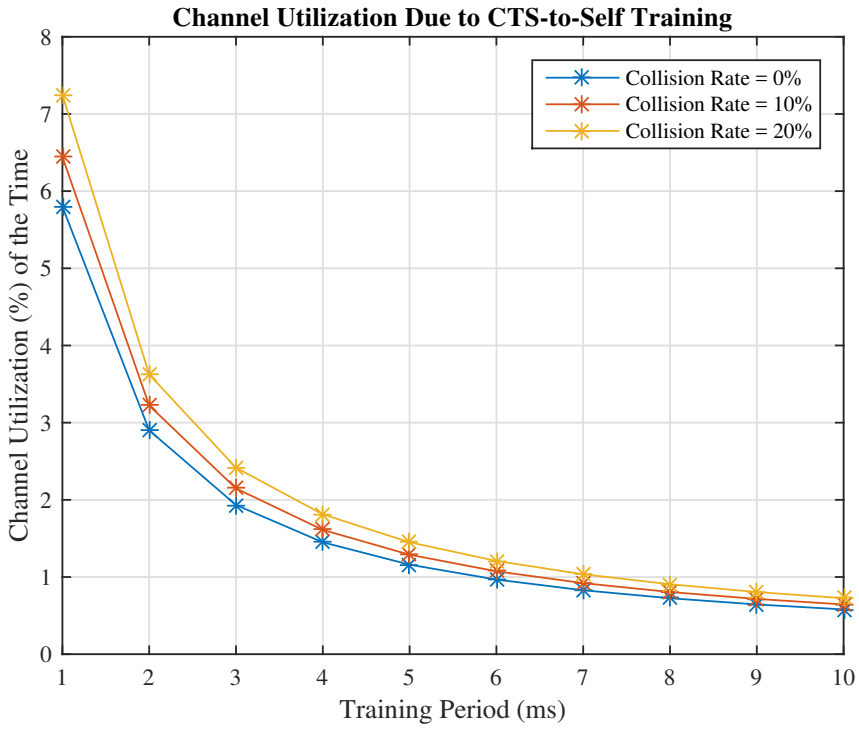

Figure 5.6: Percentage of Time the Channel is Occupied by CTS-to-self.

5.6 Conclusion

This chapter presented active suppression of SI by AFR in Wi-Fi OFDM networks. The major challenges are SI channels and delay estimation, while maintaining compliance with the standardized Wi-Fi packet structure and procedures. A novel SI channel estimation using self CTS technique is presented, that allows SI suppression below noise floor even under severe channel conditions, without requiring hardware/software changes of existing wireless nodes. Simulation results are presented showing the effectiveness of the proposed technique in relation to channel utilization cost.

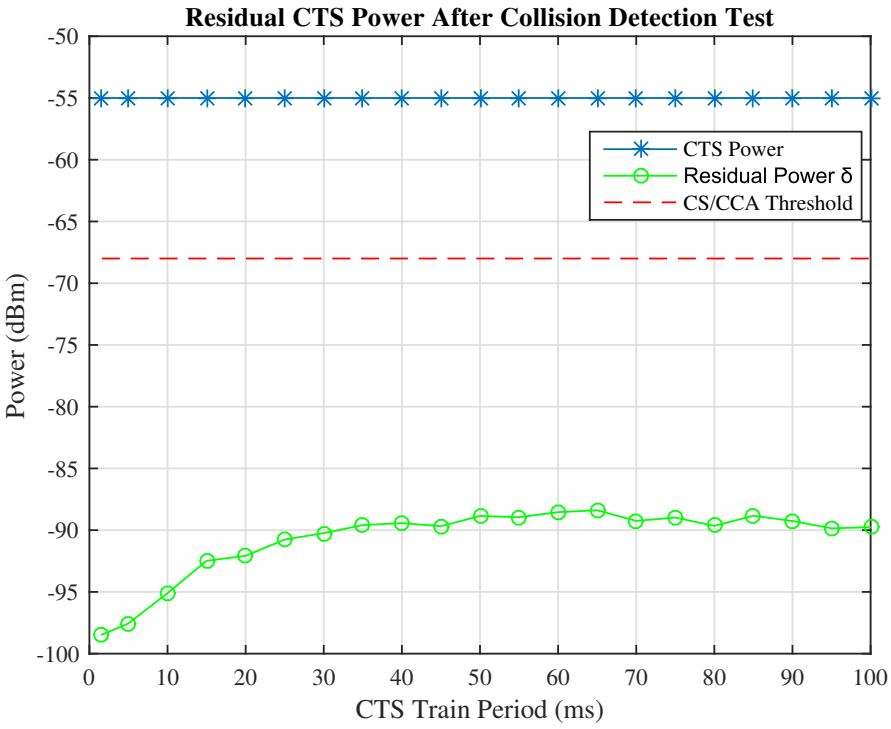

Figure 5.7: Residual Power of CTS-to-self in 10Hz Doppler Channel.

Chapter 6

Design and Implementation of an End-to-End Amplify and Forward Full-Duplex Relay Network

6.1 Introduction

Wireless network users are increasingly demanding better coverage and higher data rates. One way to address these issues is to transmit the signal through relays [6]. The addition of a relay station (RS) to an existing network is a common solution when wireless coverage extension is required in the absence of a connection to the backbone network. Half-duplex (HD) relays employ two different frequencies, time slots, or orthogonal spreading codes to prevent the transmitted signal from interfering with its own receiver. In contrast, full-duplex relays (FDR) utilize wireless resources more efficiently by transmitting and receiving simultaneously on the same frequency band, creating the potential of doubling the system throughput, when compared to their Half Duplex (HD) counterparts [46, 47]. Although

the FDR has higher transmission efficiency, it suffers from Self Interference (SI), since the transmitted signal by the FDR is received as an in-band blocker by its own receiver. The SI signal results in system instability, and poor signal to interference plus noise ratio (SINR) for the signal that is intended to be relayed [55]. In order to use an FDR for higher efficiency, SI must be coherently canceled to provide stability and a satisfactory level of SINR of the received signal before amplifying and forwarding it. To achieve sufficient SI suppression FDR relies on cancellation across multiple domains (spatial, analog and digital cancellation) [44].

Numerous techniques are available for SI suppression, including passive (e.g. antenna separation, directional antennas etc.) and active (analog and digital) cancellation [51, 37]. Active cancellation (AC) is based on the knowledge of the SI channel state information. In multi-relay networks, the problem of interference can become more challenging, because if all the nodes transmit simultaneously on the same frequency, the receive nodes experience interference from other transmit nodes in addition to SI [38]. Therefore, in this type of networks, the relay selection algorithms serve as an additional mechanism of maximizing the end-to-end SINR or the system throughput under power consumption constraints [4, 36, 29].

Several antenna structures have been designed for full-duplex nodes, increasing SI suppression in the propagation domain. The loop-back interference of a full-duplex relay has been studied in [20], where the relay is equipped with dual-polarized antennas, intended for outdoor-to-indoor relaying. The isolation between transmit and receive paths for different antenna configurations is evaluated experimentally. Implementation of a low-complexity full-duplex radio with a single antenna has been proposed in [3], where a dual-polarized antenna is designed, eliminating the need for circulator and achieving 60dB passive SI suppression.

Self-interference cancellation of a full-duplex relay is studied in [27], where the relay is equipped with back-to-back transmit and receive antennas, which is capable of providing 2x2 MIMO operation. Evaluation of SI suppression capability was carried out experimentally, in different real multi-path environments, both indoor and outdoor. Combining this passive

SI suppression technique with digital cancellation resulted in over 100dB SI suppression.

Several end-to-end full-duplex relay networks have been implemented, and the performance of the overall system has been experimentally evaluated. In [9], simultaneous bidirectional multi-hop relaying is studied, where a training strategy is proposed to address loop-back interference cancellation and power amplification challenges. Up to 3 relays bidirectional relay network has been implemented using National Instruments NI-5791 software-defined radio platforms, where noise propagation was studied and evaluated at the end nodes.

In [12], SI and intra-flow interference (IFI) suppression technique of multi-hop relay network is presented, using a proposed Media Access Control (MAC) protocol, that supports the estimation of SI and IFI channels. A network consisting of tandem relays was simulated, and end-to-end throughput was presented as a function of SI suppression level and number of relays in the network. The authors experimentally verified the performance of the proposed MAC protocol and its cancellation capability of SI and IFI.

In the extended wireless networks, the optimal power allocation and relay location selection have been studied under different constraints. In [21], power allocation and location selection of decode and forward relay have been proposed, which minimizes outage probability. Simulation results show that the proposed optimal power allocation scheme has lower outage probability compared to equal power allocation, especially when the SI level is high. In addition, it was shown that placing FDR closer to the destination leads to better system performance, in the cases when FDR has strong decoding capability.

Joint optimal power allocation and relay selection have been studied in [49], maximizing system information rate under limited transmit power constraint.

Relay selection based on the enhancement of network physical layer security has been analyzed by [15]. Two schemes of optimal relay selection have been proposed, where the first scheme maximizes the end-to-end security capacity, and the second scheme maximizes the

partial SINR at the relay station. The secrecy outage probability as a function of selected relay and average SNR was derived numerically and confirmed by Monte Carlo simulation.

The Performance of full-duplex relay selection in cognitive underlay networks has been analyzed in [25], targeting either coverage extension or throughput enhancement. Diversity gain evaluation of the relay selection in the presence/absence of a direct link has been performed in Rayleigh fading channel. Results show that significant diversity can be recovered even in the presence of direct interference.

The analysis of power allocation and location optimization of the full-duplex amplify-and-forward relay was presented by [31]. Allocation of source transmit power level, and optimal relay location was derived that maintains the quality of the received signal at the relay system. The performance of a single relay system is evaluated by simulation for three optimization schemes such as power allocation, relay location and joint power allocation, and location optimization.

While there is a significant amount of work in literature studying the theoretical aspects of full-duplex systems, there is a limited amount of work that analyzes and experimentally evaluates practical deployment scenarios for FDRs under constant gain and/or constant transmit power. In this chapter, we present the design and implementation of an FDR platform under realistic wireless network deployment scenarios, with the following specific contributions:

- We analyze FDR gain limitations and derive stability bounds under limited SI suppression and transmit power constraints, confirming the stability region experimentally.
- Tandem FDR network performance is analyzed, and patch antennas are designed for minimizing inter-relay interference.
- The network performance as a function of FDR location is analyzed for the cases when

FDR operates either in constant gain or constant transmit power modes.

- The received signal at the destination node, as a function of relay location is evaluated with both simulation and experimentally.
- Indoor and outdoor scenarios are considered, and performance gains are confirmed experimentally.
- Optimum relay placement for maximizing destination SINR is presented experimentally, and verified analytically.

The remainder of the chapter is organized as follows. In Section 6.2, a network extended by FDR is described, and challenges are outlined. In Section 6.3, the maximum gain limits are derived under the stability, and maximum available transmit power constraints. Section 6.4 presents a tandem FDR network highlighting the challenges and proposes a modification to FDR, reducing the problem complexity. The SINR analysis of extended signal by a single FDR is presented in Section 6.5. Performance results of the simulated and experimental system under different channel conditions are presented and compared in Section 6.6. Relay selection strategy maximizing destination SINR is discussed in Section 6.7. The chapter is concluded in Section 6.8.

Notation: We use $(*)$ to denote convolution, $(.)^*$ to denote conjugate, $E[.]$ to denote expectation, and $arg[.]$ to denote argument of a complex number. Time domain variables are represented as lowercase letters, while frequency domain variables use uppercase. Furthermore, bold lowercase letters indicate vectors.

6.2 System Model

Figure 6.1 illustrates a network consisting of a transmitting station, also referred to as source (S) node, and a receiving station referred to as destination (D) node. For simplicity, we will assume that the destination node is located outside of the source coverage, and does not receive service. To extend the coverage, an FDR is placed at the boundary of the source's cell. All the stations are assumed to be using Orthogonal Frequency Division Multiplexing (OFDM), that employs N_{FFT} subcarriers with inter-carrier spacing $\Delta f = \frac{f_s}{N_{FFT}} = \frac{1}{N_{FFT}T_s} = \frac{1}{T_{sym}}$. T_s is sampling period, f_s is sampling frequency and T_{sym} is one OFDM symbol duration.

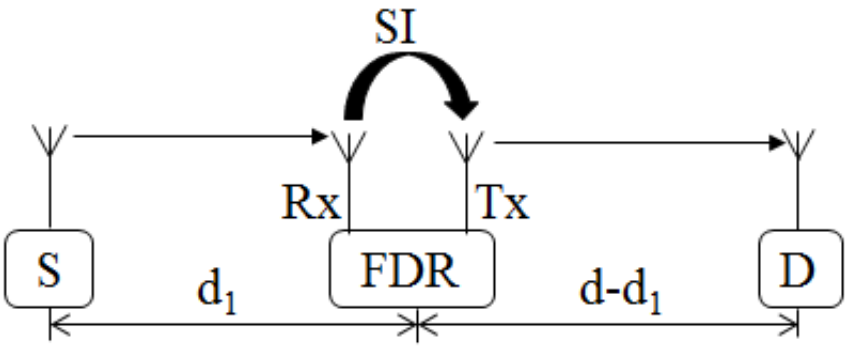

Figure 6.1: Diagram of extended network by full duplex relay.

6.2.1 Relay Station

The relay station is either classified to be Amplify and Forward (AF) type or Decode and Forward (DF) type. AF-FDR does not have a demodulation/decoding block in the receive chain [10]. The relay station receives and transmits packets on the same frequency and in the same time slot. The signal that FDR is aiming to receive is the signal of interest (SOI). The transmitted signal by RS is also received by its own receiver, causing self-interference;

thus the i^{th} block of the received signal by the relay station can be modeled as

$$r_i(n) = s_i^{rx}(n) + y_i^{rx}(n) + w_i^r(n), \tag{6.1}$$

where $s^{rx}(n)$ and $y^{rx}(n)$ are SOI and SI components of the received signal. $w^r(n)$ is Additive White Gaussian Noise (AWGN).

In general, SI power is orders of magnitude larger than SOI, due to the fact that the distance between Tx and Rx antennas of FDR is significantly smaller compared to the distance between any transmitting node and FDR. In order to successfully receive SOI and re-transmit it with high gain, while maintaining stability, proper isolation is required between Tx and Rx chains of FDR [32] [39], which is difficult to achieve with passive SI suppression only. Active suppression relies on the accurate knowledge of the SI component; hence we detail SI channel estimation impact on active cancellation performed by FDR in Section 6.3.2.

6.2.2 Signal Propagation Model

The model representing source to destination signal propagation channel is illustrated in figure 6.2, which is used for simulation purposes. The signal path from source to destination is a chain of channels consisting of a source-relay, relay-relay, and relay-destination subchannels.

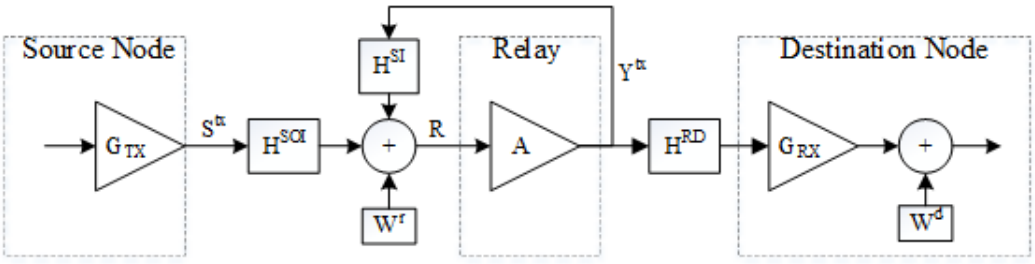

Figure 6.2: Source to destination signal path model with signal impairments.

Source-Relay

Assuming perfect synchronization between the nodes, source to relay channel represents the SOI propagation effects in the wireless channel denoted as H^{soi}, which includes path loss and Rayleigh fading effects.

Relay-Relay

Ignoring the propagation delay between Tx and Rx chains, relay to relay channel represents the SI propagation effects in the wireless channel denoted as H^{si}. The SI channel, H^{si}, is modeled to reflect path loss and Rayleigh fading effects. In addition, it assumes the use of passive self-interference suppression due to TX/RX antenna separation plus the use of directional antennas. Finally, AWGN w^r is added to the composite signal $r(n)$, which represents the overall noise of the FDR receive chain.

Relay-Destination

Forwarded signal towards destination passes through a channel H^{RD}, which is modeled to reflect path loss and Rayleigh fading effects. The path loss factors of H^{soi} and H^{RD} are a function of distance d_1 and $d - d_1$ respectively, hence increasing one results in a decrease of the other. At the destination, the overall noise of the received chain w^d is added, which is modeled as AWGN.

Assuming all the nodes are perfectly synchronized, the received signal by the FDR in (6.1)

can be rewritten in terms of transmitted signals and corresponding channel response as

$$r_i(n) = s_i^{tx}(n) * h_i^{soi}(n) + y_i^{tx}(n) * h_i^{si}(n) + w_i^r(n), \tag{6.2}$$

where $h^{soi}(n)$ and $h^{si}(n)$ represent SOI and SI channels responses respectively.

6.3 Gain and Stability Analysis

The coverage of the extended network by relay station depends on the amplification gain of FDR. Amplification gain itself is limited by the available power and stability of FDR. Since AF-FDR transmits the amplified version of the received signal after multiple SI cancellation mechanisms, we will derive stability conditions for passive and active cancellation separately. We will then confirm the derived stability region with an experiment.

6.3.1 Passive SI cancellation

Assuming that relay amplifies the signal by a factor of A, after passive cancellation, the transmitted i^{th} block of the signal from relay can be expressed as

$$y_i^{tx}(n) = Ar_i(n), \tag{6.3}$$

where A is the amplification gain and the delay in the circuit elements is neglected. Substituting (6.3) into (6.1) results in

$$\frac{y_i^{tx}(n)}{A} = s_i^{rx}(n) + y_i^{tx}(n) * h_i^{si}(n) + w_i^r(n). \tag{6.4}$$

After transferring (6.4) to frequency domain, the transmitted signal is expressed as

$$Y_i^{tx}(k) = \frac{A(S_i^{rx}(k) + W_i^r(k))}{1 - AH_i^{si}(k)}. \tag{6.5}$$

Equation (6.5) represents a positive feedback system, which has to satisfy the Nyquist criterion for every subcarrier k, in order to be stable. Proper selection of parameters A and H^{si} can lead to stability even in the presence of positive feedback [39]. However, H^{si} is difficult to control since it depends on the medium. Therefore, amplification gain A must be chosen to satisfy the Nyquist stability criterion for every subcarrier as

$$|AH^{si}(k)| < 1 \quad for \quad 0 < k < N_{FFT} - 1, \tag{6.6}$$

which ensures that the number of poles of A equal number of anti-clockwise turns of the Nyquist contour of AH^{si} around the point 1. Selection of amplification gain value for individual subcarrier is impractical, hence the subcarrier experiencing the largest product of $|AH^{si}(k)|$ will be the limiting factor of A. In order to maintain finite system gain, the condition $\max_k[|AH_i^{si}(k)|] < 1$ must be satisfied. Therefore, for the case when the gain is a scalar, the stability bounds on A are given as

$$0 < A < \frac{1}{H_{i,max}^{si}}, \tag{6.7}$$

where $H_{i,max}^{si} = \max_k[|H_i^{si}(k)|]$. From (6.5), the maximum system gain can be expressed as

$$G_{sys} = \max_k \left[\frac{A}{1 - AH_i^{si}(k)}\right] = \frac{A}{1 - AH_{i,max}^{si}}. \tag{6.8}$$

In general, the available transmit power of FDR P_T is limited. Hence the average power of transmitted signal Y_i^{tx} should be bounded as

$$E\big[|Y_i^{tx}(k)|^2\big] = E\big[|G_{sys}(S_i^{rx}(k) + W_i^r(k))|^2\big] \leq P_T. \tag{6.9}$$

In the above inequality, G_{sys} is a function of FDR gain A, SI channel $H^{si}_{i,max}$, and it is independent on received signal plus noise. Therefore, the expression in (6.9) can be rewritten as

$$E\left[|G_{sys}|^2\right]P_{SN} \leq P_T, \tag{6.10}$$

where $P_{SN} = E[|S^{rx}_i(k)|^2] + E[|W^r_i(k)|^2]$ represents the received signal plus noise power at FDR. Denoting $\alpha = \max_k[|H^{si}_i(k)|]$, which corresponds to the minimum SI suppression coefficient, the inequality in (6.10) can be rewritten as

$$\frac{A^2 P_{SN}}{(1-\alpha A)^2} \leq P_T. \tag{6.11}$$

The left-hand side in (6.11) represents power amplification of P_{SN}, under available transmit power constraint. To determine the amplification gain range for which FDR is stable, the following inequality must be solved

$$(P_{SN} - \alpha^2 P_T)A^2 + 2\alpha P_T A - P_T \leq 0. \tag{6.12}$$

The roots of the above quadratic equation are computed as

$$A_{1,2} = \frac{-\alpha P_T \pm \sqrt{P_T P_{SN}}}{P_{SN} - \alpha^2 P_T}. \tag{6.13}$$

Since $P_{SN} - P_T\alpha^2 > 0$, the roots $A_{1,2}$ can be rewritten as:

$$A_1 = -\frac{\sqrt{P_T P_{SN}} + \alpha P_T}{P_{SN} - \alpha^2 P_T}, \tag{6.14}$$

$$A_2 = \frac{\sqrt{P_T P_{SN}} - \alpha P_T}{P_{SN} - \alpha^2 P_T}, \tag{6.15}$$

where both numerators and denominators are positive numbers. Since $A_1 < 0$ and $A_2 > 0$, the amplification gain range satisfying (6.12) is computed as

$$0 \leq A \leq \frac{\sqrt{P_T P_{SN}} - \alpha P_T}{P_{SN} - \alpha^2 P_T}. \tag{6.16}$$

To keep the output of the FDR stable under limited transmit power constraint, the gain FDR must be bounded by the limits derived in (6.16), where the upper bound is a function of SI suppression amount and received power. For example, figure 6.4 is a screen capture of the spectrum analyzer. It illustrates an event where the output of FDR is unstable and transmits self-generated frequency by FDR at 2.542GHz (Marker 2) while SOI is absent (Marker 1).

6.3.2 Active SI Cancellation

Recall, that active cancellation relies on subtraction of known transmitted SI from the signal being received. Assuming all the nodes are perfectly synchronized, after digital cancellation i^{th} block of the received signal $g_i(n)$ can be expressed as

$$g_i(n) = r_i(n) - y_i^{tx}(n) * \hat{h}_i^{si}(n) = s_i^{tx}(k) * h_i^{soi}(n) + y_i^{tx}(n) * [h_i^{si}(n) - \hat{h}_i^{si}(n)] + w_i^r(n). \tag{6.17}$$

where $\hat{h}^{si}(n)$ is SI channel estimate. After performing active SI cancellation, the signal is amplified and transmitted to the destination, expressed as

$$y_i^{tx}(n) = A g_i(n). \tag{6.18}$$

Using expression of $g_i(n)$ from (6.17), the (6.18) can be expressed as

$$\frac{y_i^{tx}(n)}{A} = s_i^{rx}(n) + y_i^{tx}(n) * [h_i^{si}(n) - \hat{h}_i^{si}(n)] + w_i^r(n). \tag{6.19}$$

Transforming (6.19) to frequency domain, the transmitted signal is expressed as

$$Y_i^{tx}(k) = \frac{A(S_i^{rx}(k) + W_i^r(k))}{1 - A(H_i^{si}(k) - \hat{H}_i^{si}(k))}. \tag{6.20}$$

After denoting the channel estimation error at subcarrier k as

$$E_i^{si}(k) = H_i^{si}(k) - \hat{H}_i^{si}(k), \tag{6.21}$$

and substituting into (6.20), the transmitted signal by FDR is expressed as

$$Y_i^{tx}(k) = \frac{A}{1 - AE_i^{si}(k)}(S_i^{rx}(k) + W_i^r(k)). \tag{6.22}$$

By comparing (6.22) and (6.5), it is easy to notice that the two expressions have a similar form. In the case of active cancellation, the transmitted signal is a function of SI channel estimation error as opposed to SI channel magnitude. Therefore, in this case, the limiting factor of FDR gain will be the subcarrier with the largest $|AE_i(k)|$ product. In order to maintain a finite system gain $|AE_i(k)| < 1$ for $\forall k$, which implies that inequality $\max_k[|AE_i^{si}(k)|] < 1$ must be satisfied, resulting in

$$0 < A < \frac{1}{E_{i,max}^{si}}, \tag{6.23}$$

where $E_{i,max}^{si} = \max_k[|E_i^{si}(k)|]$. Using (6.22), the maximum system gain is expressed as

$$G_{sys} = \max_k \left[\frac{A}{1 - AE_i(k)}\right] = \frac{A}{1 - AE_{i,max}^{si}}. \tag{6.24}$$

To determine the gain under limited transmit power constraint, the transmitted signal power must be bounded as

$$E\big[|Y_i^{tx}(k)|^2\big] = E\big[|G_{sys}(S_i^{rx}(k) + W_i^r(k))|^2\big] \leq P_T. \tag{6.25}$$

In the above inequality, the G_{sys} is independent of received signal plus noise, therefore (6.25) can be rewritten as

$$E\left[|G_{sys}|^2\right] P_{SN} \leq P_T. \tag{6.26}$$

For simplicity, we substitute $\beta = E^{si}_{i,max}$, which is the maximum channel estimation error in the i^{th} received block of data. As a result, the expression in (6.24) can be rewritten as

$$\frac{A^2 P_{SN}}{(1-\beta A)^2} \leq P_T. \tag{6.27}$$

Expression in (6.27) is similar to (6.11), and therefore the solution can be carried out following analogous steps. From (6.27), we get the following inequality

$$(P_{SN} - \beta^2 P_T)A^2 + 2\beta P_T A - P_T \leq 0. \tag{6.28}$$

The roots of quadratic expression in (6.28) are

$$A_{1,2} = \frac{-\beta P_T \pm \sqrt{P_T P_{SN}}}{P_{SN} - \beta^2 P_T} \tag{6.29}$$

Since $P_{SN} - \beta^2 P_T > 0$, it follows that, to satisfy inequality in (6.28) the gain must be bounded as

$$0 \leq A \leq \frac{\sqrt{P_T P_{SN}} - P_T E_{i,max}}{P_{SN} - P_T E^2_{i,max}} \ . \tag{6.30}$$

6.3.3 Stability Discussion

In the case, when FDR has small available power, the gain will be limited, keeping it below the isolation level of Tx and Rx chains. In this case, the relay is always in a stable state. However, as available Tx power increases, it enables higher gain settings. To increase the radio coverage while keeping the system stable, the gain can be increased until reaching the

isolation level, as shown in figure 6.3. Slight increase of available transmit power along with the gain, that is above the isolation level, will cause the generation of a jamming signal shown in Figure 6.4.

In the case, when FDR has very large available power, in order to achieve stability, the gain of the FDR should be limited by isolation between Tx and Rx chains. Therefore, for FDR with passive SI suppression, the gain is inversely proportional to the SI channel strength, and for FDR with active SI suppression, the gain is inversely proportional to the SI channel estimation error, as shown in Table 6.1. Since FDR has very large available power, setting the gain value exceeding the isolation amount will cause the generation of continuously increasing signal, which will eventually damage the hardware.

Tx Power	**Passive Cancellation**	**Active Cancellation**
Unlimited	$0 < A < \frac{1}{H^{si}_{i,max}}$	$0 < A < \frac{1}{E_{i,max}}$
Limited	$0 < A < \frac{\sqrt{P_T P_{SN}} - \alpha P_T}{P_{SN} - \alpha^2 P_T}$	$0 < A < \frac{\sqrt{P_T P_{SN}} - P_T E_{i,max}}{P_{SN} - P_T E^2_{i,max}}$

Table 6.1: Full-duplex relay gain limits.

6.4 SINR Analysis for Tandem FDR Network

In this section, a tandem network consisting of L full-duplex relays connected in series is studied. First, we consider relays equipped with omnidirectional antennas. Then the drawbacks are highlighted, and a tandem network of relays equipped with directional patch antennas are designed to mitigate these issues.

6.4.1 Tandem Relay Network with Omnidirectional Antennas

Figure 6.5 illustrates a tandem relays network, where all the relays are equipped with omnidirectional antennas and assumed to have self-interference cancellation ability. Each relay is

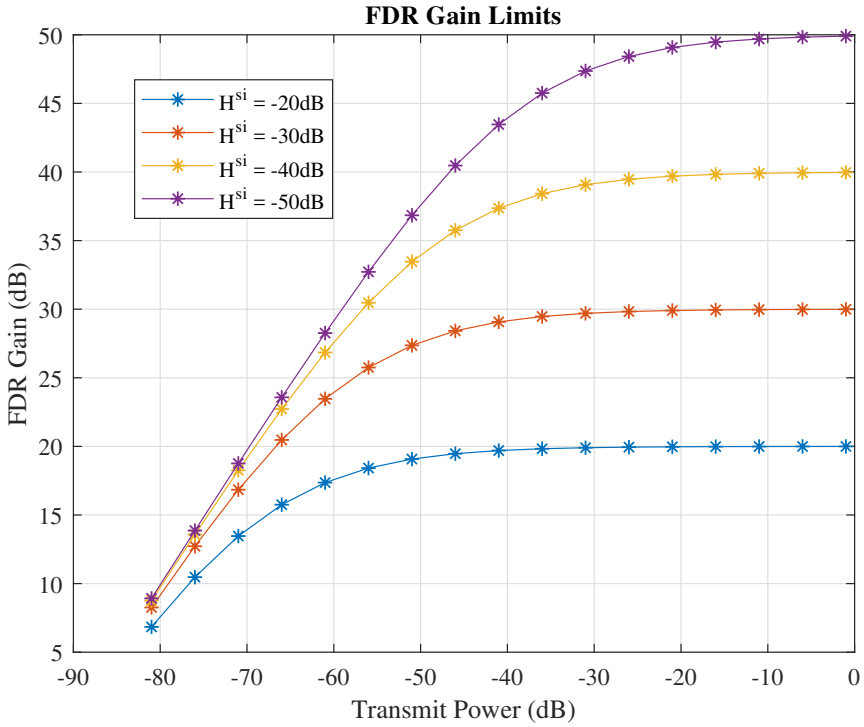

Figure 6.3: FDR gain under limited transmit power while $P_{SN} = -90dBm$.

positioned in the coverage area for its adjacent nodes. When relaying signals transmitted by the source node, every relay in the chain receives SOI, SI, and interference from transmissions of neighboring relays often referred to as inter-relay interference (IRI) [12]. For simplicity, we will assume that the transmitted signal strength of each relay is negligible beyond its adjacent neighbors. The received signal by l^{th} relay is expressed as

$$r_l(n) = x_{l-1}(n) * h_{l-1,l}(n) + x_l(n) * h_{l,l}(n) + x_{l+1}(n) * h_{l+1,l}(n)u(L-l-1) + w_l(n), \quad (6.31)$$

where $x_l(n)$ is transmitted signal by l^{th} relay and $u(l)$ is the unit step function. The third term in (6.31) represents the IRI, which is the signal transmitted by $l+1$ relay, and it interferes with received signal at l^{th} relay except for the case when $l = L$. This type of setup has two main drawbacks:

- Each relay, FDR_l, has to cancel the self-interference and interference from next relay,

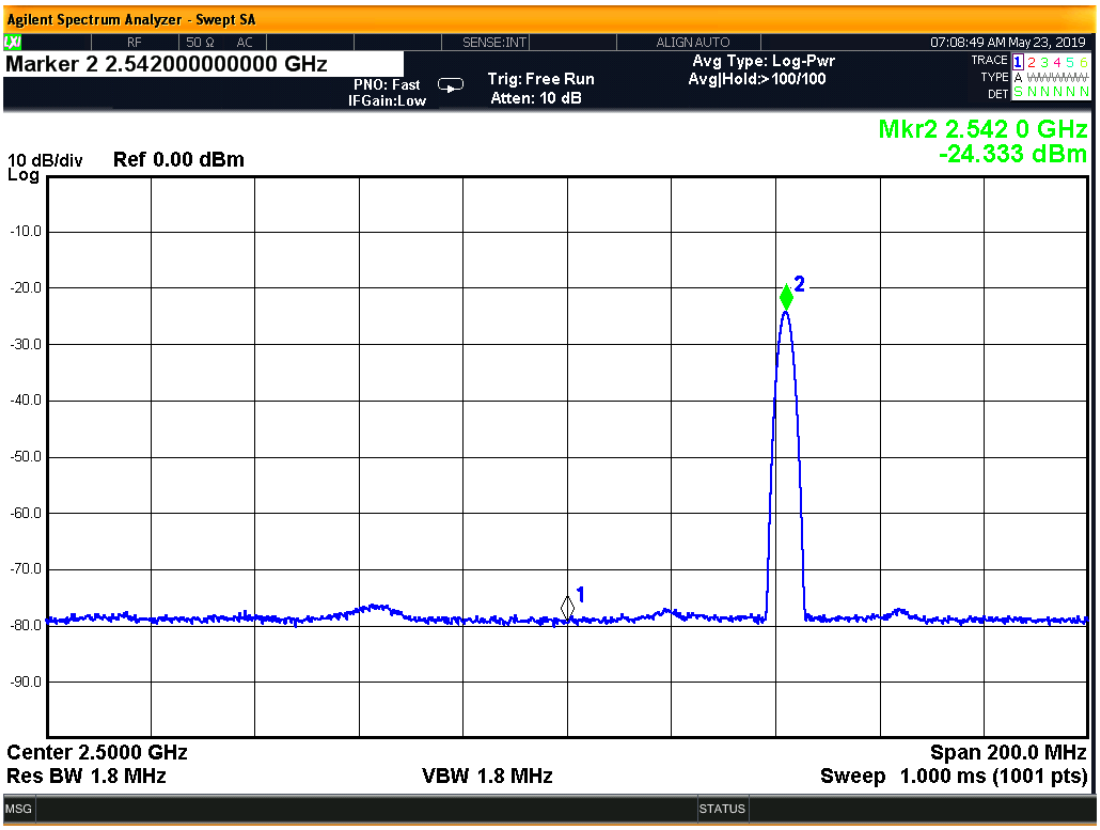

Figure 6.4: Signal generated by unstable FDR with gain of 58.25dB while SI isolation level of 58dB.

FDR$_{l+1}$, in order to extract the SOI from the received signal. This requires estimation of $h_{l+1,l}$ in addition to $h_{l,l}$, substantially increasing the SI cancellation complexity.

- Omnidirectional antenna wastes energy by extending the coverage in the direction already receiving coverage from previous FDR.

In order to compensate for these drawbacks, the omnidirectional antennas are replaced with patch antennas [1].

[1]FDR is assumed to be between the source and destination. If FDR is located beyond destination node, while there is no coverage by FDR for destination, with high probability the SNR at destination will be higher then the relayed.

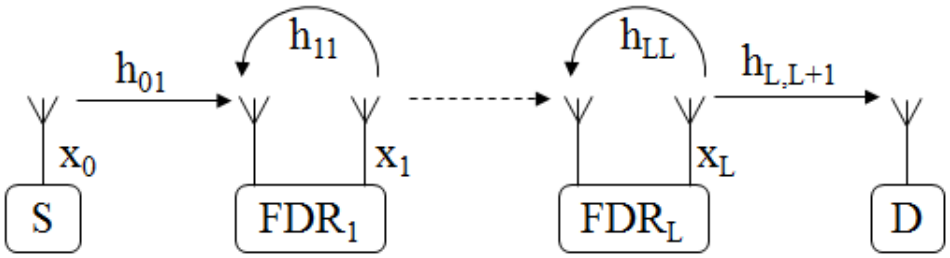

Figure 6.5: Network diagram of tandem FDRs equipped with omnidirectional antennas.

6.4.2 Tandem Relay Network with Patch Antennas

As the name suggests, the patch antenna is an electrically conductive flat structure separated from a ground plane by a dielectric substrate. In our design, we use a rectangular copper as a patch mounted on the FR4 substrate with a ground plane on the opposite side. The 3D model of our patch antenna overlapped with a simulated radiation pattern is shown in Figure 6.7. All the modeling and simulations of the antenna are performed in High Frequency Structure Simulator (HFSS) software [34, 26].

Figure 6.6 illustrates a tandem relay network equipped with antenna patches radiating in opposite directions.

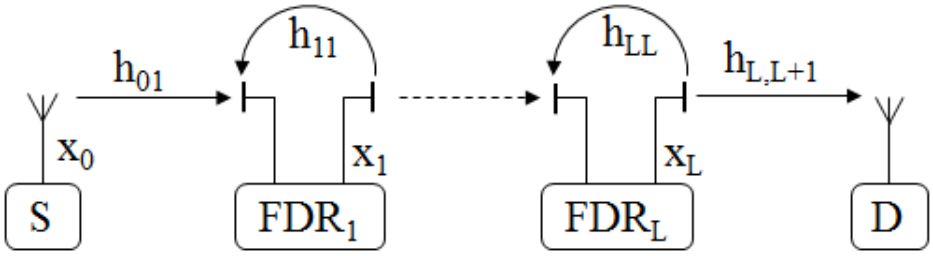

Figure 6.6: Network diagram of tandem FDRs equipped with patch antennas.

In this case, each FDR_l with $l > 1$ can receive signal from FDR_{l-1} but not vice versa. This modification has a number of advantages as follows:

- Due to the directivity of the patch antenna, IRI isolation is achieved.

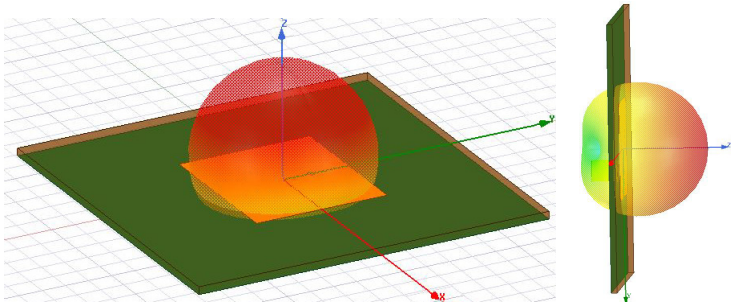

(a) Front View (b) Side View

Figure 6.7: HFSS Model of Patch Antenna overlapped with Radiation Pattern.

- Due to the directivity of the patch antenna, SI isolation is increased, consequently improving the coverage of FDR by allowing higher gain when necessary power is available. Recall that FDR gain is limited by SI suppression and available transmit power, as shown in Section 6.3.

- Increasing SI suppression in the propagation domain is preferred because it avoids saturation of Rx front-end.

- This type of arrangement of patch antennas uses transmit power efficiently by directing energy towards the extended area.

Notice that both simulated and measured radiation patterns of our patch antenna are showing small back lobes (Figure 6.7b and Figure 6.8), which means that, there is a small amount of backward radiation. Since the distance between FDR's TX and Rx antennas is short, the residual SI still remains, which is due to the backward radiation of the patch antenna as well as the presence of nearby reflector. However, considering sufficient distance between two nodes, the IRI becomes vanishingly weak. Therefore, the received signal by l^{th} relay is now reduced and can be expressed as

$$r_l(n) = x_{l-1}(n) * h_{l-1,l}(n) + x_l(n) * h_{l,l}(n) + w_l^r(n). \tag{6.32}$$

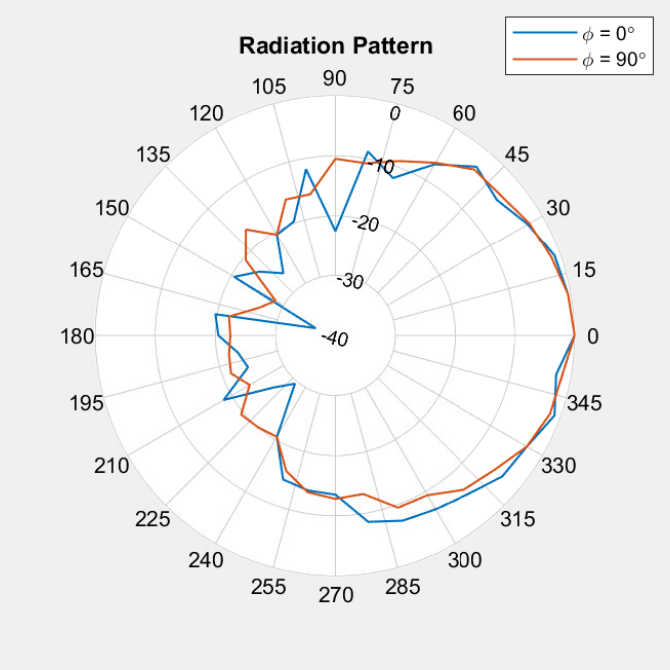

Figure 6.8: Measured Radiation Patterns of Fabricated Patch Antenna. The patterns are measured by swiping angle $\theta \in [0°; 360°]$ for $\phi = 0°$ and $\phi = 90°$.

Since (6.32) form is identical to received signal by single FDR given in (6.2), the active SI cancellation can be carried out as shown in (6.17). Hence, the amplified and re-transmitted signal by l^{th} relay can be written as

$$x_l(n) = A_l(x_{l-1}(n) * h_{l-1,l}(n) + w_l^{si}(n) + w_l^r(n)), \tag{6.33}$$

where $w_l^{si}(n)$ is the residual part of SI at FDR_l after applying SI cancellation. To solve equation (6.33), we express the transmitted signal $x_l(n)$ in terms of the originally transmitted signal by the source $x_0(n)$. Now one can transform (6.33) into frequency domain and write it as a system of l equations.

$$X_l(k) = A_l(X_{l-1}(k)H_{l-1,l}(k) + W_l^{si}(k) + W_l^r(k)). \tag{6.34}$$

The residual SI at FDR can be modeled as a Gaussian random variable with zero mean and variance proportional to transmit power [13]. Therefore, to simplify the expression in (6.34),

the two noise terms can be combined into interference plus noise terms as

$$W_l(k) = W_l^{si}(k) + W_l^r(k). \tag{6.35}$$

As a result, the expression in (6.34) can be rewritten as

$$X_l(k) = A_l(X_{l-1}(k)H_{l-1,l}(k) + W_l(k)). \tag{6.36}$$

Consequently, in the network consisting of $L \geq 2$ FDRs connected in series, the transmitted signal by l^{th} FDR for $2 \leq l \leq L$ can be expressed as

$$\begin{aligned} X_l(k) = (X_0(k)H_{01} + W_1(k))\, A_1 \prod_{i=2}^{l} A_i H_{i-1,i}(k) + \\ A_l W_l(k) + \sum_{m=2}^{l-1} \left[W_m(k) A_1 \prod_{i=m+1}^{l} A_i H_{i-1,i}(k) \right]. \end{aligned} \tag{6.37}$$

Denoting the product as

$$\zeta_m = \prod_{i=m}^{l} A_i H_{i-1,i}(k) \tag{6.38}$$

and substituting into expression (6.37), it can be rewritten as

$$X_l(k) = X_0(k)H_{01}A_1\zeta_2 + A_l W_l(k) + W_1(k)A_1\zeta_2 + \sum_{m=2}^{l-1} \left[W_m(k) A_1 \zeta_{m+1} \right]. \tag{6.39}$$

From (6.36), the transmit SINR of the FDR_1 can be expressed as

$$\text{SINR}_1 = \frac{E[|X_0(k)H_{01}(k)|^2]}{E[|W_1(k)|^2]}. \tag{6.40}$$

Meanwhile, the transmit SINR of FDR_l for the case when $2 \leq l \leq L$ can be computed from (6.39) as

$$\text{SINR}_l = \frac{E[|X_0(k)H_{01}(k)|^2]}{E[|W_1(k)|^2] + E\left[\frac{A_l W_l(k)}{\zeta_2} + \sum_{m=2}^{l-1} \left[W_m(k) \frac{\zeta_{m+1}}{\zeta_2} \right] \right]^2}. \tag{6.41}$$

By comparing (6.41) with (6.40), it becomes clear that every next FDR degrades the SINR of the desired signal.

6.5 Effect of Relay Location on SINR Analysis

As discussed in Section 6.4, the proposed back to back patch antenna setup helped to gain SI and IRI suppression for FDR systems, improving the SINR. However, relaying the signal through a long multi-hop AF-FDR chain introduces latency and degrades the SINR, as shown in (6.41). Therefore, relaying the signal through the nearest neighbor may not be the best choice and could lead to signal quality degradation at the destination. Recall that AF-FDR does not improve the SINR of the received signal by the relay, which means that poor SINR somewhere in the chain will propagate all way to the destination. To investigate the impact of FDR location on signal quality at the destination, in this section, we consider a single FDR equipped with patch antennas, as illustrated in Figure 6.9.

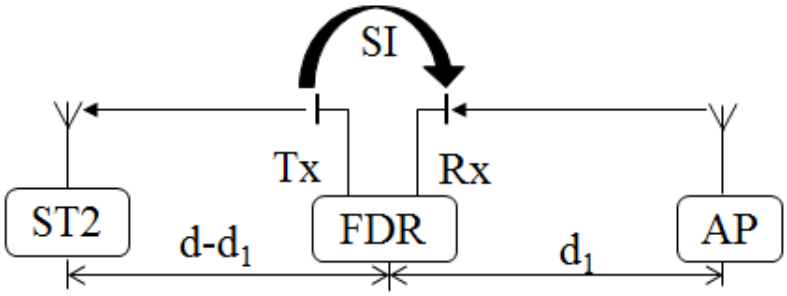

Figure 6.9: Diagram of FDR equipped with patch antennas.

The transmitted signal from the source has power P_T, which travels distance d_1, before reaching FDR, as illustrated in figure 6.9. Therefore, the received signal power by FDR can be expressed using the simplified path loss model as [19]

$$P_{RR} = P_T G_A K \left[\frac{d_0}{d_1}\right]^{\gamma}, \tag{6.42}$$

where G_A is combined antenna gain, d_0 is the reference distance, γ is the path loss exponent, and P_{w1} is the AWGN power at FDR. K is the path loss coefficient computed as $K = [\frac{\lambda}{4\pi d_0}]^{\gamma}$, where λ is the waive length. The received signal by FDR is amplified by a gain factor of A, and re-transmitted. Since total power gain of the FDR is $G_R = A^2$, the transmitted signal by FDR will be

$$P_{RT} = G_R(P_{RR} + E[|w^{si}(n)|^2] + E[|w^r(n)|^2]). \tag{6.43}$$

For simplicity, we denote the residual SI power plus AWGN power as

$$P_{w1} = E[|w^{si}(n)|^2] + E[|w^r(n)|^2]. \tag{6.44}$$

Therefore, the expression in (6.43) can be rewritten as

$$P_{RT} = G_R(P_{RR} + P_{w1}). \tag{6.45}$$

6.5.1 FDR with Constant Gain

In this case, the gain factor is kept constant and does not depend on the level of received power at the relay P_{RR}

$$P_{RT} = G_R \left(P_T G_A K \left[\frac{d_0}{d_1} \right]^{\gamma} + P_{w1} \right). \tag{6.46}$$

Since the distance between the source and destination nodes is d, the signal transmitted by FDR travels distance $d - d_1$; thus the received signal power at the destination can be computed as

$$P_R = P_{RT} G_A K \left[\frac{d_0}{d - d_1} \right]^{\gamma} + P_{w2}, \tag{6.47}$$

where $P_{w2} = E[|w^d(n)|^2]$ is the noise power at destination. Substituting (6.46) into (6.47), the received power at the destination can be expressed in terms of the transmitted signal by

source node as

$$P_R = P_T G_R G_A^2 K^2 \left[\frac{d_0^2}{d_1(d-d_1)}\right]^\gamma + P_{w1} G_R G_A K \left[\frac{d_1}{d-d_1}\right]^\gamma + P_{w2}, \tag{6.48}$$

and consequently, the SINR of the received signal by the destination is

$$\text{SINR} = \frac{P_T G_R G_A^2 K^2 \left[\frac{d_0^2}{d_1(d-d_1)}\right]^\gamma}{P_{w1} G_R G_A K \left[\frac{d_0}{d-d_1}\right]^\gamma + P_{w2}}. \tag{6.49}$$

As it is clear from (6.49), there are two noise terms impacting SINR at the destination. Depending on which noise source is dominant we distinguish the following two scenarios.

Case 1.1: P_{w1} is the dominant noise at destination. Since P_{w1} is the noise of FDR that is being amplified and transmitted, it can become dominant at the destination either if FDR has a high noise figure or FDR operates in high gain mode. High FDR gain is available in the case when large suppression of SI is achieved. The high gain can amplify the P_{w1} enough to cause the first noise term in (6.49) to dominate, such that

$$P_{w1} G_R G_A K \left[\frac{d_0}{d-d_1}\right]^\gamma >> P_{w2}. \tag{6.50}$$

Under the condition given in (6.50), the none-dominant noise term can be neglected, and (6.49) can be simplified as

$$\text{SINR} = \frac{P_T G_A K}{P_{w1}} \left[\frac{d_0}{d_1}\right]^\gamma. \tag{6.51}$$

It is evident from (6.51), that as the distance between the source and FDR increases the SINR at destination decreases.

Case 1.2: P_{w2} is the dominant noise at the destination. Since P_{w2} is the receiver noise

of the destination, it can become dominant when FDR has a low noise figure and operates at low gain mode. Low FDR gain is available in the case when high suppression of SI is unavailable due to the presence of large nearby reflections resulting in

$$P_{w1} G_R G_A K \Big[\frac{d_0}{d - d_1}\Big]^{\gamma} << P_{w2}. \tag{6.52}$$

Under the condition given in (6.52), the none-dominant noise term can be neglected, and expression in (6.49) can be simplified as

$$\text{SINR} = \frac{P_T G_R G_A^2 K^2}{P_{w2}} \left[\frac{d_0^2}{d_1(d - d_1)}\right]^{\gamma}. \tag{6.53}$$

From (6.53) it is evident that SINR follows a U-shaped curve as a function of distance d_1.

6.5.2 FDR with Constant Transmit Power

In this case, the transmit power P_{RT} of FDR is kept constant. Since received signal power P_{RR} changes with distance d_1, FDR gain is varied accordingly to keep the P_{RT} constant. For a given transmit power of P_T, the gain can be computed as

$$G_R = \frac{P_T}{P_{RR}}. \tag{6.54}$$

Substituting received power from (6.42) into (6.54), the gain can be expressed in terms of distance d_1 and an arbitrary constant G_C as

$$G_R = \frac{G_C}{G_A K} \left[\frac{d_1}{d_0}\right]^{\gamma}. \tag{6.55}$$

Using (6.45), the signal transmitted by FDR for this case is

$$P_{RT} = G_C P_T + G_R P_{w1}. \tag{6.56}$$

As follows from (6.56), G_C is a constant gain coefficient, which represents the ratio between transmitted and received signal powers by the FDR, in the absence of noise i.e. $G_C = P_{RT}/P_T$ when $P_{w1} = 0$. As a result, the received signal power at the destination can be expressed as

$$P_R = G_C P_T G_A K \left[\frac{d_0}{d - d_1}\right]^{\gamma} + G_C P_{w1} \left[\frac{d_1}{d - d_1}\right]^{\gamma} + P_{w2}\ , \tag{6.57}$$

and consequently, the SINR of the received signal by the destination can be computed as

$$\text{SINR} = \frac{P_T G_C G_A K \left[\frac{d_0}{d-d_1}\right]^{\gamma}}{G_C P_{w1} \left[\frac{d_1}{d-d_1}\right]^{\gamma} + P_{w2}}\ . \tag{6.58}$$

Case 2.1: P_{w1} is the dominant noise at the destination, such that the following inequality takes place

$$G_C P_{w1} \left[\frac{d_1}{d - d_1}\right]^{\gamma} >> P_{w2}. \tag{6.59}$$

Under the condition given in (6.59), the none-dominant noise term can be neglected and (6.58) can be simplified as

$$\text{SINR} = \frac{P_T G_A K}{P_{w1}} \left[\frac{d_0}{d_1}\right]^{\gamma}. \tag{6.60}$$

The SINR expression, in this case, is identical to the expression derived in (6.51), resulting in the same conclusion.

Case 2.2: P_{w2} is the dominant noise at the destination, resulting in the following inequality

$$G_C P_{w1} \left[\frac{d_1}{d - d_1}\right]^{\gamma} << P_{w2}. \tag{6.61}$$

Under the condition given in (6.61), the none-dominant noise term can be neglected and (6.58) can be simplified as

$$\text{SINR} = \frac{P_T G_C G_A K}{P_{w2}} \left[\frac{d_0}{d - d_1}\right]^{\gamma}. \tag{6.62}$$

It follows from (6.62), that for the case, when Tx power is constant at FDR, as the distance between the source and FDR increases, the SINR at destination also increases.

6.6 Simulation And Experimental Results

In this section, an AF full-duplex relaying system is investigated both experimentally and by simulation, according to the parameters listed in Table 6.2. The aim is to relay data packets without amplifying the self-interference and evaluate the signal quality at the destination node. We first simulate the full-duplex relayed network, evaluating the system performance for constant gain and constant power modes. We then construct a real-time full-duplex network and compare the experimentally measured network performance with simulations for constant gain and constant power modes.

OFDM Parameters	**Value**	**Signal Parameters**	**Value**
Number of OFDM Subcarriers	64	Channel Type	D
Number of Data Subcarriers	48	Doppler Frequency	10 Hz
Number of Pilots	4	AWGN Power	-100dBm
Cyclic Prefix (CP)	$3.2\mu s$	Rx SOI Power	-70 dBm
Symbol Duration (CP+FFT)	$16\mu s$	Rx SI Power	-65 dBm
Long Training Duration	$32\mu s$	Passive Cancellation	-60 dBm
Short Training Duration	$16\mu s$	Carrier Frequency	2.5 GHz
Subcarrier Frequency Spacing	78125 Hz	Signal Bandwidth	5 MHz
Data Packet Duration	1.6ms	Tx Power	-35 dBm

Table 6.2: Simulation parameters

6.6.1 Simulation

To evaluate the system performance depending on the relay location, an extended network using a single FDR is simulated. The relay gain, the noise power at relay P_{w1}, the noise power at destination P_{w2} are selected to highlight the cases presented in Section 6.5, meanwhile keeping them within the realistic range acquired from our experimental system.

Figure 6.10 shows the SINR of the received signal at the destination node for different noise power levels, while the gain of FDR is constant. For low noise level at the destination, when $P_{w2} < P_{w1}$, the SINR drops as FDR is moved away from the source node corresponding to Case 1.1 in Section 6.5. As the noise level at destination becomes larger, the SINR drops as FDR gets close to the midpoint between the two nodes, then increases as FDR gets close to the destination node, creating a U-shaped curve corresponding to Case 1.2 in Section 6.5.

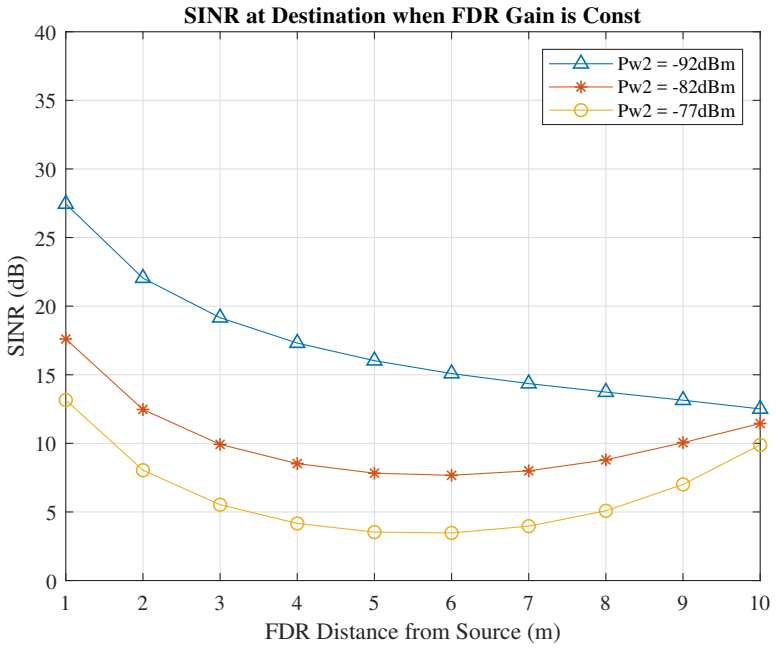

Figure 6.10: Simulated SINR at Destination for different noise levels.

Figure 6.11 illustrates the SINR of the received signal at the destination node for different noise power levels, while the Tx power of FDR is constant. The figure shows that for low

noise level at destination when $P_{w2} < P_{w1}$, the highest SINR at the destination is achieved, when the relay is placed closer to the source, and it drops as FDR is moved away from the source. Since noise level is dominated by P_{w1}, the high SINR at FDR results in high SINR at the destination, which corresponds to Case 2.1 in Section 6.5. However, when the noise level at destination becomes dominant, the lowest SINR at the destination is achieved when FDR is placed closer to the source, and it increases as it gets closer to the destination node, corresponding to Case 2.2 Section 6.5.

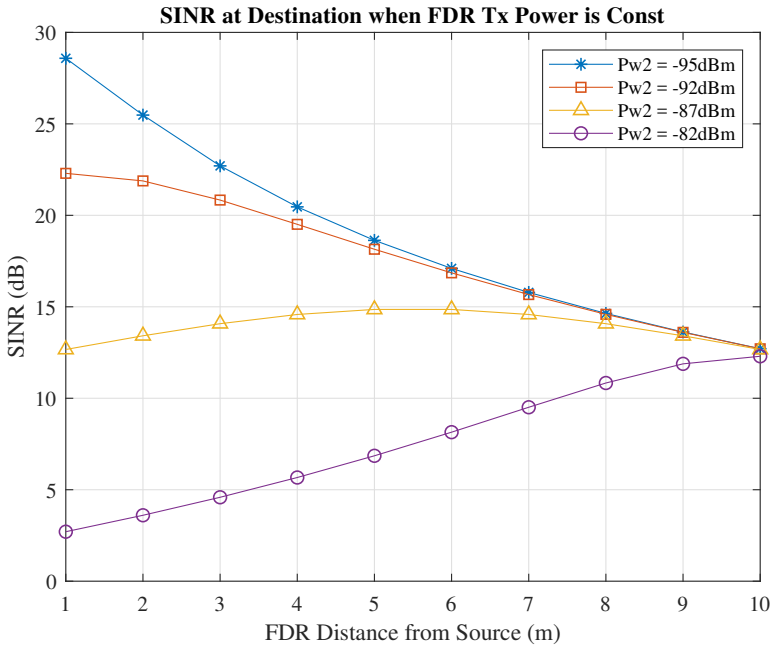

Figure 6.11: Simulated SINR at Destination for different noise levels.

6.6.2 Experiment

FDR Node

A simplified block diagram of the experimental AF-FDR platform is shown in figure 6.12. It is equipped with Rx/Tx patch antennas pointing in opposite directions, that provide 110° coverage (shown in figure 6.8), amplifying the signal of interest towards the destination.

The received signal is amplified and filtered using multistage low-noise amplifiers (LNA) and band-passed filters (BPF). After setting the gain of the FDR using attenuator (ATTN), the signal is amplified by a power amplification stage (PA) and transmitted. To be able to

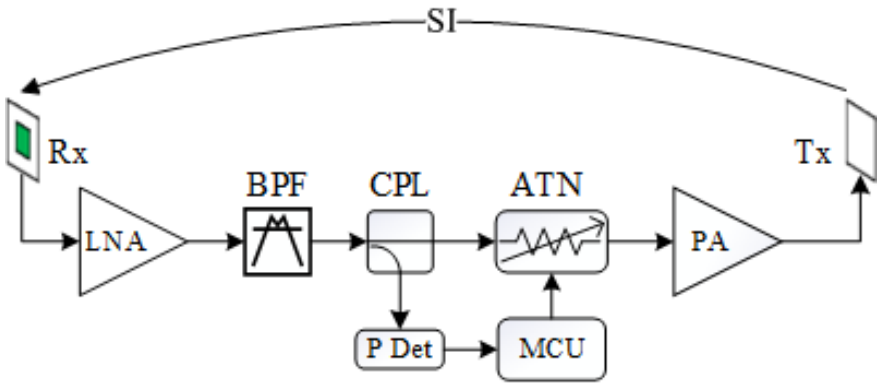

Figure 6.12: FDR architecture block diagram.

estimate the power level of the received signal, a power detector (PDet) is connected to the main RF path through a coupler (CPL). The output of the power detector is sampled by a micro-controller unit (MCU) for FDR gain control. This feature becomes particularly useful for constant Tx power experiments, where the gain of FDR is a function of the received signal power. Setting receiver front end gain of destination node high/low, increases or decreases the noise figure of the receiver [16], which allows experiments with high/low P_{w2}. Figure 6.13 shows the actual implemented system.

Relay Network

An experimental wireless network, consisting of a half-duplex source and a half-duplex destination nodes is constructed, using Universal Software Radio Peripheral (USRP) platforms. The two end nodes are situated 11m apart. Transmit power is reduced to a minimum, which leaves the receiving node outside of the radio coverage area. A full-duplex relay is placed in between the two end nodes to extend the existing network coverage, as shown in figure 6.14.

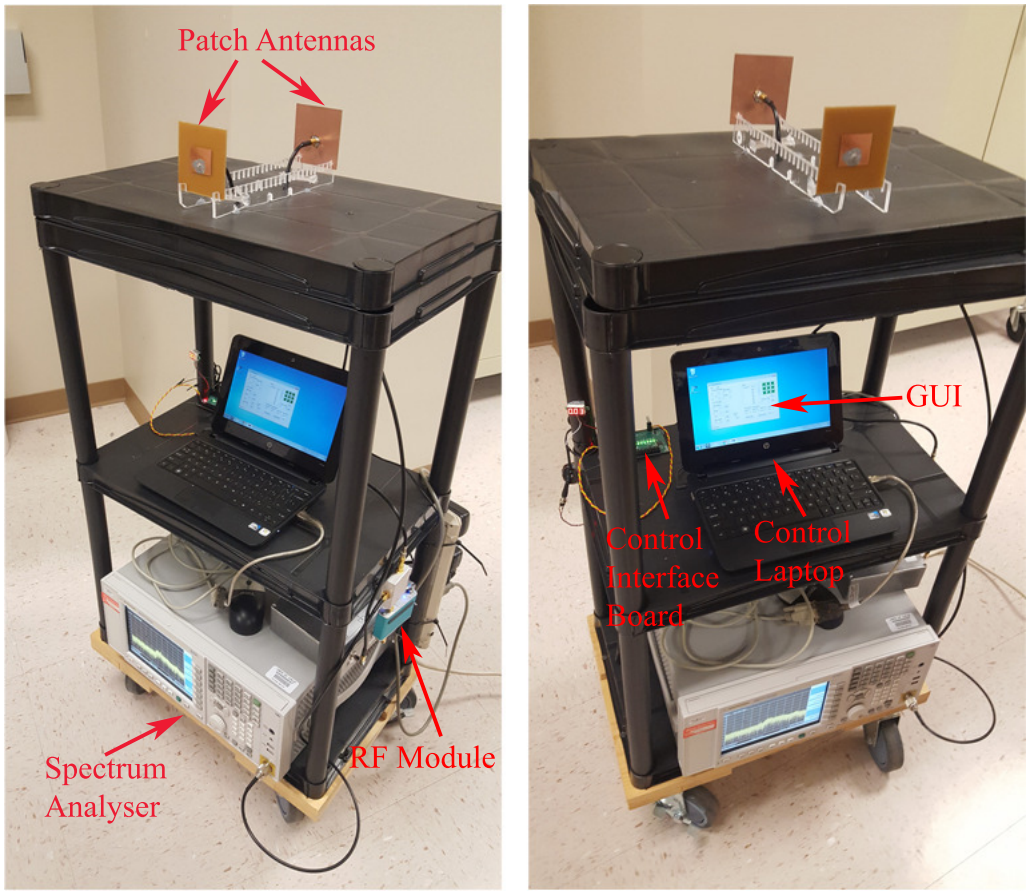

Figure 6.13: Full-Duplex Relay Tower.

The distance between FDR and source is increased by moving the relay closer to destination in 1m increments. As a performance metric, the SINR at the destination node is recorded for high and low destination receiver noise levels, denoted as P_{wrx}.

Displacement of the FDR in a lab environment causes reflected SI variations, due to the presence of multiple nearby objects, which introduce variations in measured performance. In addition, the performance is influenced by nearby wireless devices, transmitting on the same frequency, and causing an increased level of total noise at the destination, such as $P_{w2} = P_{wrx} + P_{wi}$, where P_{wi} is the external interference. To keep the influence of surrounding reflectors negligible, we first conducted experimental measurements outdoor (figure 6.15), followed by indoor measurements (figure 6.16), that show the feasibility of FDR in the crowded lab environment.

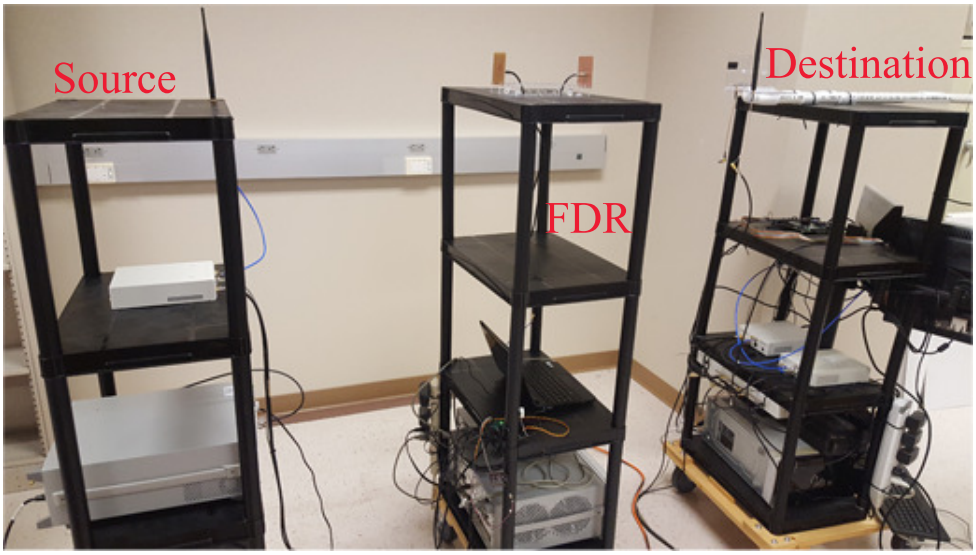

Figure 6.14: Network Nodes with Full-Duplex Relay.

Figure 6.17 illustrates system performance outdoor when the gain of the FDR is kept constant. As it is clear from the figure, the FDR improves the signal reception at the destination. The large SINR improvement (up to 23dB) is achieved when FDR is located closer to the source since it allows the relay to amplify the signal with high SINR. As the FDR is moved away from the source, the SINR of the received signal at the relay reduces, resulting in SINR reduction of the received signal at the destination node. By comparing figure 6.17 and figure 6.10, it becomes clear that the experimental SINR measurements agree with the performance of the simulated system.

Figure 6.18 shows system performance indoor when the gain of FDR is constant. From the figure, it is clear that FDR improves the signal SINR at destination (up to 14dB), despite increased SI level due to the harsh lab environment with many reflectors. When comparing system performance indoor with outdoor (figures 6.18 and 6.17), one can infer that the SINR measurements follow similar trends as outdoor, albeit with variations due to reflections as discussed earlier.

To proceed with system performance evaluation for constant Tx power by relay, a test tone is transmitted by the source node, and the gain of FDR is tuned to meet constant Tx

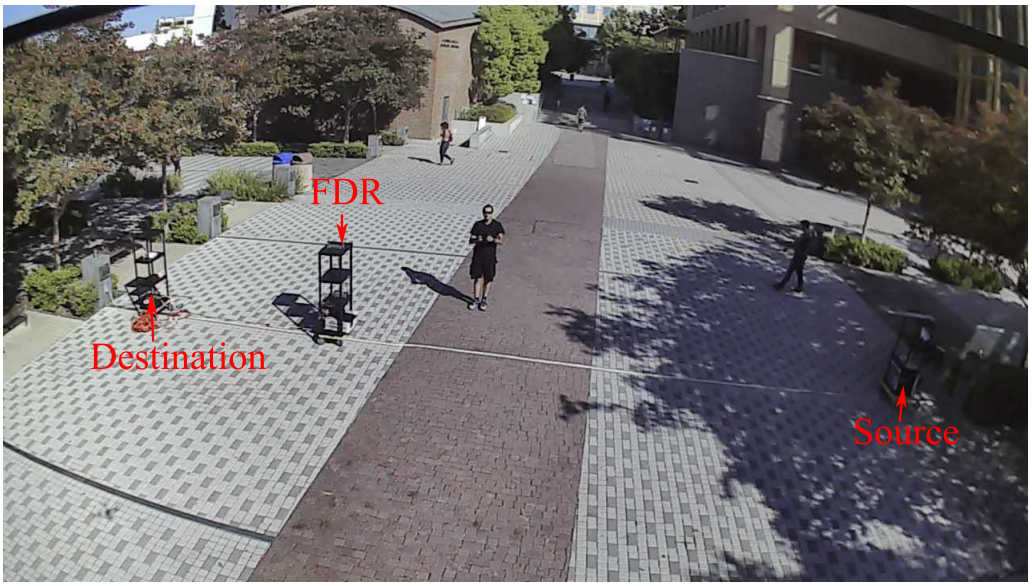

Figure 6.15: Experimental setup in outdoor environment.

power constraint across all the measurements. Figure 6.19 illustrates the system performance outdoor/indoor when the transmit power of the FDR is kept constant. The figure shows that the SINR at the destination node is highest when the relay is placed closer to the destination node, and it drops as the FDR is moved closer to the source. This corresponds to case 2.2 when P_{w2} is dominant. Recall, that P_{w2} can become dominant, either due to the noise contribution P_{w1} by FDR is low, or FDR gain factor is low. Since FDR gain is limited by the amount of SI cancellation, our current setup does not allow us to increase the gain high enough to create the dominant P_{w1} scenario (Case 2.1) experimentally.

6.7 Impact of Relay Location on Network Performance

In this section, optimum relay selection is studied based on the received signal quality at the destination. As it was shown in Section 6.5, the SINR of the relayed signal at the destination can vary significantly depending on noise levels, FDR operating mode, as well as the relative location of AF-FDR with respect to the source and destination nodes. This implies that

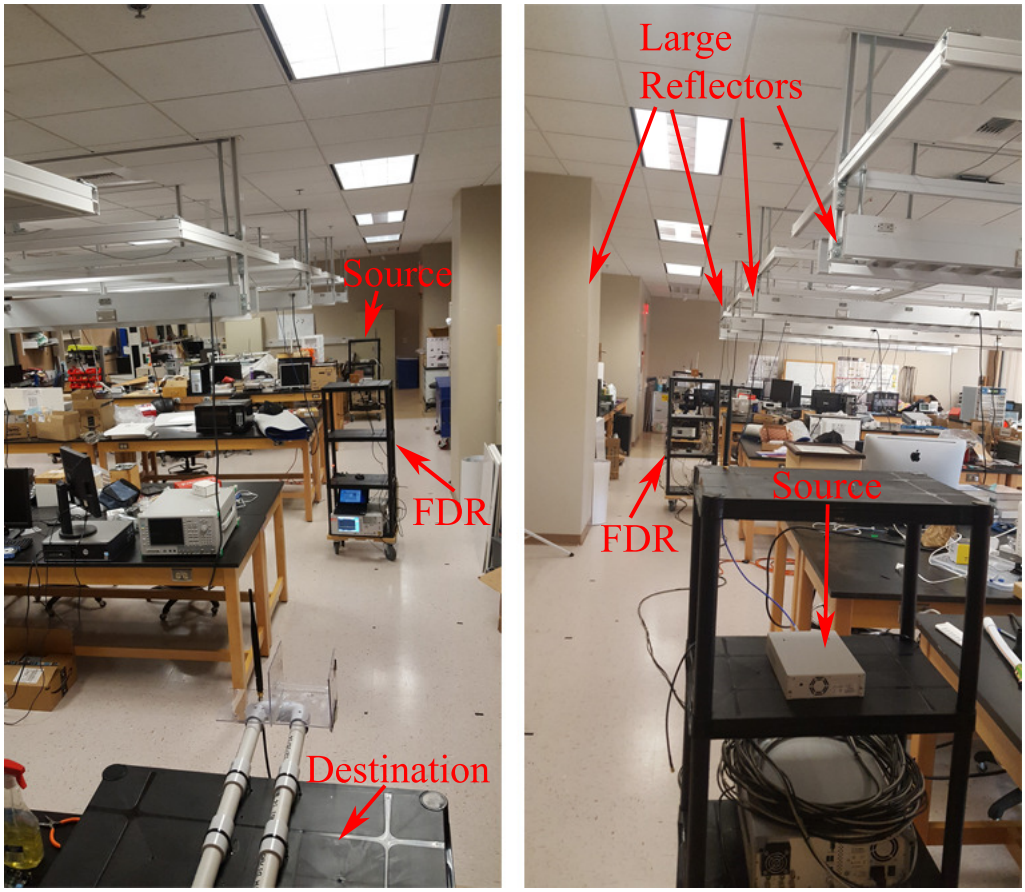

Figure 6.16: Experimental setup in indoor environment.

the highest possible SINR can be achieved by using a smart relay selection mechanism that routes SOI through the available FDRs with relatively high SINR towards the destination. Since the operating mode of the FDR can totally change the dependency of destination SINR on relay location, we distinguish the relay selection under constant gain and constant transmit power modes separately.

6.7.1 Constant Gain FDR Selection

In this case, the gain of the AF-FDR is assumed to be fixed, regardless of the strength of the received signal. In the scenario, when the high gain relay is available in the network, satisfying inequality (6.50) in Section 6.5 Case 1.1, the SINR of the relayed signal at the

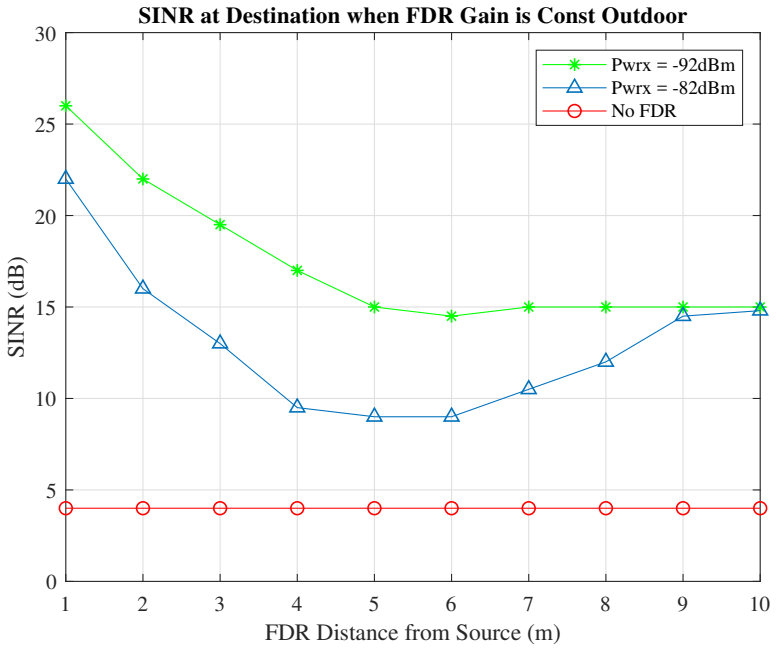

Figure 6.17: Outdoor Experimental system performance when FDR gain is constant.

destination is decreasing function of source relay distance. Therefore, unlike DF-FDR in [21], selecting high gain AF-FDR closer to the source will result in better signal quality at the destination. Due to the gain limitation explained in Section 6.3, a high gain FDR may not be available, creating the Case 1.2 scenario described in Section 6.5. In this case, the SINR of the relayed signal at the destination is a U-shaped curve, suggesting that the selection of relays located the midway source and destination path will result in the worst signal quality at the destination. Therefore, in this case, the FDR near the source node is the best choice, and if it is nonavailable, a relay near the destination node is preferred.

6.7.2 Constant Transmit Power FDR Selection

In this case, the gain of the FDR is a function of the received signal, such that the transmit power is constant. In the case, when the high gain relay is available in the network, satisfying the inequality (6.59) in Section 6.5 Case 2.1, the SINR at the destination is decreasing

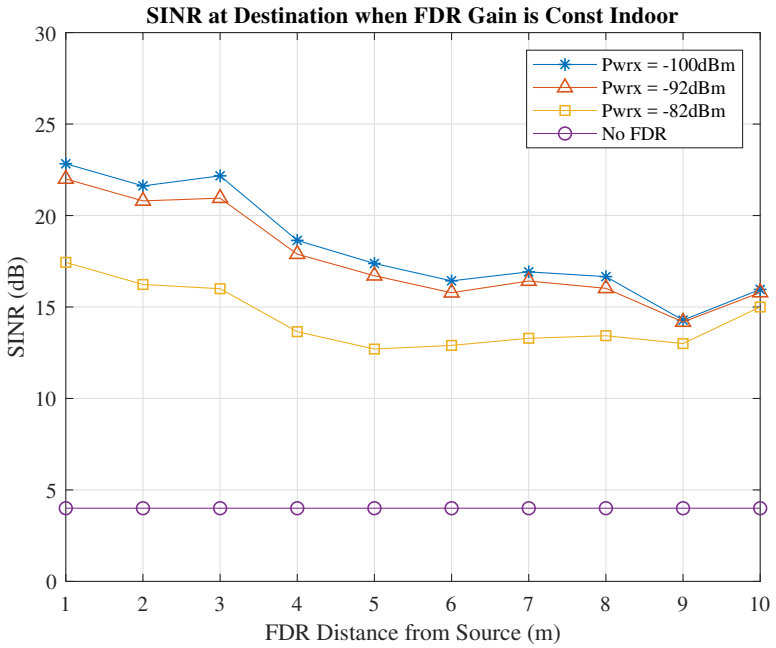

Figure 6.18: Indoor Experimental system performance when FDR gain is constant.

function of source relay distance. Therefore, selecting FDR with high gain closer to the source is preferred, which will result in the best signal quality at the destination. However, due to the gain limitations described in Section 6.3, high gain FDR may not always be available in the network, creating the scenario described in Section 6.5 Case 2.2. In that case, the SINR of the relayed signal at the destination is an increasing function of the source to relay distance, suggesting that a relay closer to the destination should be preferred.

6.8 Conclusion

This chapter presented the design and implementation aspects of the full-duplex amplify and forward relay network. The major challenge is the self-interference suppression in order to provide satisfactory signal quality in the desired area of service. First, the FDR gain is analyzed under the stability, and available transmit power constraints. The stability bounds are derived analytically and are confirmed experimentally. The performance of a tandem

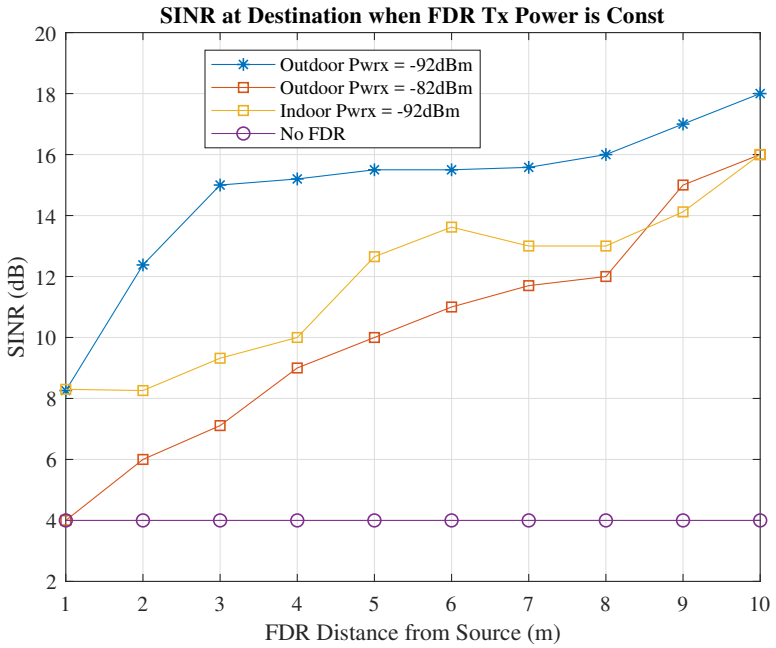

Figure 6.19: Experimental system performance when FDR transmit power is constant.

connected network of FDRs is analyzed, and patch antennas are designed to eliminate inter relay interference. The network performance is analyzed as a function of FDR location for constant gain and constant transmit power modes. In addition, the network performance as a function of FDR location is evaluated by simulation and experimentally, outdoor as well as indoor. Finally, the optimal relay location strategy is proposed maximizing the destination SINR, based on the simulated and experimental results.

6.9 Bidirectional Relaying

As discussed earlier, to gain more SI suppression for FDR systems, omnidirectional antennas, could be replaced by back to back patch antennas as illustrated in figure 6.9. This modification has a number of advantages as follows:

- Due to the directivity of the patch antenna, SI isolation is increased, consequently

improving the coverage of FDR by allowing higher gain, when necessary power is available. Recall that FDR gain is limited by SI suppression and available transmit power, as shown in the Section 6.3.

- Increasing SI suppression in propagation domain is preferred because it avoids saturation of Rx front-end.
- This type of arrangement of patch antennas uses transmit power efficiently by directing energy towards extended area.

In order to support bi-directional (both upstream and downstream) traffic with directional patch antennas, an additional signal path is required as shown in figure 6.20.

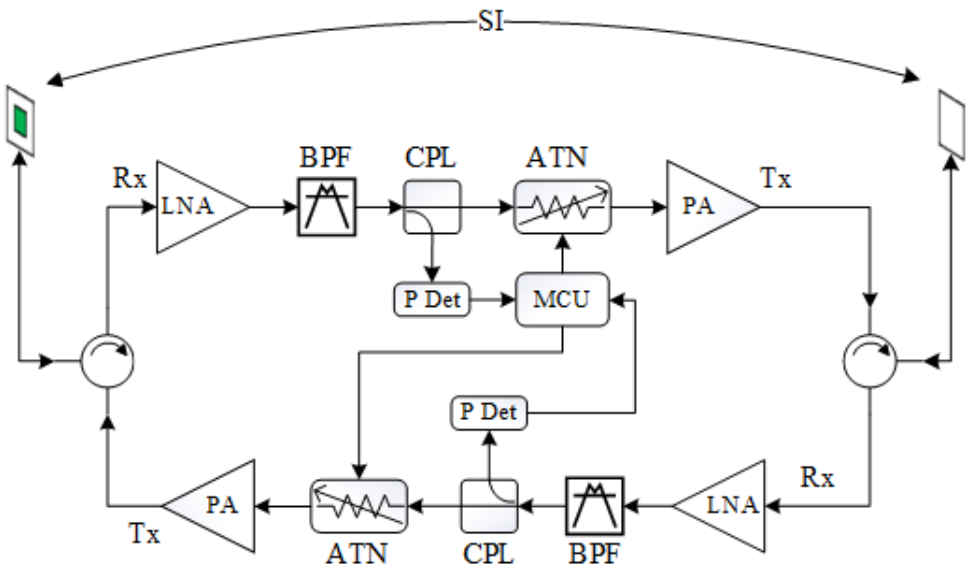

Figure 6.20: System Diagram of Bi-Directional FDR

The two signal paths are coupled to patch antennas with a circulator, which separates the incoming and outgoing signal streams to the corresponding Rx and Tx chains respectively. In general circulators provide finite amount of isolation between incoming and outgoing signal paths in the range of 20dB - 60dB, which means a small part of the Tx signal will leak back, creating additional feedback loop. To increase isolation between the two branches and break

the loop, only one of the branches can be activated based on signal propagation direction. Since the end-nodes are operating in half-duplex mode, there will be one signal per time slot traveling in either direction. When the channel is idle the micro-controller unit (MCU) disables power amplifiers (PA) of both branches. As soon as there is an incoming packet, the MCU can sense its preamble and enable the corresponding PA to allow transmission. This way only one PA is active at a time and loop is broken preventing feedback due to RF leakage. Performance details will be given in section 6.6.

Chapter 7

Conclusions and Future Work

In this thesis, we consider the practical issues of a wireless network with full-duplex enabled nodes.

First, a network consisting of a full-duplex base station that wirelessly communicates with half-duplex nodes is constructed. The synchronization errors were analytically modeled and their impact on the system performance was investigated. Novel techniques were proposed that allow synchronization error compensation in time and frequency for full-duplex OFDM systems. The effectiveness and robustness of those techniques are tested on the real-time full-duplex network.

Second, the impact of environmental dynamics on the received SI for the full-duplex system was investigated, which is equipped with a reconfigurable antenna as a passive SI cancellation stage. The power delay profile of the SI channel, which is acquired by the narrow band as well as wide-band systems are compared for the cases when suppressing, and non-suppressing antenna patterns are selected. In addition, the SI channel is modeled using statistical probability distribution fitting, and candidate models are compared using the goodness of fit test.

Third, a full-duplex relay is considered, and its compatibility to extend an existing WiFi network is investigated. Novel techniques were proposed, enabling active SI cancellation for amplify and forward as well as decode and forward full-duplex relays while using a standardized WiFi frame structure.

Finally, a complete full-duplex relayed network was implemented using a custom-designed amplify and forward hardware platform. As a first step, the relay gain limitations under stability, and available transmit power constraints was investigated. Second,the overall system performance depending on the relay location in the cases when the relay operates in constant gain as well as constant transmit power modes was studied. The performance of the end-to-end network was tested by simulation and experimentally in outdoor/indoor environments, demonstrating up to 23dB SINR improvement at the destination node.

As future work, one can extend the single FDR network, creating a tandem connected FDR network, and investigate the inter relay interference cancellation in the physical domain. The FDR antennas can be replaced with configurable beam steering or multiple-input multiple-output (MIMO) setup. This type of modification has the potential of increasing SI suppression, resulting in greater radio coverage; however, it requires training algorithms to achieve maximum SI suppression, while maintaining strong SOI link.

Bibliography

[1] E. Ahmed, A. M. Eltawil, Z. Li, and B. A. Cetiner. Full-Duplex Systems Using Multireconfigurable Antennas. *IEEE Transactions on Wireless Communications*, 14(11):5971–5983, 2015.

[2] E. Ahmed, A. M. Eltawil, and A. Sabharwal. Self-interference cancellation with nonlinear distortion suppression for full-duplex systems. *Conference Record - Asilomar Conference on Signals, Systems and Computers*, pages 1199–1203, 2013.

[3] M. S. Amjad, H. Nawaz, K. Ozsoy, O. Gurbuz, and I. Tekin. A Low-Complexity Full-Duplex Radio Implementation with a Single Antenna. *IEEE Transactions on Vehicular Technology*, 67(3):2206–2218, 2018.

[4] S. Atapattu, P. Dharmawansa, M. Di Renzo, C. Tellambura, and J. S. Evans. Multi-User Relay Selection for Full-Duplex Radio. *IEEE Transactions on Communications*, 67(2):955–972, 2019.

[5] A. S. Behbahani, A. M. Eltawil, and H. Jafarkhani. Linear decentralized estimation of correlated data for power-constrained wireless sensor networks. *IEEE Transactions on Signal Processing*, 60(11):6003–6016, 2012.

[6] A. S. Behbahani, R. Merched, and A. M. Eltawil. Optimizations of a MIMO relay network. *IEEE Transactions on Signal Processing*, 56(10 II):5062–5073, oct 2008.

[7] S. Bojja-Venkatakrishnan, E. A. Alwan, and J. L. Volakis. Wideband RF and analog self-interference cancellation filter for simultaneous transmit and receive system. *2017 IEEE Antennas and Propagation Society International Symposium, Proceedings*, 2017-Janua:933–934, 2017.

[8] S. Bojja Venkatakrishnan, E. A. Alwan, and J. L. Volakis. Wideband RF self-interference cancellation circuit for phased array simultaneous transmit and receive systems. *IEEE Access*, 6:3425–3432, 2018.

[9] L. Chen, F. Wu, J. Xu, K. Srinivasan, and N. Shroff. BiPass: Enabling end-to-end full duplex. *Proceedings of the Annual International Conference on Mobile Computing and Networking, MOBICOM*, Part F1312:114–126, 2017.

[10] X. Chen, G. Liu, Z. Ma, X. Zhang, W. Xu, and P. Fan. Optimal Power Allocations for Non-Orthogonal Multiple Access over 5G Full/Half-Duplex Relaying Mobile Wireless Networks. *IEEE Transactions on Wireless Communications*, 18(1):77–92, 2019.

[11] J. Choi, D. Kim, S. Lee, H. Lee, J. Bang, and D. Hong. A new frame structure for asynchronous in-band full-duplex systems. In *IEEE International Symposium on Personal, Indoor and Mobile Radio Communications, PIMRC*, volume 2015-Decem, pages 487–491, 2015.

[12] W. Choi, J. Park, Y. Kim, A. Sabharwal, and H. Lim. Design and Implementation of a Full-Duplex Pipelined MAC Protocol for Multihop Wireless Networks. *IEEE Access*, 5(D):14930–14942, 2017.

[13] T. M. C. Chu and H. J. Zepernick. Performance of a Non-Orthogonal Multiple Access System with Full-Duplex Relaying. *IEEE Communications Letters*, 22(10):2084–2087, 2018.

[14] S. Dey, T. Dey, and D. Kundu. Two-parameter Rayleigh distribution: Different methods of estimation. *American Journal of Mathematical and Management Sciences*, 33(1):55–74, 2014.

[15] Q. Ding, M. Liu, and Y. Deng. Secrecy Outage Probability Analysis for Full-Duplex Relaying Networks Based on Relay Selection Schemes. *IEEE Access*, 7:105987–105995, 2019.

[16] R. Ettus. USRP Daughterboard SBX 400-4400 MHz Rx/Tx (40 MHz).

[17] E. Everett, A. Sahai, and A. Sabharwal. Passive self-interference suppression for full-duplex infrastructure nodes. *IEEE Transactions on Wireless Communications*, 13(2):680–694, 2014.

[18] M. E. Fouda, S. Shaboyan, A. Elezabi, and A. Eltawil. Application of ICA on Self-Interference Cancellation of In-band Full Duplex Systems. *IEEE Wireless Communications Letters*, 2337(c):1–1, 2020.

[19] A. Goldsmith. *Wireless Connunications*. Cambridge University Press, 2005.

[20] K. Haneda, E. Kahra, S. Wyne, C. Icheln, and P. Vainikainen. Measurement of loop-back interference channels for outdoor-to-indoor full-duplex radio relays. *EuCAP 2010 - The 4th European Conference on Antennas and Propagation*, pages 1–5, 2010.

[21] J. Hou, S. Narayanan, N. Yi, Y. Ma, and M. Shikh-Bahaei. Symbol-level selective full-duplex relaying with power and location optimization. *IEEE Transactions on Communications*, 66(11):5097–5111, 2018.

[22] T. Huusari, Y. S. Choi, P. Liikkanen, D. Korpi, S. Talwar, and M. Valkama. Wideband self-adaptive RF cancellation circuit for full-duplex radio: Operating principle and measurements. *IEEE Vehicular Technology Conference*, 2015(Lcm):1–7, 2015.

[23] IEEE Computer Society. IEEE Standard for Information technology–Telecommunications and information exchange between systems Local and metropolitan area networks–Specific requirements - Part 11: Wireless LAN Medium Access Control (MAC) and Physical Layer (PHY) Specifications. *IEEE Std 802.11-2016 (Revision of IEEE Std 802.11-2012)*, 2016(June):1–3534, 2016.

[24] H. Ju, S. Lee, K. Kwak, E. Oh, and D. Hong. A new duplex without loss of data rate and utilizing selection diversity. In *IEEE Vehicular Technology Conference*, number 1, pages 1519–1523, 2008.

[25] M. G. Khafagy, M. S. Alouini, and S. Aissa. Full-duplex relay selection in cognitive underlay networks. *IEEE Transactions on Communications*, 66(10):4431–4443, 2018.

[26] P. Kohnke. ANSYS Theory Reference - Release 5.6, 1999.

[27] D. Korpi, M. Heino, C. Icheln, K. Haneda, and M. Valkama. Compact Inband Full-Duplex Relays with beyond 100 dB Self-Interference Suppression: Enabling Techniques and Field Measurements. *IEEE Transactions on Antennas and Propagation*, 65(2):960–965, 2017.

[28] Y. Kurzo, A. Burg, and A. Balatsoukas-Stimming. Design and Implementation of a Neural Network Aided Self-Interference Cancellation Scheme for Full-Duplex Radios. *Conference Record - Asilomar Conference on Signals, Systems and Computers*, 2018-Octob:589–593, 2019.

[29] Q. N. Le, V. N. Q. Bao, and B. An. Full-duplex distributed switch-and-stay energy harvesting selection relaying networks with imperfect CSI: Design and outage analysis. *Journal of Communications and Networks*, 20(1):29–46, 2018.

[30] H. Lee, J. Choi, D. Kim, and D. Hong. Impact of time and frequency misalignments in OFDM based in-band full-duplex systems. *IEEE Wireless Communications and Networking Conference, WCNC*, pages 1–6, 2017.

[31] S. Li, K. Yang, M. Zhou, J. Wu, L. Song, Y. Li, and H. Li. Full-Duplex Amplify-and-Forward Relaying: Power and Location Optimization. *IEEE Transactions on Vehicular Technology*, 66(9):8458–8468, 2017.

[32] G. Liu, F. R. Yu, H. Ji, V. C. M. Leung, and X. Li. In-Band Full-Duplex Relaying: A Survey, Research Issues and Challenges. *IEEE Communications Surveys Tutorials*, 17(2):500–524, 2015.

[33] B. McNair and B. Daneshrad. An integrated OFDM receiver for high-speed mobile data communications. *GLOBECOM'01. IEEE Global Telecommunications Conference (Cat. No.01CH37270)*, 5:3090–3094, 2001.

[34] V. Midasala, P. Siddaiah, and S. N. Bhavanam. Rectangular patch antenna array design at 13GHz frequency using HFSS. *2014 IEEE International Conference on Computational Intelligence and Computing Research, IEEE ICCIC 2014*, 8:6–9, 2015.

[35] Morelli, Michele, C-C. Jay Kuo and M.-O. Pun. Synchronization Techniques for Orthogonal Frequency Division Multiple Access (OFDMA): A Tutorial Review. *Proceedings of the IEEE*, 95(7):1394 – 1427, 2007.

[36] N. Nomikos, T. Charalambous, D. Vouyioukas, R. Wichman, and G. K. Karagiannidis. Power Adaptation in Buffer-Aided Full-Duplex Relay Networks with Statistical CSI. *IEEE Transactions on Vehicular Technology*, 67(8):7846–7850, 2018.

[37] C. D. Nwankwo, L. Zhang, A. Quddus, M. A. Imran, and R. Tafazolli. A Survey of Self-Interference Management Techniques for Single Frequency Full Duplex Systems. *IEEE Access*, 6:30242–30268, 2018.

[38] J. Park, Y. Kim, G. Kim, and H. Lim. Power allocation for multi-hop transmission using unsaturated full-duplex relay network model. *IEEE Wireless Communications Letters*, 7(6):906–909, 2018.

[39] F. Passerini and A. M. Tonello. Analog Full-Duplex Amplify-and-Forward Relay for Power Line Communication Networks. *IEEE Communications Letters*, 23(4):676–679, 2019.

[40] I. Progri, W. Michalson, and M. Bromberg. Accurate synchronization using a full duplex DSSS channel. *PLANS 2004. Position Location and Navigation Symposium (IEEE Cat. No.04CH37556)*, pages 220–226, 2004.

[41] A. Sabharwal, P. Schniter, D. Guo, D. W. Bliss, S. Rangarajan, and R. Wichman. In-band full-duplex wireless: Challenges and opportunities. *IEEE Journal on Selected Areas in Communications*, 32(9):1637–1652, 2014.

[42] A. Sethi, V. Tapio, and M. Juntti. Self-interference channel for full duplex transceivers. *IEEE Wireless Communications and Networking Conference, WCNC*, 1:781–785, 2014.

[43] S. Shaboyan, E. Ahmed, A. S. Behbahani, W. Younis, and A. M. Eltawil. Frequency and Timing Synchronization for In-Band Full-Duplex OFDM System. In *GLOBECOM*, 2017.

[44] S. Shaboyan, A. S. Behbahani, and A. M. Eltawil. Active Cancellation of Self-Interference for Full-Duplex Amplify and Forward Wi-Fi Relay, 2018.

[45] S. Shaboyan, A. S. Behbahani, and A. M. Eltawil. Robust Frame Boundary Synchronization for In-Band Full-Duplex OFDM System. *Conference Record - Asilomar Conference on Signals, Systems and Computers*, 2018-Octob:1395–1399, 2019.

[46] H. Shen, Z. He, W. Xu, S. Gong, and C. Zhao. Is Full-Duplex Relaying More Energy Efficient Than Half-Duplex Relaying? *IEEE Wireless Communications Letters*, 8(3):841–844, 2019.

[47] N. V. Shende, Ö. Gürbüz, and E. Erkip. Half-Duplex or Full-Duplex Communications: Degrees of Freedom Analysis under Self-Interference. *IEEE Transactions on Wireless Communications*, 17(2):1081–1093, 2018.

[48] M. Sliskovic. Carrier and sampling frequency offset estimation and correction in\nmulticarrier systems. *GLOBECOM'01. IEEE Global Telecommunications Conference (Cat. No.01CH37270)*, 1:285–289, 2001.

[49] X. Song and S. Xu. Joint Optimal Power Allocation and Relay Selection in Full-Duplex Energy Harvesting Relay Networks. *2018 10th International Conference on Communication Software and Networks, ICCSN 2018*, pages 80–84, 2018.

[50] S. N. Venkatasubramanian, L. Laughlin, K. Haneda, and M. A. Beach. Wideband self-interference channel modelling for an on-frequency repeater. *2016 10th European Conference on Antennas and Propagation, EuCAP 2016*, pages 1–5, 2016.

[51] Z. Wei, X. Zhu, S. Sun, Y. Jiang, A. Al-Tahmeesschi, and M. Yue. Research Issues, Challenges, and Opportunities of Wireless Power Transfer-Aided Full-Duplex Relay Systems". *IEEE Access*, page 1, 2017.

[52] X. Wu, Y. Shen, and Y. Tang. Propagation characteristics of the full-duplex self-interference channel for the indoor environment at 2.6 GHz. *IEEE Antennas and Propagation Society, AP-S International Symposium (Digest)*, 0(1):1183–1184, 2014.

[53] X. Wu, Y. Shen, and Y. Tang. The power delay profile of the single-antenna full-duplex self-interference channel in indoor environments at 2.6 GHz. *IEEE Antennas and Wireless Propagation Letters*, 13:1561–1564, 2014.

[54] H. I. Yoo, K. S. Woo, C. H. Park, J. Kim, S. Jung, and Y. S. Cho. A synchronization technique for OFDM-based Full Duplex Relays with frequency-domain feedback interference canceller. *IEICE Transactions on Communications*, E92-B(11):3487–3490, 2009.

[55] F. Zabini, G. Pasolini, and O. Andrisano. Design Criteria for FIR-Based Echo Cancellers. *IEEE Transactions on Broadcasting*, 62(3):562–578, 2016.